Optical Trapping of Ytterbium Atoms

Reina Maruyama

A dissertation submitted in partial fulfillment of
the requirements for the degree of

Doctor of Philosophy

University of Washington

2003

Program Authorized to Offer Degree: Department of Physics

UMI Number: 3091035

UMI Microform 3091035

ProQuest Information and Learning Company
300 North Zeeb Road
P.O. Box 1346
Ann Arbor, MI 48106-1346

In presenting this dissertation in partial fulfillment of the requirements for the Doctoral degree at the University of Washington, I agree that the Library shall make its copies freely available for inspection. I further agree that extensive copying of this dissertation is allowable only for scholarly purposes, consistent with "fair use" as prescribed in the U.S. Copyright Law. Requests for copying or reproduction of this dissertation may be referred to Proquest Information and Learning, 300 North Zeeb Road, Ann Arbor, MI 48106-1346, to whom the author has granted "the right to reproduce and sell (a) copies of the manuscript in microform and/or (b) printed copies of the manuscript made from microform."

Signature 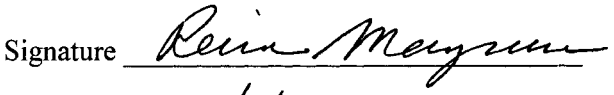

Date 5/6/03

University of Washington

Graduate School

This is to certify that I have examined this copy of a doctoral dissertation by

Reina Maruyama

and have found that it is complete and satisfactory in all respects,
and that any and all revisions required by the final
examining committee have been made.

Chair of Supervisory Committee:

E. Norval Fortson

Reading Committee:

E. Norval Fortson

Blayne R. Heckel

Warren Nagourney

Date: 5/6/03

University of Washington

Abstract

Optical Trapping of Ytterbium Atoms

by Reina Maruyama

Chair of Supervisory Committee:

Professor E. Norval Fortson
Department of Physics

This dissertation describes an experimental study on magneto-optical trapping (MOT) of ytterbium atoms. In particular, Doppler cooling and sub-Doppler cooling have been investigated and compared in the same atom, and sub-Doppler cooling has been studied in two isotopes of ytterbium possessing different nuclear angular momenta. Ytterbium offers a unique combination of having a closed S-shell in the ground state, several isotopes with high abundances, and two transitions that are accessible by lasers that can be used for laser cooling and trapping. Laser cooling with several different ground-state angular momenta can be studied by simply changing isotopes with little changes to the experimental parameters.

All seven stable isotopes of ytterbium have been slowed from an atomic beam, trapped in a MOT using the strong $^1S_0$–$^1P_1$ line and transfered into a second MOT using the $^1S_0$–$^3P_1$ intercombination line. The apparatus developed for this experiment is described in detail, including the lasers used for both transitions at 399 nm and 556 nm. Trap properties such as temperature, spring constant, lifetime of the traps, and isotope dependence of cooling mechanisms in the $^1S_0$–$^3P_1$ trap were investigated. Doppler cooling was studied in even isotopes with no spin in the ground state. Sisyphus cooling in the ground state of odd isotopes of alkaline-earth-like atoms with zero electronic and non-zero nuclear angular momentum was demonstrated for the first time, and compared with numerical simulations. Future directions that exploit the unique features of ytterbium are also discussed.

TABLE OF CONTENTS

LIST OF FIGURES

LIST OF TABLES

GLOSSARY/ACRONYMS

AOM: Acousto optic modulator. It shifts the frequency of the laser by mixing a determined acoustic frequency.

BBO crystal: Beta-Barium Borate non-linear crystal.

Blue laser: Laser at 399 nm, resonant with $^1S_0$–$^1P_1$ line of ytterbium.

Blue MOT: Magneto-optical trap using the $^1S_0$–$^1P_1$ transition.

EDM: Electric dipole moment or a permanent electric dipole moment.

EOM: Electro optic modulator. It shifts the phase of the laser by mixing a determined radio-frequency.

FM: Frequency modulation.

FORT: Far-off resonance trap.

FPI: Fabry-Perot interferometer.

FWHM: Full width at half maximum.

FSR: Free-spectral range.

Green laser: Laser at 556 nm, resonant with $^1S_0$–$^3P_1$ line of ytterbium.

Green MOT: Magneto-optical trap using the $^1S_0$–$^3P_1$ transition.

Group II: Atoms with two electrons closing the valence s-shell. These are second column in the periodic table, including Be, Mg, Ca, Sr, Ba, and Ra.

IC: Input coupler.

LBO crystal: Lithium triborate (LiB_3O5) non-linear crystal.

MLVS: Multi-line visible.

MOT: Magneto-optical trap.

PSD: Phase-sensitive detector.

PMT: Photomultiplier Tube.

RF: Radio-frequency.

SHG: Second harmonic generation.

TOF: Time-of-flight.

ACKNOWLEDGMENTS

I would like to thank my advisor, Prof. Norval Fortson, whose intuition about physics and human beings never cease to amaze me. Without his support and understanding, this project would not have been possible. Prof. Michael Romalis and Amar Andalkar are largely responsible for the early design and setup of the lasers and apparatus. Without their help, this project would have gotten off to a much slower start. Dr. (and now Special Agent) Roahn Wynar came in at the right time to push the experiment forward, and I am indebted to him for the improvements in the data acquisition system that allowed us to make the temperature measurements. I would also like to thank Prof. Warren Nagourney for sharing his expertise in lasers with us, and Alex Cronin for teaching me the way around the lab, and letting me work with him in the very early days of my time in the Fortson Lab. The support from the staff in the physics department at the University of Washington were also invaluable to the experiment: Mike Vinton and others in the machine shop, Bob Morley in the glass shop, and Dr. Bryan Venema in the electronics shop. I would also like to thank those who have worked very hard to improve the lives of graduate students during the time I was here: Profs. David Boulware and Steve Sharpe, and the graduate program coordinators, Kim Hawley and Nichole Fernkes. Thanks to Prof. Steve Lamoreaux for giving me confidence early on, and Claire Cramer for taking over this difficult experiment so that I can leave knowing that the experiment, and the graduate student affairs, are in good hands. Thanks also to all the other characters in the lab past, present, and future, who have helped me along in so many different ways: Dr. Bruce Warrington, Dr. Justin Torgerson, Dr. Kristi Hendrickson, Timo Koerber, Clark Griffith, Matt Swallows, Jeff Sherman, Chris Pearson, and Laura Kogler. This

work would not have been possible without the support of those outside the lab: Pieter, Paul, (no Mary), Arnd, Debbie, and the list goes on. Special thanks to my parents, who opened up so many doors, and let me choose the ones to go through, and to Karsten, for inspiring so many around him to be their best, and for never doubting my abilities.

The work described in this dissertation is supported by the National Science Foundation.

Chapter 1

INTRODUCTION

Optical trapping of neutral atoms has become a powerful and ubiquitous tool to produce and study ultra-cold samples of dilute gases. Much work has been done on alkali-metal traps including their use in the initial but crucial steps to achieve what was one of the main driving motivations of the field of cold atoms: Bose-Einstein condensation (BEC). There are several differences between the well-studied alkali-metals and ytterbium that make it more suitable for a variety of studies. The simple electronic structure of the ground state, $^1S_0$, and the lack of nuclear spin in the even isotopes allow for calculations to be done without hyperfine structure. Most of the studies on cold atoms have been conducted on alkali-metal species, and many properties of cold non-alkali atom traps remain unexplored.

Although Doppler and sub-Doppler cooling are the starting points and building blocks of most cold atom studies, they have not been fully experimentally investigated. This dissertation describes the first observation of sub-Doppler cooling in a zero-electron spin ground state. It is also the first work which makes direct comparison of Doppler and sub-Doppler cooling in the same system. There has been much interest in cold ytterbium and alkaline-earth atoms in the recent years for their simple electronic structure in the ground state and existence of their narrow intercombination line. Having seven isotopes with five bosons and two fermions, trapped ytterbium is a candidate for a variety of studies including those of frequency standards and fundamental symmetries.

1.1 Background

This experiment was motivated by the ongoing search for a permanent electric dipole moment (EDM). The Fortson laboratory at the University of Washington has been a leader in

the search for permanent EDMs in atoms: a signature of time-reversal symmetry violation. The work described in this dissertation began with the goal of finding out whether an EDM search is feasible with clouds of optically trapped atoms. We set out to see whether trapping ytterbium is possible, how many can be trapped, and to find out what is required to achieve the sensitivity that would make it competitive with the current EDM experiments.

In the process, we have acquainted ourselves with the rapidly growing field of cold atoms, and studied interesting atom trap properties which are unique to ytterbium and other closed-shell atoms. We have conducted the first direct comparison of Doppler and sub-Doppler cooling mechanisms by using the even and odd isotopes of Yb. Although EDM experiments in atom traps have not been ruled out, it will take many more years of hard work. In the meantime, there are many other interesting phenomenon to study.

Much has happened since we started the Yb project in 1997. A new version of the mercury (Hg) experiment which was under development for several years has come on line, and new EDM experiments are planned in other laboratories. The much-sought-after Bose-Einstein condensation (BEC), first predicted in 1924, was achieved for the first time in 1995 with cold neutral trapped atoms, and the field has grown into a full bloom. Collision studies of cold atoms have become possible, and have become very important in the context of BECs and as a systematic to precision measurements in cold atoms. With Nobel prizes awarded for atom trapping in 1997 and for BEC in 2001, and the addition of fermions to the study of quantum degeneracy in 1999, the field of atom trapping has been an exciting one. The ytterbium project combines these exciting aspects of atomic physics.

1.2 Overview

This thesis is organized as follows: Chapter 2 discusses the motivation and the historical background behind this experiment. Chapter 3 discusses key aspects about laser cooling and trapping which are important to this experiment. The relevant properties of ytterbium are discussed in Chapter 4. Chapter 5 describes the apparatus used for the measurements described in this thesis, and Chapter 6 describes the key component of this experiment: the lasers. Chapter 7 contains the results from the work done on the magneto-optical trapping

using the $^1S_0$–$^1P_1$ transition, and Chapter 8 has the results on our work on the trap using the $^1S_0$–$^3P_1$ transition. The conclusions of this dissertation are presented in Chapter 9. The appendices include some electronic schematics and possible short-term improvements and additions to the current apparatus. For clarity and consistency, I have used the notation used in the laser cooling and trapping textbook by Metcalf and van der Straten [Met99]. For quick reference, I have listed some parameters that are used often in trapping ytterbium atoms in Table 4.4.

Chapter 2

MOTIVATION AND HISTORICAL PERSPECTIVE

One of the most exciting aspects of atomic physics is its ability to probe physics beyond the Standard Model in the high energy realm at energies above 10^9 eV. This is done using optical transitions of atoms of just a few eV, most of the time in small tabletop experiments run by only a few researchers. The Fortson laboratory has traditionally focused on such experiments that study fundamental symmetries: precision measurements of time-reversal symmetry and parity non-conservation. The idea for the ytterbium trapping experiment came up as part of such an effort, as an exploratory work to see whether an experiment to look for a permanent electric-dipole moment (EDM) is feasible in an atom trap environment. The discovery of a permanent EDM would signify violation of time-reversal symmetry.

As an atom with an electronic spin of zero in the ground state, ytterbium (Yb) has a structure that is very similar to mercury (Hg). In addition, both ^{199}Hg and ^{171}Yb have nuclear spin of $I = 1/2$, a condition essential to minimize systematics for a sensitive measurement of EDM. ^{199}Hg has been studied over the years, and an upper limit of $10^{-28} e\,\mathrm{cm}$ on the size of atomic Hg has been set by our group. We set out to gain competence and expertise in the field of atom trapping and to determine whether an experiment with trapped Yb or Hg would be able to reach competitive levels in sensitivity as the Hg experiment, and lay out what is involved in reaching this goal.

Because of the spin zero electronic ground state in Yb, there are some interesting trapping features which are different from the alkali-metal atoms such as sodium (Na), rubidium (Rb), or cesium (Cs) which have been studied extensively. Ytterbium, with a closed s-shell in the ground state, has an electronic structure which is similar to the alkaline-earth atoms (also called group II atoms) such as magnesium (Mg), calcium (Ca), and strontium (Sr). The lack of spin in the ground state makes theoretical modeling of trapping, cooling, and collision processes much simpler, and quantitative comparisons that are not possible in

alkali-metals are possible in alkaline-earths and Yb. In these atoms, Doppler cooling can be studied independent of the overwhelming effects of sub-Doppler cooling. In alkali-metal species, the existence of hyperfine structure has prevented the development of quantitative theoretical collision models which can be compared with experiments. In alkali-earth species and in Yb, the lack of hyperfine structure suppresses greatly the number of possible collision channels, and provides an excellent opportunity for comparisons with accurate theoretical calculations.

In addition, ytterbium has a high number of natural isotopes: seven stable isotopes, five even and two odd, most with significant abundance. The even isotopes have no angular momentum in the ground state. The two odd isotopes have nuclear spin, allowing us to add the effects of hyperfine structure at will in two different sizes without introducing much change to the system.

2.1 Ytterbium in Traps and Possible Applications

Ytterbium has a structure similar to alkaline-earth species, with two valence electrons closing the s-shell in the ground state. It has an allowed electric dipole transition, $^1S_0$–$^1P_1$, at 399 nm, and a weaker intercombination transition, $^1S_0$–$^3P_1$, at 556 nm.[1]

In recent years, there has been much interest in using the narrow intercombination transitions in the alkaline-earth species as frequency standards. Trapped Mg [Rus98, Mad02], Ca [Cur01, Hol01, Oat99, Sch96, Ude01a, Kur98], and Sr [Ido00, Xu02] have been proposed as candidates, and significant work has gone into understanding the cooling and trapping these species. The same line in Yb is too broad and is not suitable for a clock. However, the highly forbidden $^1S_0$–$^3P_0$ or $^1S_0$–$^3P_2$ transitions are extremely sharp and may be suitable for clocks. To use cold atoms as a frequency standard, it is important to understand frequency shifts and broadening introduced by the trap potentials and collisions among the

[1]The total electron spin, S, must remain unchanged in an electric dipole transition to first approximation, especially in light atoms. Therefore the intercombination transition is a forbidden transition. As atoms get heavier with increasing Z, the stronger spin-orbit interaction mixes spin states, that is, the LS coupling gives way to intermediate coupling. As a result, the lifetimes of the $^3P_1$ get shorter for heavier atoms as can be seen in Table 2.1 (see also p.39 in [Sob92]). Only Sr and Yb can use the intercombination line to hold atoms a MOT. The transition is too weak in Ca and Mg to hold them against gravity.

Table 2.1: The abundance and nuclear spin, transition wavelengths, and lifetimes of $^1S_0$–$^1P_1$ and $^1S_0$–$^3P_1$ transitions of naturally occurring isotopes of Mg, Ca, Sr, and Yb [Lid02].

Isotope	Abundance (%)	Nuclear spin	$\lambda(^1S_0$–$^1P_1)$	$\tau(^1P_1)$	$\lambda(^1S_0$–$^3P_1)$	$\tau(^3P_1)$
^{24}Mg	78.99	0				
^{25}Mg	10.00	5/2	285 nm	2.02 ns	457 nm	5100 μs
^{26}Mg	11.01	0				
^{40}Ca	96.94	0				
^{42}Ca	0.647	0				
^{43}Ca	0.135	7/2				
^{44}Ca	2.086	0	423 nm	4.6 ns	657 nm	398 μs
^{46}Ca	0.004	0				
^{48}Ca	0.187	0				
^{84}Sr	0.56	0				
^{86}Sr	9.86	0				
^{87}Sr	7.00	9/2	460 nm	4.7 ns	689 nm	21 μs
^{88}Sr	82.58	0				
^{168}Yb	0.13	0				
^{170}Yb	3.05	0				
^{171}Yb	14.3	1/2				
^{172}Yb	21.9	0	399 nm	5.5 ns	556 nm	850 ns
^{173}Yb	16.1	5/2				
^{174}Yb	31.8	0				
^{176}Yb	12.7	0				

trapped atoms. Quantitative comparisons between theory and experiments are possible for collisions among alkaline-earth like atoms, whereas hyperfine structure introduces many collisional channels and make calculations very difficult for alkali atoms.

Table 2.1 summarizes the naturally occurring isotopes and their abundance, nuclear spin, wavelengths, and lifetimes for the $^1S_0$–$^1P_1$ and $^1S_0$–$^3P_1$ transitions of Mg, Ca, Sr, and Yb. These atoms have similar electronic structures, with the lifetime of the intercombination line, $^1S_0$–$^3P_1$, decreasing for heavier atoms. Yb has seven naturally occurring isotopes, five even and two odd, and is useful for isotope and hyperfine comparison studies.

2.1.1 Doppler and Sub-Doppler Cooling

Sub-Doppler cooling mechanisms that depend on multiple sub-levels in the ground state such as Sisyphus cooling are absent in the even isotopes of alkaline and Yb atoms because they have no electronic spin or nuclear spin ($I = 0$) in the ground state. Pure Doppler cooling can be studied without being overwhelmed by sub-Doppler cooling mechanisms. The odd isotopes have $I > 0$, and various sub-Doppler cooling mechanisms can be added. Cooling and trapping methods (magnetic traps, for example) that depend on Zeeman shifts of magnetic sublevels are not available to the ground-level alkaline-earth-like atoms because the coupling of a magnetic field with nuclear spin is much weaker than with electron spin.

Radiation cooling of neutral atoms was first predicted in atoms modeled as a two-level system [H$\ddot{\text{o}}$75]. This model imposes a lower limit on the temperatures that can be achieved, called the Doppler limit. It was first achieved in alkali atoms [Chu85]. Careful measurements of the temperature in optical molasses indicated that the atom clouds were much colder than this limit [Let88], and it was soon realized that the multiple sublevels which are always present in alkali atoms must be taken into account to explain this phenomenon. Sisyphus cooling and various other polarization cooling mechanisms were proposed to explain the unexpectedly low temperature [Dal89]. Yb atoms offer systems in which the cooling mechanisms can be separated. Doppler cooling can be studied in the $^1S_0$ ground state of the spin-free even isotopes as a nearly perfect two-level system. A systematic experimental study of the dynamics of a simple two-level atom in a MOT such as temperature and

spring constant were recently done for the first time in Sr [Xu02]. Yb has two odd isotope with nuclear spin, and sublevels can be added at will to study sub-Doppler cooling. These cooling mechanisms are described in Chapter 3. Sub-Doppler cooling in odd isotopes was investigated for this work, and is presented in Chapter 8.

2.1.2 Cold Collisions

The interest in the field of cold and ultracold collisions was renewed as it became necessary to understand the interaction among the cold trapped atoms. The field encompasses a broad range of disciplines including optical manipulation of chemical processes, quantum degenerate gases, precision measurement, and spectroscopy. Precise inter-atomic interactions at short distances are critical in achieving and understanding Bose-Einstein condensation and Fermi degenerate gases. The field is concerned with atoms which are cold enough that their deBroglie wavelengths, λ_{dB}, are as long as chemical bond lengths and the interaction among atoms can no longer be interpreted as classical nuclear point particles with potentials defined by their associated electronic charge distribution. It is also important to understand the collisional mechanisms which cause frequency shifts as the requirements for frequency standards become more stringent.

Low temperature collisions are separated into two temperature regimes, referred to as cold and ultra-cold collisions. The term, cold collisions, generally refers to collisions which occur when the deBroglie length is on the order of chemical bond distances, at temperatures in the range of 1 mK–1 μK. Cold collisions are studied with one or more light fields to confine and probe the atoms, and excited quasi-molecular states play an important role in these studies. As two atoms in their ground state approach each other, they can absorb a photon that is on resonance with an excited molecular state and form a bound excited molecule. These molecules can decay and emit photons at different internuclear separations from the one at which they were created. The difference in the binding energy shows up as kinetic energy of the atoms, causing them to be knocked out of the trap.

Ultracold collisions refer to interactions among atoms which have deBroglie wavelengths on the order of the mean distance between the atoms. They generally occur at temperatures

below the photon recoil limit below 1 μK range between two ground state atoms. No photons are involved in these processes. These collisions are important in evaporative cooling and formation of BECs or Fermi degenerate gases. They are described only in terms of their radial component without angular components, and are characterized by a phase shift or scattering length, a, of the ground state wavefunction. The sign of a determines the stability of condensates: $a > 0$ results in stable condensates, and atoms with $a < 0$ form unstable BECs, where the atomic interaction is attractive and BECs collapse beyond a certain point.[2] A comprehensive review of cold and ultracold collisions can be found in Ref. [Wei99].

There has been much interest from the theory community to study collisions in alkaline-earths [Mac01, Mac02, Der01, Mac99, Tie02]. Because alkalis have complicated hyperfine structures, they have many collisional channels which complicates the comparison between the experimental results with theoretical models. With their simple ground-state structure, alkaline-earths offer an ideal setting to compare theoretical predictions with experiments.

There are two general ways to study cold collisions: one is to study the number-density-dependent loss from the traps via collisions [Wal92, Mar93, Let95, Gen98, Pet94], and the other is to use another source of light and to do photoassociation spectroscopy [Jon96, Wan97, Gar95, McA95, Abr96]. In alkaline-earths, trap-loss collisions were studied in Sr [Din99] and photoassociation spectroscopy was done in Ca [Zin00]. As these papers suggest, there is much to gain from more experimental work on alkaline-earths and Yb. A comprehensive calculation for group II atoms and Yb has been presented in Ref. [Mac01].

2.1.3 Quantum Degeneracy

To create a BEC or Fermi degenerate gas, it is necessary to cool the atoms to the critical temperature at which the de Broglie wavelength of the atoms, λ_{dB}, is roughly the mean distance between the atoms. Therefore, it is important to have a trap with large enough atom number density at low enough temperature. Generally, temperature below the recoil limit

---

[2] ^{7}Li is such a case [Bra95]. It was somewhat of a controversy as to whether BECs could be formed with $a < 0$. A ^{7}Li BEC was achieved by the Hulet group at roughly the same time as the Rb and Na BECs by Ketterle and Wieman, however it was not until later that what they had was recognized as a BEC. This uncertainty is expressed even by the authors in Ref. [Abr95] published earlier in the same year by the Hulet group.

is accomplished by evaporative cooling in magnetic traps. BECs were first accomplished in 1995 in Rb using a TOP magnetic trap [And95], in Li using a biased magnetic trap [Bra95], and in Na using a magnetic trap with an optical plug and radio-frequency-induced evaporative cooling [Dav95b]. More recently, all-optical creation of BECs and Fermi-degenerate gases have been accomplished, as discussed below.

Evaporative cooling relies on elastic collisions to re-thermalize the gas after the trap potential is lowered to let out the hottest atoms. This poses a challenge for achieving quantum degeneracy for fermions in magnetic traps because Fermi-Dirac statistics prohibit spin-polarized identical fermions from occupying the same space, and prevents effective re-thermalization in the evaporative cooling process. The first Fermi degenerate gas was produced in 1999 at JILA with ^{40}K by trapping two spin states of the same isotope in a magnetic trap, using a dual radio-frequency-knife method [DeM99].

Yb and alkaline-earth atoms have no electronic sublevels in the ground state, and they must be pumped into metastable states if one wants to trap them in a magnetic trap [Der01, Lof02a, Nag03]. However, once in a metastable state, they lose their advantage of being different from the well-studied alkali-metals. Evaporative cooling is also possible in far-off resonant traps. Quantum degeneracy had eluded the earlier efforts using all optical traps due to density-dependent heating and losses from the laser cooling techniques, residual heating in optical dipole traps, or conditions unfavorable for evaporative cooling. It is only recently that these technical difficulties were solved and all-optical BEC has been accomplished in a crossed-beam optical dipole trap in Rb [Bar01], and in a single focused beam degenerate Fermi gas in ^{6}Li [Gra02], both with a CO_2 laser.

In Yb, high atom density of $10^{14}\,\mathrm{cm}^{-3}$ at a temperature of $100\,\mu$K has been achieved in a crossed optical dipole trap [Tak03], and phase-space density exceeding 0.1 (where a density of 1 is required for BEC) has been achieved in a FORT in Sr [Ido00]. A Bose-Einstein condensate, Fermi-degenerate gas, or a mixture of both would be highly interesting in Yb. The simple ground state structure allows for simple theoretical modeling, and the abundance of isotopes in Yb can be used for mixtures of quantum degenerate bosons and fermions, opening many interesting possibilities.

2.2 *Electric Dipole Moment and Time-Reversal Symmetry*

Until the recent measurement of the CP asymmetry in B-mesons by the BaBar collaboration at SLAC (Stanford Linear Accelerator) [Aub01] and Belle collaboration at KEK (Kou-Enerugii Butsurigaku Kenkyusho, Japanese for high energy physics laboratory) [Aba01], the only evidence for CP-violation was in the K-meson decay measured in 1964 by Christenson, Cronin, Fitch and Turlay [Chr01]. The CP-violation in both of these processes can be described by the Standard Model. There is a strong belief, however, that the Standard Model is not complete: it cannot explain the gauge hierarchy, gravity, or the matter–antimatter asymmetry in our Universe. Many extensions to the Standard Model such as supersymmetry (SUSY), multi-Higgs, and left-right symmetry models have been proposed to explain these phenomena. The existence of a permanent EDM would violate T- and P-symmetry, and by CPT invariance, leads to CP violation. The Standard Model predicts EDMs in atoms which are smaller than the current experimental sensitivity. However, the high accuracy null results of EDM experiments have set stringent limits on the possible extensions to the Standard Model.

The observation of a permanent EDM would violate T- and P-symmetry. This symmetry violation manifests itself in the interaction of the atoms with electric and magnetic fields. If atoms have a permanent electric dipole moment (d) and magnetic dipole moment (μ), they will respond to external electric and magnetic fields, $\mathbf{E}$ and $\mathbf{B}$, according to the Hamiltonian,

$$H = -(d\mathbf{E} + \mu\mathbf{B}) \cdot \frac{\mathbf{F}}{\mathrm{F}} \tag{2.1}$$

where $\mathbf{F}$ is the total atomic angular momentum. Under T-reversal, $\mathbf{B}$ and $\mathbf{F}$ change signs but $\mathbf{E}$ does not. Reversing $\mathbf{E}$ relative to $\mathbf{B}$ mimics a T-reversal operation. The experimental observable is the change in Zeeman frequencies associated with this flip in the fields. If an EDM exists, it has to be aligned with the spin of the atom since the perpendicular components will average to zero. The shot-noise-limited uncertainty in the measured EDM in these experiments is

$$\delta d = \frac{\hbar}{2E_{eff}\sqrt{\tau NT}} \tag{2.2}$$

where E_{eff} is the magnitude of the effective applied electric field, τ is the coherence time,

N is the number of atoms under investigation, and T is the total measurement time. To ensure a low shot-noise limit, it is important to make E_{eff}, τ, N, and T as large as possible.

There are a number of ways in which to look for permanent electric dipole moment in neutrons, diamagnetic or paramagnetic atoms or molecules. I will focus mainly on atoms here. Generally, experiments using diamagnetic atoms (atoms having paired electrons) are sensitive to T-violation coming from hadronic (quark-quark) interactions, and paramagnetic atoms (with unpaired electron) are sensitive to the leptonic sources of T-violation. Both are sensitive to semi-leptonic (electron-quark) interactions. These experiments are generally conducted on samples of neutrons, atoms, or molecules in cells (bottles) or in beams. A good reference on this subject is a book by Khriplovich and Lamoreaux [Khr97].

In searching for an EDM in paramagnetic or diamagnetic atoms, heavy atoms are preferred since the size of an EDM is enhanced with Z, and the best limits have been set by thallium (Tl, Z = 81) and mercury (Hg, Z = 80) respectively. For diamagnetic atoms, isotopes with nuclear spin of 1/2 are preferred because many systematic effects that can arise from Stark shifts or quadrupole interactions are not present. Isotopes of diamagnetic atoms with nuclear spin are limited, and searches for EDM have been conducted in ^{129}Xe [Ros01] and ^{199}Hg [Rom01a]. ^{3}He also has $I = 1/2$; however, the size of an EDM is expected to be much smaller since it is a light atom.

2.2.1 EDM in Cells and Beams

Traditionally EDM experiments have been conducted with gases confined in cells or atomic beams. They have their advantages and disadvantages, and an Yb experiment in an optical trap combines the positive aspects from both. The disadvantage to such an experiment comes from the technical difficulties in holding enough atoms in a trap for a long enough time.

The advantage of a cell is that one can sample a large number of atoms, and depending on the species, a long coherence time of spin polarization can be achieved. However, collisions with walls of the cells limit the spin coherence time. The electron spin in paramagnetic atoms is much more easily disturbed by the collisions, and the longest coherence times achieved are

around 20 ms [Mur89]. In diamagnetic atoms the nuclear spin polarization is more stable against collisions, and coherence times of up to 300–500 s or more are possible [Rom01a]. Small leakage currents invariably flow when high voltage is applied to insulators which generate magnetic fields that are correlated with the direction of the applied electric field. The signal detected is indistinguishable from that of an EDM, and is a major source of systematics in cell experiments. The best limit for diamagnetic atoms is set by the Hg experiment at the University of Washington [Rom01a]. The measurements give $d(^{199}\mathrm{Hg}) = -(1.06 \pm 0.49 \pm 0.40) \times 10^{-28} e\,\mathrm{cm}$, with an upper limit of $|d(^{199}\mathrm{Hg})| < 2.1 \times 10^{-28} e\,\mathrm{cm}$. This result sets the most stringent constraints on many of the model-independent parameters in hadronic and semileptonic CP-violating effects, and some of the model-specific parameters in extensions to the Standard Model [Ber91, Bar93b].

In beam experiments, higher electric field can be applied to the atoms as these experiments are conducted in ultra high vacuum. The atoms are confined in a well-defined narrow beam and electric fields exceeding 100 kV/cm can be applied. A major source of systematics for a beam experiment is the motional magnetic field, $\mathbf{E} \times \mathbf{v}/c^2$. Because the atoms in a beam are moving rapidly, the usable coherence time is short. The latest result for paramagnetic atoms comes from the Tl beam experiment at the University of California at Berkeley which used an electric field of 123 kV/cm. In this version of the experiment, sodium was used as a co-magnetometer. Their measurement of the electron EDM of $d_e = (6.9 \pm 7.4) \times 10^{-28} e\,\mathrm{cm}$ yields an upper limit of $|d_e| \leq 1.6 \times 10^{-17} e\,\mathrm{cm}$, consistent with a zero EDM [Reg02].

2.2.2 EDM Searches in Traps

An EDM measurement of atoms in traps would combine the advantages of both beam and cell experiments. Because the trapped atoms are confined in a small volume in ultra-high vacuum, it is possible to apply a high electric field without having to worry about the leakage currents of cells. The inhomogeneity of magnetic and electric fields will be small. In addition, an EDM experiment with trapped atoms will have much longer coherence times than in beam experiments.

Far-off resonance traps (FORT) [Chu86, Mil93] offer an environment desirable for pre-

cision measurements since the perturbation to the atomic energy levels from such a trap is minimal. A detailed study of the Zeeman shift induced by dipole traps for Hg and Cs as examples of diamagnetic atoms and paramagnetic atoms respectively is described in Ref. [Rom99]. Much of the work on traps has been done on alkali atoms, and although they are paramagnetic, these systems are instructive for learning what is possible in traps. An EDM measurement has been proposed for Cs in which a coherence time of 4 s has been achieved [Dav95a]. The role of collisions in such a measurement has been studied in Cs [Bij94]. The behavior of spin-polarized Rb atoms in a FORT has been studied, and 98% polarization of 4×10^6 atoms with a coherence time of 10 s has been obtained in ^{85}Rb [Cor99].

For our experiment, we chose ytterbium for several reasons: Yb has a structure much like Hg, in which our group has developed an extensive expertise. It has a closed S-shell electronic ground state, $^1S_0$, and the ^{171}Yb isotope has a nuclear spin of $I = 1/2$, a condition favorable for sensitive measurements of atomic EDMs. The expected size of EDM in Yb is three times smaller than Hg EDM due to its smaller size with Z = 70 compared to Z = 80 of Hg [Das02, Das96]. However, Yb has the advantage that the $^1S_0$–$^1P_1$ and $^1S_0$–$^3P_1$ transitions at 399 nm and 556 nm are accessible for laser cooling and trapping (see Chapter 6). The corresponding lines in Hg are at 254 nm and 185 nm, and lasers with enough power at these wavelengths are difficult to achieve, especially at 185 nm.

For this experiment, an ultimate experimental sensitivity of $10^{-29}e$ cm was proposed for Yb. To achieve this sensitivity, it is necessary to have an electric field of $E = 100$ kV/cm, $N = 10^8$ trapped atoms, $\tau = 100$ s of coherence time, and $T = 100$ days of measurement time. To meet these conditions, efficient loading of the atoms into a FORT and ultra-high vacuum on the order of 10^{-12} Torr are essential conditions. Figure 2.1 shows the experiment setup of the FORT and the relative field orientations that would minimize the systematic error due to the FORT laser [Rom99].

More than 10^8 Yb atoms have been trapped in the green MOT by the Yabuzaki group at Kyoto University [Kuw99]. They have also trapped 3×10^6 ^{174}Yb atoms in a crossed dipole trap, with 2×10^5 concentrated in the crossed FORT region [Tak03]. Their trap lifetime seems to be limited by collisions with background gas, and by improving the vacuum and

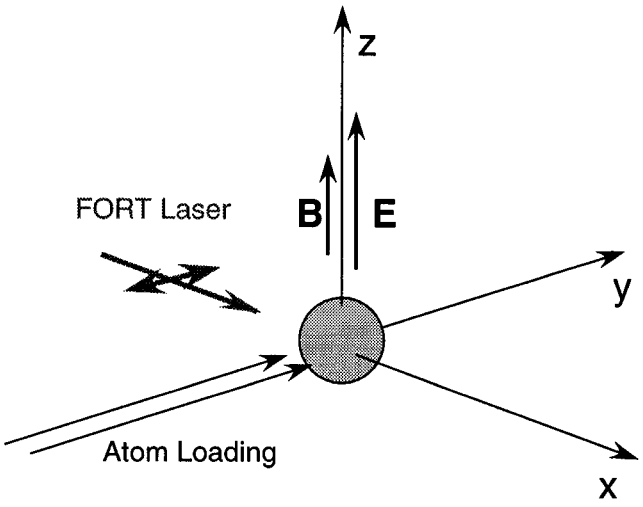

Figure 2.1: Relative field orientation of an EDM experiment for trapped atoms that minimize systematic error due the trap laser. The laser propagation and polarization are perpendicular to the applied magnetic and electric fields.

transfer efficiency, it is likely that the number of trapped atoms can be increased. Transfer of atoms from a MOT to an optical dipole trap has been accomplished with an efficiency of up to 40% with Rb atoms [Kup00] and 80% in Sr [Ido00]. Trap lifetimes of up to 300 s have been achieved with an ultrastable CO_2 laser with trap depth of 0.4 mK in fermionic ^{6}Li by O'Hara et al. [O'H99]. Because the usual spin relaxation mechanisms found in cells are absent, coherence times close to the trap lifetimes are expected.

There are other precision experiments under way that use trapped atoms to probe fundamental symmetries and weak interactions. These include the effort on parity nonconservation in atomic francium [Sim96, Spr02] and beta-decay experiments at TRIUMF [Beh97, Gor00] and the national laboratories in Berkeley [Vet01] and Los Alamos [Cra00].

2.2.3 New EDM Experiments

In recent years, several research groups have started to explore new EDM experiments. The liquid xenon (^{129}Xe) experiment at Princeton takes advantage of the large number of atoms available in the liquid ($N \sim 10^{22}\,\mathrm{cm}^{-3}$), high electric field breakdown strength of

400 kV/cm, and long coherence time of 1300 s [Rom01b]. The statistical limit in the EDM sensitivities of this experiment is $10^{-36} e$ cm, and the proposed experimental sensitivity is in the range of $|d(^{129}\mathrm{Xe})| < 10^{-31}$ to $10^{-33} e$ cm.

Paramagnetic molecules offer new possibilities in the search for electron EDMs. The large polarizability of polar molecules can greatly enhance the EDM, and large polarization can be achieved with modest external fields. The observable energy shifts caused by an electron EDM may be 100–1000 times greater than in paramagnetic atoms. There are two ways to obtain paramagnetic molecules: by using molecules that are paramagnetic in their ground states (e. g. HgF or YbF), or by populating a paramagnetic state of a molecule which is diamagnetic in the ground state (e. g. PbO). The former is thermally and chemically unstable (chemical radicals), and the experiments must be carried out in beams. For these reasons, it is difficult to achieve a high production rate [Hin97, Sau95, Sau96]. Although the reported sensitivity level does not yet reach the sensitivity of Hg or Tl experiments, a measurement has been published on YbF of $d_e = (-0.2 \pm 3.2) \times 10^{-26} e$ cm, limited by counting statistics, with the future possible sensitivity level of $1 \times 10^{-27} e$ cm [Hud02].

The second approach, using diamagnetic molecules that are pumped to a paramagnetic state, has the advantage that the molecules are thermally and chemically stable. The molecules can be stored in a cell, which gives this experiment a large advantage in sensitivity due to the large number of molecules. With a proposed ultimate sensitivity of $|d_e| < 10^{-31} e$ cm, the EDM limit can be improved by 4 orders of magnitude below the current limit set by the Tl experiment [DeM00].

Yet another experiment has been proposed for a search for electron EDM in a solid by Lamoreaux [Lam02]. There were unsuccessful attempts in the past, but with the improvements in the technology in superconducting quantum interference device (SQUID) and advancement in solid state materials, this experiment hopes to achieve an EDM sensitivity of $10^{-32} e$ cm, 5 orders of magnitude improvement over current experimental limits.

Chapter 3

LASER COOLING AND TRAPPING

In this chapter, I will describe some fundamental concepts of laser cooling and trapping. For brevity, I will primarily focus on the features which are directly relevant to this work. For more introduction and details, I refer to a comprehensive book meant as an introduction to the subject of laser cooling and trapping by Metcalf and van der Straten [Met99]. Much of the earlier work is also listed in the resource letter by Newbury and Wieman [New96] and the November issue of the Journal of the Optical Society of America B (vol. 6, no. 11) contains much of the pivotal work on sub-Doppler cooling in optical molasses.

The early picture of laser cooling involved a simple two-level atom. Sub-Doppler cooling was discovered when the pioneers of laser cooling noticed that the temperature in their traps were lower than what was thought to be the lowest temperature achievable using laser cooling techniques: the Doppler limit. It was found that having multiple sublevels in the ground state dramatically enhances laser cooling and temperatures much lower than the Doppler limit can be achieved.

In Yb, these effects of Doppler and sub-Doppler cooling can be isolated. The ground state has a closed s-shell structure and zero electronic spin. The even isotopes also have no nuclear spin which means that there is no hyperfine structure, therefore no sub-levels in the ground state. The cooling transitions are completely closed, and can accurately be modeled as a two-level system. The odd isotopes, ^{171}Yb with $I = 1/2$ and ^{173}Yb with $I = 5/2$, have additional sublevels in the ground state due to the nuclear spin.

The chapter starts out with the description of how one can apply forces on neutral atoms. Methods of Doppler cooling and trapping with focus on Zeeman slowing of atomic beams and magneto-optical trapping (MOT) which are used in this work are described in Sections 3.2 and 3.3. In Section 3.4, the sub-Doppler cooling mechanisms in one-dimension as well as three-dimensions are described.

3.1 Force on Neutral Atoms

There are three general categories of forces that are widely used to trap atoms: optically induced electric dipole force, magnetic dipole forces, and radiation pressure. Of these three, radiation pressure is perhaps the most robust and versatile as it also provides cooling. The other two forces are conservative: they provide ways of holding the atoms, but they have no way of dissipating excess kinetic energy. The atoms generally need to be pre-cooled by other methods such as Doppler cooling before they are loaded into conservative traps. In this section, I will briefly discuss all three forces, and the rest of this chapter will focus on the radiation pressure as it is relevant to the work presented in this dissertation.

3.1.1 Optical Dipole Traps

The optical dipole force relies on the dipole interaction between an optical field and the induced electric dipole moment of atoms. Atoms experience light shift when immersed in optical fields. If the optical field is lower in frequency than the atomic resonance, two states which are coupled via electric dipole repel each other, and the ground state energy is shifted down. Atoms immersed in a laser field which is tuned below atomic resonance are attracted toward higher laser intensities. The opposite is true if the optical field is higher in frequency, and atoms are repelled from locations with higher laser intensities.

The simplest configuration for a red-detuned optical dipole trap is a tightly focused Gaussian laser beam as depicted in Figure 3.1 [Chu86]. For sufficiently large laser detuning, $|\delta|$, the scattering rate is significantly reduced and the force from radiation pressure is negligible: the radiation pressure decreases as $1/\delta^2$ for $\delta \gg \Omega$ (see Section 3.1.3) whereas the dipole force decreases only as $1/|\delta|$. In red-detuned dipole traps, atoms are trapped at the focus of the Gaussian beam. Traps have been realized for very large detunings with 10.6 μm CO_2 lasers [Mil93], and in these traps the perturbation to the atoms is much smaller than in MOTs or magnetic traps and suitable for precision measurements as described in Section 2.2.2 and Refs. [Rom99, Dav95a, Bij94]. For tighter confinement, crossed-dipole traps are used. Optical dipole traps are conservative traps and have no ability to cool atoms. Therefore it is necessary to pre-cool the atoms in an optical molasses or a MOT

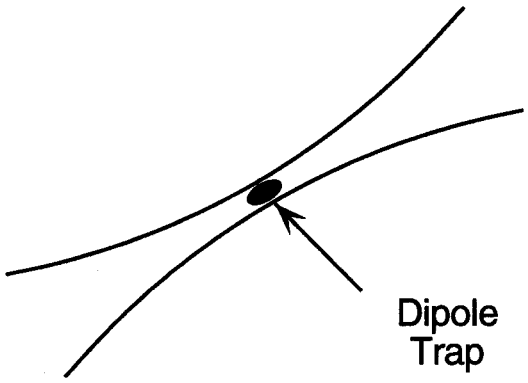

Figure 3.1: A single-focused Gaussian beam forming a dipole trap. Atoms can be trapped at the focus if the beam is red-detuned.

before loading them into a dipole trap. Pointing stability of the laser is crucial to obtain long lifetimes because spatial jitter in the trap laser can heat up the atoms [Sav97]. Trap lifetime of 300 s has been achieved in lithium [O'H99].

In the red-detuned far-off resonance limit, the potential created by dipole traps is described solely through the dc coupling of the laser field and static atomic polarizability, α. The trap potential is

$$U = -\frac{1}{2}\alpha |E_{rms}|^2 \tag{3.1}$$

where E_{rms} is the rms electric field amplitude of the laser, and the force on the atoms is the spatial gradient of the potential. Ytterbium has an atomic polarizability of $\alpha = 21.0 \times 10^{-24}\,\mathrm{cm}^2$ [Lid02]. A 40 W CO_2 laser focused to a 50 μm waist would create an intensity of $I = 2\,\mathrm{MW/cm}^2$, and the trap potential would be roughly 300 μK. The scattering rate is calculated from

$$\sigma_s = \frac{8\pi}{3}\alpha_g^2 k^4 \tag{3.2}$$

where α_g is the polarizability of an atom in the ground state [O'H99]. An Yb atom in this trap would scatter only one photon every 2500 s.

Although the trapping mechanism itself does not have a built-in cooling, evaporative cooling can be used once the atoms are in the dipole trap. The procedure is similar to

what is done in magnetic traps: once the atoms are trapped, the potential is lowered by quickly by decreasing the laser power to let out some of the hottest atoms (this can be done, for example, by using an AOM). Then the trap potential is raised again to let the atoms rethermalize by elastic collisions (inelastic collisions result in trap loss). By repeating these steps, the temperature of the remaining atoms can be reduced significantly. This procedure is lossy so it is advantageous to have a cold set of atoms as a starting point. Bose-Einstein condensation [Bar01] and Fermi-degenerate gases [Gra02] have been achieved by all-optical means in crossed dipole traps. The Yabuzaki group at Kyoto University in Japan has trapped 10^5 Yb atoms in a crossed-dipole trap consisting of an argon-ion laser [Tak03]. Their trap has a temperature of $100\,\mu$K and density as high as $4.7 \times 10^{14}\,\mathrm{cm}^{-3}$ has been observed, but their system is still far from quantum degeneracy.

3.1.2 Magnetic Trapping

Magnetic trapping uses the same principle as the Stern-Gerlach experiment where the magnetic moment of an atom interacts with a magnetic field gradient. The force on the atoms from this interaction is

$$\vec{F} = \vec{\nabla}(\vec{\mu} \cdot \vec{B}) \tag{3.3}$$

where $\vec{\mu}$ is the magnetic moment of the atom. In alkali-metals, magnetic traps are generally formed with a magnetic quadrupole field produced by a pair of magnet coils with current running in the opposite direction (see Figure 3.2). The field has a minimum in the center, with the magnitude of the field increasing in all directions away from the center. The sign of the field gradient along the radial direction is opposite that of the axial direction.

Magnetic traps are also conservative, and atoms are usually first cooled in a MOT before they are loaded into magnetic traps. To reach low temperatures required for quantum degeneracy, atoms are cooled by forced evaporation in magnetic traps in most cases. To avoid spin-exchange collisions which can lead to trap-loss, only the atoms in a single spin state are loaded. This poses a problem for evaporative cooling of fermions because Fermi-Dirac statistics prohibits s-wave collisions between two identical fermions. The first Fermi-degenerate gas was formed by clever mixture of two spin states of ^{40}K [DeM99].

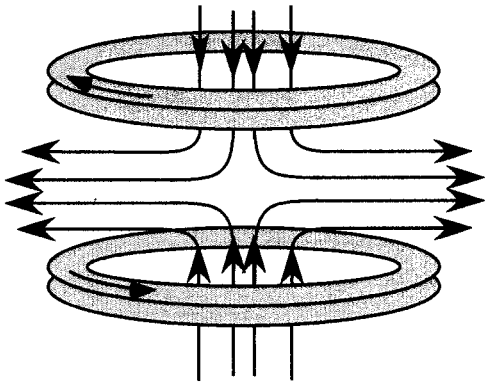

Figure 3.2: Magnetic quadrupole field produced by a set of anti-Helmholtz coils.

Yb and alkaline-earth atoms cannot be magnetically trapped in the ground state since $\vec{\mu}$ comes only from the nucleus. The magnetic moment of the nucleus, $\vec{\mu}_N$, is roughly 2000 times smaller than the electron magnetic moment, $\vec{\mu}_e$. These atoms, however, have a metastable state, $^3P_2$, that can be used for magnetic trapping [Lof02a], recently accomplished in Sr [Nag03] and in Ca [Han03].

3.1.3 Radiation Pressure and Doppler Cooling

Radiation pressure relies on momentum transfer from photons to atoms by the process of resonant absorption and spontaneous emission. An atom moving at velocity v immersed in a near resonant light field experiences a force which is the product of the momentum of the photons and the rate at which the absorption occurs:

$$\begin{aligned} \vec{F} &= (\text{photon momentum}) \times (\text{absorption rate}) \\ &= \frac{\hbar\vec{k}\gamma}{2}\left(\frac{I/I_s}{1+I/I_s+(2(\delta \pm kv)/\gamma)^2}\right) \end{aligned} \tag{3.4}$$

where $\vec{k}$ is the wave vector of the laser, γ is the transition rate, δ is the laser detuning, I is the laser intensity, and I_s is the saturation intensity. By adjusting δ, it is possible to create a condition such that the atoms preferentially absorb photons that are propagating in a certain direction. The maximum force that can be applied to atoms is determined by

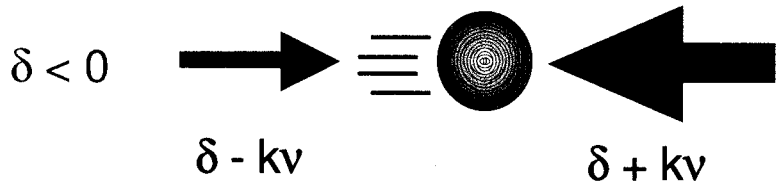

Figure 3.3: Doppler cooling. A red-detuned laser will exert a stronger force if the atom is moving in the opposite direction.

the spontaneous decay rate, γ,

$$\vec{F}_{max} = \hbar\vec{k}\gamma/2 \tag{3.5}$$

where $|\vec{k}| = 2\pi/\lambda$. The maximum acceleration that the atom can experience is $\vec{a}_{max} = \vec{F}_{max}/M$. Trapping neutral atoms using this force was first described in [Ash78].

Thermodynamics dictates that a cooling process be both dissipative and irreversible. In laser cooling, kinetic energy of the atoms is dissipated into the laser field because the photons being emitted have a higher energy than those that were absorbed. The reliance on spontaneous absorption and emission makes the process irreversible.

Cooling occurs when the energy loss is velocity dependent. The force on atoms can be written as

$$F = -\beta v \tag{3.6}$$

where β is the damping coefficient. In Doppler cooling, the laser is red-detuned from resonance so that atoms which are moving opposite to $\vec{k}$ see the laser frequency which is blue shifted and closer to resonance. This makes it more likely for absorption to occur when the atoms are moving in the opposite direction as the laser beam than when they are moving in the same direction. When the atoms decay to the ground state by spontaneous decay, photons are emitted in random directions, and the net force applied on the atoms over many cycles is in the opposite direction to their velocity. Because the photons emitted are greater in energy than the photons absorbed, there is a net loss in kinetic energy, resulting in cooling. Other cooling mechanisms such as Sisyphus cooling and other polarization cooling also rely on this process of preferential absorption followed by shedding kinetic energy into

the optical field. These processes are discussed more in detail in Section 3.4.

3.2 Deceleration of Atomic Beam: Zeeman Slower

Our sample of Yb atoms is produced in a hot oven at 673 K (400 °C). The MOT we use has a capture range of only 2.8 K, and we employ a Zeeman slower to increase the number of atoms within the capture range. The details of the oven design and atomic beam creation are discussed in Section 5.1.2.

A sample of gas that is in thermal equilibrium has a Maxwell-Boltzmann velocity distribution,

$$f(v) = \sqrt{\frac{2}{\pi}}\frac{v^2}{\tilde{v}^3}\exp\left(-\frac{v^2}{2\tilde{v}^2}\right), \tag{3.7}$$

where $\tilde{v} = \sqrt{k_B T/M}$. The most probable velocity in this distribution is $v_{mp} = \sqrt{2}\tilde{v}$, $v_{ave} = \sqrt{(8/\pi)}\tilde{v}$ is the average velocity, and $v_{rms} = \sqrt{3}\tilde{v}$ is the root mean square velocity. In an atomic beam, the distribution is slightly modified, and has the form,

$$f_B(v) = \sqrt{\frac{v^3}{2\tilde{v}^4}}\exp\left(-\frac{v^2}{2\tilde{v}^2}\right) \tag{3.8}$$

where v is now the velocity of the atoms in the direction along the beam (see Ref. [Ram56] for more details on molecular beams). Figure 3.4 shows the normalized velocity distribution in a molecular beam with $\tilde{v} = 1$. Just as in the three-dimensional Maxwell-Boltzmann distribution, the beam is described by characteristic velocities: $v_{mp} = \sqrt{3}\tilde{v}$, $v_{ave} = \sqrt{9\pi/8}\tilde{v}$, and $v_{rms} = 2\tilde{v}$. An Yb beam emerging from an oven at 400 °C has $v_{mp} = 310\,\mathrm{m/s}$, $v_{ave} = 336\,\mathrm{m/s}$, and $v_{rms} = 358\,\mathrm{m/s}$.

A Zeeman slower consists of a circularly polarized laser beam counterpropagating with the atomic beam and a magnetic field gradient along the beams. The laser is tuned below resonance so that it is near resonance with the fast atoms emerging from the oven with Doppler shift of $\omega_D = -\vec{k}\cdot\vec{v}$. Each optical transition causes a change in the atomic velocity by the recoil velocity, $v_r = 0.57\,\mathrm{cm/s}$. As the atoms undergo many optical transitions, the Doppler shift changes, and they will eventually fall out of resonance.

There are several ways to keep the atoms in resonance with the slowing laser: using white light in which there are many frequency components to the slowing laser, chirping

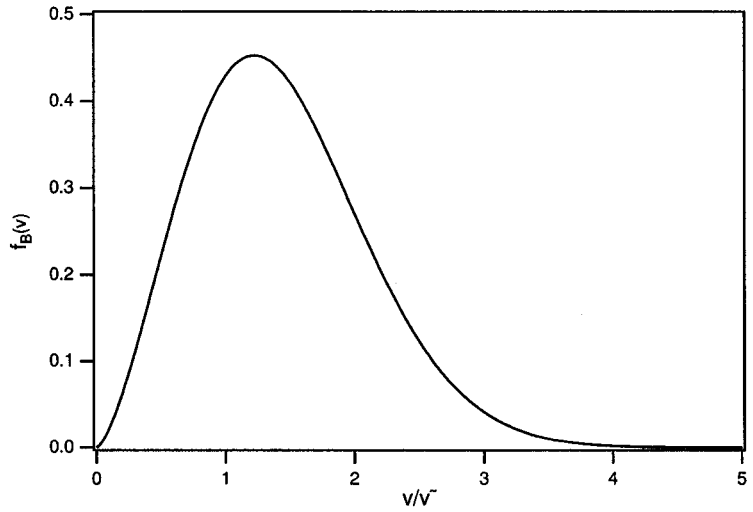

Figure 3.4: Velocity distribution for an atomic beam with $\tilde{v} = 1$.

the laser frequency at the same rate as the atoms are slowing down, or shifting the atomic resonance frequency itself using a magnetic field gradient to compensate for the changing Doppler shift. The third option is the Zeeman slower, chosen in this experiment and in many others as the most simple and reliable method.

A magnetic field gradient which gives a constant deceleration along position, z, is

$$B(z) = B_0\sqrt{1 - z/z_0} \tag{3.9}$$

where $z_0 = Mv_0^2/\eta\hbar k\gamma$ is the total length of the magnet, for which $B_0 = \hbar k v_0/\mu'$, $\mu' \equiv (g_e M_e - g_g M_g)\mu_B$, $g_{g,e}$ are the Landé g-factor of the ground and excited states, $M_{g,e}$ are the magnetic quantum numbers, μ_B is the Bohr magnetron, and $\eta < 1$ is a design parameter that determines the overall length of the magnet, z_0. The minimum length required to stop the atoms from temperature T is

$$L_{min} = \bar{v}^2/2a_{max} \tag{3.10}$$

where $\bar{v} = 2\sqrt{k_B T/M}$. The minimum time required is

$$t_{min} = \bar{v}/a_{max}. \tag{3.11}$$

Table 3.1: Parameters of interest for slowing atoms in an atomic beam. The oven temperatures for the alkalis were chosen to give a vapor pressure of 1 Torr. T_{oven} for Yb is the typical operating temperature.

Atom	T_{oven} (K)	$\bar{v}$ (m/s)	L_{min} (m)	t_{min} (ms)
H	1000	5000	0.012	0.005
Li	1017	2051	1.15	1.12
Na	712	876	0.42	0.96
K	617	626	0.77	2.45
Rb	568	402	0.75	3.72
Cs	544	319	0.93	5.82
Yb ($^1S_0$–$^1P_1$)	673	358	0.12	0.7
Yb ($^1S_0$–$^3P_1$)	673	358	27	150

Table 3.1 lists these parameters for Yb and some alkali atoms. A more complete list can be found on p. 76 in Ref. [Met99].

Several measures were taken to ensure efficient MOT loading. Yb has the advantage that the $^1S_0$–$^1P_1$ transition is stronger than the cooling transitions used in alkalis. The minimum length required for the Zeeman slower is shorter, therefore the transverse spread in the atomic beam is less of a problem. We employ a magnetic field gradient that decrease in the direction of the atomic beam. We have also added an overall bias to the magnetic field gradient so that the atoms in the MOT are not in resonance with the slower beam, to ensure that the atoms in the trap are not affected by the Zeeman slower laser. The minimum length required for a Zeeman slower using the weaker intercombination line is $L_{min} = 27\,\mathrm{m}$, and is completely impractical.

3.3 Doppler Cooling in Optical Molasses and Magneto-Optical Traps

Atoms can be cooled in three-dimensions using an optical molasses which consists of three pairs of counterpropagating beams which are orthogonal to each other. Addition of a

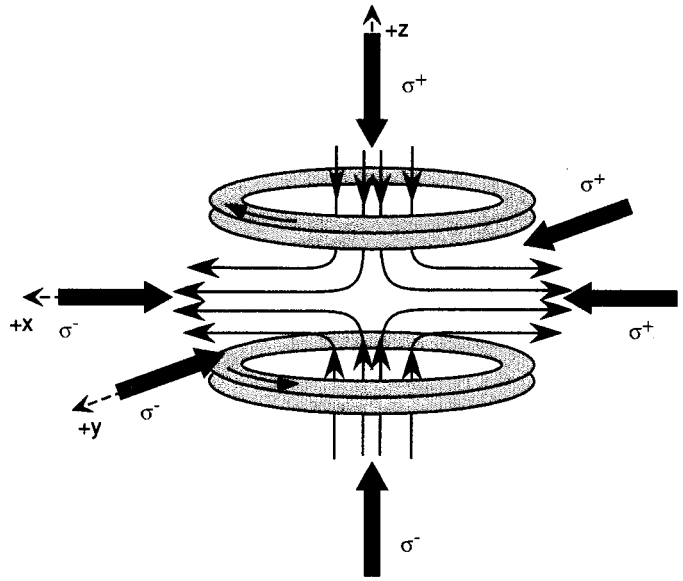

Figure 3.5: Schematic of a MOT including the field-producing coils, the six laser beams, and magnetic-field gradient. The black lines represent the magnetic field gradient produced by the anti-Helmholtz coils, the dashed lines are the axis against which the circular polarizations are defined.

magnetic quadrupole field and polarizing the laser beams in a σ^+–σ^- configuration forms a MOT as sketched in Figure 3.5. The magnetic quadrupole field is very much like that of magnetic traps, although the required gradient for MOT is much smaller. The lasers are red-shifted and circularly polarized such that in addition to Doppler cooling, there is a position dependent force that tends to push the atoms toward the middle of the trap.

The force in the trap adds a position dependent component to Equation 3.6, and if we take one of the dimensions, the force is

$$F = -\beta v - \kappa x \tag{3.12}$$

where β, the damping coefficient, comes from the Doppler cooling and κ is a spring constant that comes from the position dependent absorption of photons with the correct $\vec{k}$ direction.

In a MOT, the red-detuning of the laser serves two purposes. The first is to cool the atoms via Doppler cooling as described in Section 3.1.3. The second is to introduce a position-dependent force on the atoms. To understand how this works, consider an atom

with $J_g = 0 \rightarrow J_e = 1$. Figure 3.6 shows a schematic of the position dependent energy levels of such an atom in a magnetic field gradient formed by a MOT.[1] The magnetic-field gradient separates the magnetic sublevels in the excited state. With the two counterpropagating laser beams circularly polarized in the σ^+-σ^- configuration, atoms displaced from the center are more likely to absorb photons that tend to apply a force toward the center.

Consider the force in the x-direction. An atom displaced from the center by a small distance of x moving with velocity v_x experiences a force that is the sum of the forces from the two laser beams polarized σ^+ and σ^-,

$$F_x = F_+ + F_- \tag{3.13}$$

where F_+ and F^- are the forces from each of the two laser beams, and

$$F_\pm = \pm\hbar k \left[\frac{(I_x/I_s)(\gamma/2)}{1 + I_t/I_s + (2\delta_\pm/\gamma)^2}\right], \tag{3.14}$$

where I_x is the intensity of the light in the x-direction, I_t is the total intensity of all of the laser beams. $\delta_\pm$ is the effective laser detuning for each laser beam given by

$$\delta_\pm = \delta \mp \vec{k} \cdot \vec{v} \pm \mu'(\partial B/\partial x)x/\hbar. \tag{3.15}$$

By expanding the force in powers of x,

$$F_x = F_{x0} + x \left.\frac{\partial F}{\partial x}\right|_{x_0} + \cdots, \tag{3.16}$$

we derive the spring constant in x-direction, $\kappa_x = \partial F/\partial x|_{x_0}$, for atoms in equilibrium: $F_{x0} = 0$ [Xu02]. For the simple case of $J_g = 0 \rightarrow J_e = 1$ example described here,

$$\kappa_x = 4\hbar k \left(\frac{\partial B}{\partial x}\right) \mu_B g_e \frac{I_x}{I_s} \left[\frac{\delta_-/\gamma}{(1 + I_t/I_s + (2\delta_-/\gamma)^2)^2} + \frac{\delta_+/\gamma}{(1 + I_t/I_s + (2\delta_+/\gamma)^2)^2}\right]. \tag{3.17}$$

For sufficiently cold and small trapped clouds of atoms, the effective detuning $\delta_\pm$ reduce to δ and Equation 3.17 simplifies to

$$\kappa_x = 8\hbar k \left(\frac{\partial B}{\partial x}\right) \mu_B g_e \frac{I_x}{I_s} \left[\frac{\delta/\gamma}{(1 + I_t/I_s + (2\delta/\gamma)^2)^2}\right]. \tag{3.18}$$

[1] All J's here can be replaced by the hyperfine quantum number, F, in this discussion. However, I will use J so as not to be confusing with F used for forces.

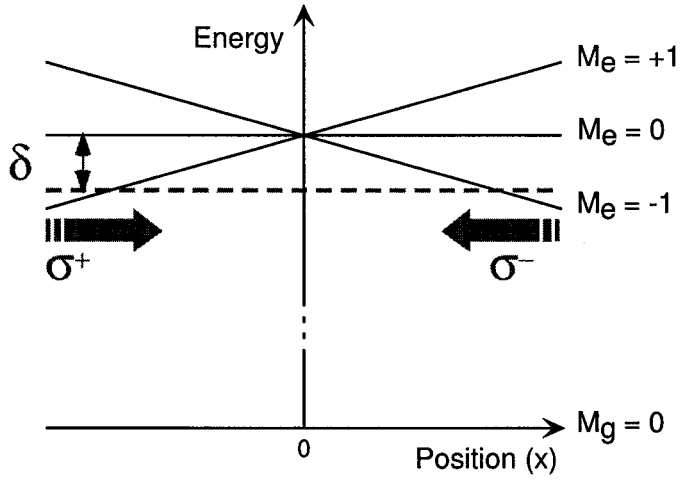

Figure 3.6: One dimensional schematic of a MOT for a $J_g = 0 \rightarrow J_e = 1$ transition. The laser is tuned at the red-dashed line, at $\omega_a - \delta$. The magnetic sublevels are split in the magnetic field gradient, making it more likely for the atoms to absorb the red-detuned photons that tend to push them toward the center of the trap.

For clouds with low enough number density such that their optical density is less than unity, the resulting spatial distribution is Gaussian: $n = n_0 e^{-(r/a)^2}$. Clouds with higher density will approach a uniform density across the volume as effects of radiation trapping become more dominant.

The atoms in optical molasses come to an equilibrium temperature when there is a balance between heating and cooling from the optical fields. The process is analogous to gases being in equilibrium with the surrounding container, and the resulting velocity distribution is Maxwell-Boltzmann in Equation 3.7. Temperature can be defined in terms of the kinetic energy in the system. In one-dimension, the kinetic energy, temperature and velocity are related by

$$\begin{aligned}\langle E_k \rangle &= \frac{1}{2} k_B T \\ &= \frac{1}{2} M \bar{v}^2\end{aligned}$$

and the right-hand side should be multiplied by the degrees of freedom when appropriate.

The competition between cooling and heating can be described by the damping force from the light and diffusion in momentum, which comes from the random nature of the recoiling from the absorbed and emitted photons. A good derivation from the point of view of random walks of the atoms and from the Fokker-Planck equation can be found in Sections 5.3 and 5.4 in [Met99].

There are two temperature limits associated with radiation cooling in an optical molasses: Doppler cooling limit, T_D, and recoil limit, T_r. The Doppler limit, as the name suggests, is the lowest possible temperature that can be reached by Doppler cooling, and is defined only by the transition rate: $T_D = \hbar\gamma/2k_B$. For two-level atoms such as the $^1S_0$–$^1P_1$ and $^1S_0$–$^3P_1$ transitions of the even isotopes of Yb, this is the lowest temperature that can be achieved through radiation force. The Doppler limit in Yb is 690 μK for the $^1S_0$–$^1P_1$ transition and 4.5 μK for the $^1S_0$–$^3P_1$ transition. The recoil limit is the limit which comes from the recoil of single photons, corresponding to a temperature of $T_r = \hbar^2 k^2/(Mk_B)$. Any cooling process that relies on spontaneous emission is limited by this recoil.

The temperature in an optical molasses is derived by finding where the rates of heating from the random recoil of photons and cooling from energy dissipation into the light field are equal, that is, $(dE/dt)_{heat} + (dE/dt)_{cool} = 0$ [Let89]. For the simple $J = 0 \rightarrow 1$ transition, the temperature is

$$T = \frac{\hbar\gamma}{8k_B} \frac{\gamma}{|\delta|} \left[1 + \frac{I_t}{I_s} + \left(\frac{2\delta}{\gamma} \right)^2 \right]. \tag{3.19}$$

This has a minimum at $I_t \ll I_s$ and $\delta = \gamma/2$ at $T_D = \hbar\gamma/(2k_B)$. Temperatures expected in a MOT for a two-level atom is the same as in an optical molasses.

There are several ways to measure the temperature of trapped atoms. We use three different methods, and their experiment details will be described in Chapters 7 and 8. The first two methods use time-of-flight (TOF) where the trap is turned off and the rate of expansion is monitored, and the third uses the equipartition theorem. In the first TOF

method, a probe beam is placed at distance d from the trap, and fluorescence of the atoms as a function of time is monitored as they pass through the probe beam (see Section 7.3.3). In the second TOF method, the size of the clouds is compared before and after the trap is turned off.

In the third method, the size of the trapped cloud is used. The equipartition of energy among the degrees of freedom of the system requires that

$$k_B T = M v_{rms}^2 = \kappa \sigma_{rms}^2 \tag{3.20}$$

where M is the mass of the atom, and σ_{rms} is the rms size of the clouds. By measuring the size of the clouds from the absorption images and calculating the spring constant of the trap from Equation 3.18, the temperature of the clouds can be inferred. The details for this method are described in Section 8.8. Some parameters useful for laser cooling and trapping for the two cooling transitions of Yb, $^1S_0$–$^1P_1$ and $^1S_0$–$^3P_1$, are summarized in Table 4.4.

3.4 Sub-Doppler Cooling

In the previous sections, the laser cooling and trapping processes were described entirely in the simplest optical transition possible, $J_g = 0 \rightarrow J_e = 1$. In this system, the cooling is limited by the spontaneous decay rate, and the temperature is limited to T_D. By including higher angular momenta in the ground state, it is possible to achieve colder temperatures. For Yb, this is relevant for the two odd isotopes, ^{171}Yb with $I = 1/2$ or ^{173}Yb with $I = 5/2$, making the ground state hyperfine levels $F = 1/2$ or $F = 5/2$.

In the early days of laser cooling and trapping, sub-Doppler cooling was completely unexpected. It was not until Lett *et al.* reported their observation of temperatures below the Doppler cooling limit in 1988 [Let88] that theories were developed to account for the additional cooling. A series of papers in the November issue of the Journal of the Optical Society of America, B in 1989 explain the various cooling mechanisms that involve optical pumping among the ground state sublevels [Let89, Dal89, Asp89, Cas89, Ung89, Wei89]. Of these, two cooling schemes are relevant to our work in a MOT, and they are described in Ref. [Dal89].

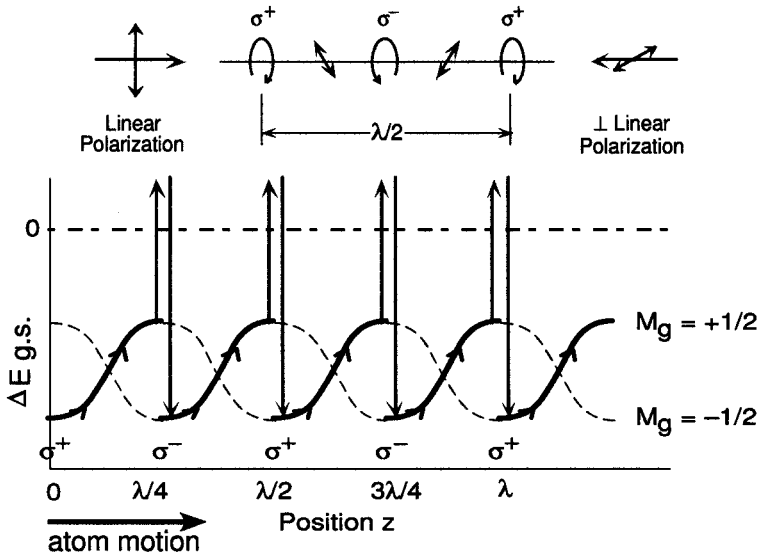

Figure 3.7: Schematic of Sisyphus cooling for $J_g = 1/2 \rightarrow J_e = 3/2$ transition in lin $\perp$ lin configuration. The upper portion shows the polarization set up by the two beams. The lower figure shows the ground state sublevels which are light shifted by the polarization gradient set up.

3.4.1 Sisyphus Cooling: Lin $\perp$ Lin Polarization

The simplest and usually the strongest sub-Doppler cooling mechanism in a MOT is the so-called Sisyphus cooling. It requires at least two sublevels in the ground state and thus requires $J_g \geq 1/2$. Consider an optical molasses in one dimension where the two counter-propagating beams are linearly polarized and orthogonal to each other. The polarization configuration is often referred to as lin $\perp$ lin or $\pi^x\pi^y$ polarization. The resulting polarization is illustrated in the top portion of Figure 3.7. A position dependent polarization gradient is set up, changing from σ^+ to σ^-, and back to σ^+ with a period of $\lambda/2$. The ground state sublevels experience different amounts of light shift depending on the polarization of the light. For the case of $J = 1/2 \rightarrow 3/2$ transition, the $M_g = +1/2$ sublevel is shifted three times the amount that the $M_g = -1/2$ sublevel is shifted when the atoms are at $z = 0$ where the polarization is σ^+ as shown in the bottom portion of Figure 3.7.

As the atom moves to the right, the polarization of light changes and the atoms must climb up a potential hill. At $z = \lambda/4$, the polarization is now σ^-, and the atoms are optically

pumped to the $M_g = -1/2$ sublevel, and the whole process starts all over again. The name Sisyphus cooling comes from the process of the atoms having to go "uphill" over and over again, after a character in Greek mythology, who spends his afterlife pushing a rock uphill as a punishment, only to watch it roll down the hill again. The kinetic energy of the atoms is first converted to potential energy, then shed into the light by the amount equal to the energy difference between the sublevels during optical pumping. The most efficient cooling occurs when the atoms have enough momentum to travel a distance of $\lambda/4$ as they undergo one optical pumping cycle. The friction coefficient is a factor of $2|\delta|/\gamma$ larger than that of Doppler cooling, and the predicted temperature is smaller by the same amount [Dal89].

3.4.2 Corkscrew Cooling: σ^+-σ^- Polarization

When the polarization of the two counterpropagating beams are circularly polarized and orthogonal to each other, the resulting polarization is linear everywhere, and rotating in a corkscrew-like manner as shown in the top part of Figure 3.8. This polarization arrangement does not induce a light shift that varies with position as it does in Sisyphus cooling. Instead, velocity dependent forces arise from motion-induced atomic orientation. This cooling mechanism requires a minimum of $J_g = 1$.

Consider an atom with $J = 1 \rightarrow 2$ transition at rest, immersed in linearly polarized light. Because of the difference in Clebsch-Gordan coefficients as shown in Figure 3.8, more atoms are optically pumped into the $M_g = 0$ sublevel and the $M_g = 0$ ground state sublevel is shifted more than the $M_g = \pm 1$ sublevels due to the difference in transition probabilities. If the atoms are moving in this light field with speed v, the optical pumping process lags behind the change in the laser polarization. The slight population imbalance resulting from this lag translates into the difference in the scattering rate of counter- or co-propagating σ^+ and σ^- light. The energy is dissipated into the light field. The resulting equilibrium temperature is of the same order as in Sisyphus cooling, however, the cooling rate is slower by a factor of δ^2/γ^2, and in cases where both cooling is present, Sisyphus cooling will dominate. See Ref. [Dal89] for more details.

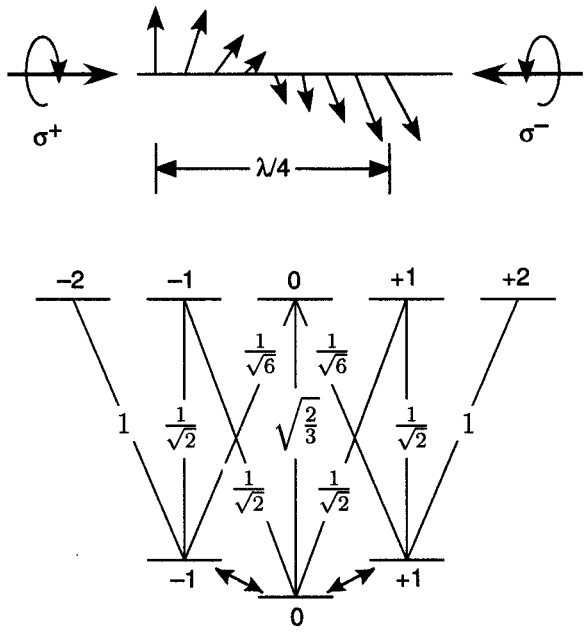

Figure 3.8: Corkscrew Cooling: $J_g = 1 \rightarrow J_e = 2$ transition in $\sigma^+ - \sigma^-$ configuration. The top half shows the polarization that results from such a configuration, where it is linear everywhere but rotating in a corkscrew-like manner with a period of λ. The lower half shows the Clebsch-Gordan coefficients for a $J = 1 \rightarrow 2$ transition. The $M_g = 0$ sublevel is shifted more than the $M_g = \pm 1$ sublevels in atoms immersed in linearly polarized light due to the difference in transition probabilities.

3.4.3 Sub-Doppler Cooling in Three Dimensions

In general, the phase relations among the three pairs of mutually orthogonal counterpropagating beams are not well defined. The polarization variations that moving atoms see as they go through a three-dimensional (3D) optical molasses or MOT depend on the phase relations among the beams, and are neither strictly lin $\perp$ lin nor $\sigma^+ - \sigma^-$. The degrees of Sisyphus and corkscrew cooling available at all phases among the three beams in 3D with the counterpropagating beams having $\pi^x\pi^x$, $\pi^x\pi^y$ (lin $\perp$ lin), $\sigma^+ - \sigma^-$, and $\sigma^+ - \sigma^+$ have been characterized in Ref. [Hop97]. Most published work on 3D cooling is studied in the $\pi^x\pi^y$ configuration. The maximum degree of Sisyphus cooling available in this polarization configuration is relatively insensitive to the phase among the three beams, varying between

45–50% of cooling available in 1D. In the $\sigma^+-\sigma^-$ MOT configuration, the degree of Sisyphus cooling averaged over all phase relations is 44%, similar to the 47% in the averaged 3D $\pi^x\pi^y$ configuration. However, the degree of Sisyphus cooling can vary from 0 when all beams are in phase, to 53% in the $\sigma^+-\sigma^-$ MOT configuration when the three phases are orthogonal to each other [Hop97]. It will be interesting to see if changing these phase relations will change the temperature of the MOT, especially in ^{171}Yb which lacks enough angular momentum for corkscrew cooling.

From the one-dimensional description of Sisyphus and corkscrew cooling mechanisms, the kinetic energy of the atomic motion that results from fluctuating radiative forces leads to the scaling law for $|\delta| \gg \gamma$,

$$E_k \propto \hbar|\delta|s \tag{3.21}$$

where s is the saturation parameter $s = 2|\Omega|^2/(4\delta^2 + \gamma^2)$ and Ω is the Rabi frequency. Experiments [Sal90, Ger93] and numerical simulations [Cas95, Møl91] have shown that E_k of atom samples cooled in 3D also vary linearly with $|\delta|s$.

The temperature of laser-cooled ^{133}Cs ($F = 4 \rightarrow 5$) [Sal90], ^{85}Rb ($F = 3 \rightarrow 4$), and ^{87}Rb ($F = 2 \rightarrow 3$) [Ger93] was measured as a function of laser intensity and detuning in a lin $\perp$ lin configuration. The Rb experiment showed that given the same experimental conditions, the dependence of temperature on laser intensity and detuning is different for transitions with different F. The results are consistent with the model that includes localization of atoms in the standing waves set up by the lasers forming the optical molasses.

Castin and Mølmer calculated the mean kinetic energy of atoms cooled in lin $\perp$ lin molasses with well defined phase relations [Cas95]. Their calculations are consistent with the experimental result of Cs and Rb. They also showed that the dependence of mean kinetic energy on the laser detuning and laser intensity, $|\delta|s$, depends only weakly on the phase relations among the three perpendicular beams. Figure 3.9 shows their calculations as shown in Fig. 1 in Ref. [Cas95]. It shows that at high enough laser intensities, E_k depends linearly on $|\delta|s$, and that the slopes are different for transitions with different J_g. Localization effects which occurs from both intensity gradients and polarization gradients play a significant role in the final equilibrium temperature. It was found experimentally that in MOT or molasses,

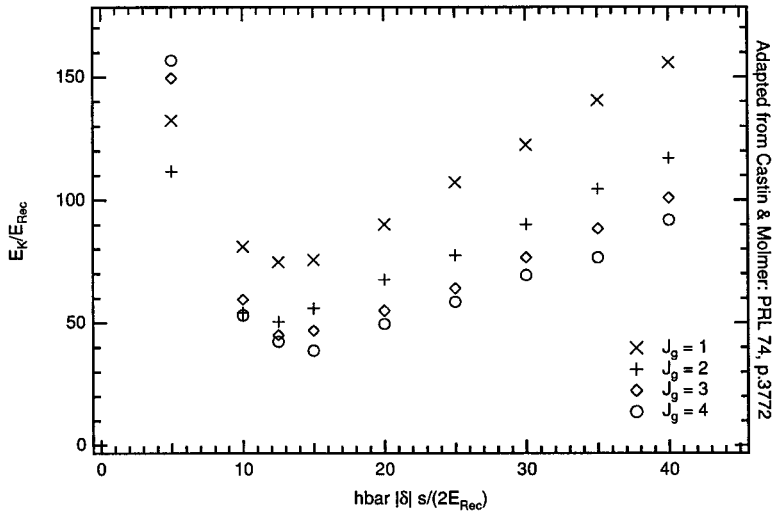

Figure 3.9: Mean kinetic energy of atoms cooled in a 3D lin $\perp$ lin configuration for $J_g \rightarrow J_e = J_g + 1$, $J_g = 1$, 2, 3, and 4 for $\delta = -5\gamma$. Adapted from Ref. [Cas95].

atoms tend to be localized to small volumes within the clouds, and that the relative phase variation among the beams has little effect on localization, not only for 3D $\pi^x\pi^y$ but for 3D $\sigma^+-\sigma^-$ configuration as well [Sch99]. It was also found experimentally that the temperature in a MOT is 30% higher than observed in a lin $\perp$ lin cooling [Wal94].

We have made these measurements for Yb, and the results are presented in Chapter 8. With seven stable isotopes with the even isotopes having $I = 0$, ^{171}Yb with $I = 1/2$, and ^{173}Yb with $I = 5/2$, Yb is an ideal system for conducting a comparative study on the cooling mechanisms. ^{171}Yb is especially interesting since corkscrew cooling is absent for transitions with $F_g = 1/2$: cooling in atoms with spin of only 1/2 has not yet been studied experimentally. In 1D, it is expected that the temperature is a factor of $116/63 = 1.84$ higher than expected from the simple Doppler cooling resulting from the increase in momentum diffusion due to a correlation between the successive photon absorptions via the ground state sublevels [Cas90, Møl02]. We have found that in a MOT with $\sigma^+-\sigma^-$ configuration, the linear dependence of temperature on laser intensity and detuning for the odd isotopes is consistent with this view. See Chapter 8 for details.

Chapter 4

YTTERBIUM

Ytterbium (Yb) is a diamagnetic atom with properties that are significantly different from alkali-metals. It first came to our attention as an atom that has an electronic structure very similar to mercury and a possible candidate for a new EDM experiment using neutral atom traps. It is a heavy diamagnetic atom with $Z = 70$ and a $^1S_0$ ground state that has an isotope with nuclear spin of $I = 1/2$, ^{171}Yb. The abundance of stable isotopes (seven to be exact) makes it a very versatile atom. In addition to an EDM measurement, many experiments have been proposed for Yb including atomic frequency standards, an all-optical quantum degenerate gas of bosons, fermions, and mixture of both, as well as parity nonconservation measurements on the $6s^2\ ^1S_0 \rightarrow 6s5d\ ^3D_1$ transition, which is underway at the University of California at Berkeley [DeM95, Bow96, Bow99].

There are two transitions available for cooling and trapping in ytterbium, the strong blue $^1S_0$–$^1P_1$ transition at 399 nm and the weaker and narrow green intercombination transition, $^1S_0$–$^3P_1$, at 556 nm. We have trapped all seven isotopes of Yb using both of these lines, and the details are described in Chapters 7 and 8. The availability of five even isotopes and two odd isotopes with different nuclear spins have allowed us to investigate trap properties that have not been studied before, as discussed in Chapter 8. In this chapter, basic properties of Yb are discussed. The characteristic values of Yb which are important for laser cooling and trapping are also discussed.

4.1 Basic Properties

Ytterbium is a rare earth metal. For its location on the periodic table, see Figure 4.1. The ground state electronic configuration is [Xe] $4f^{14}6s^2$, and it has two electrons in the valence shell which close the valence s-shell. Ytterbium metal is silvery in color, and quite malleable: we were able to shave off pieces by a pair of wire cutters in order to load our Yb oven (see

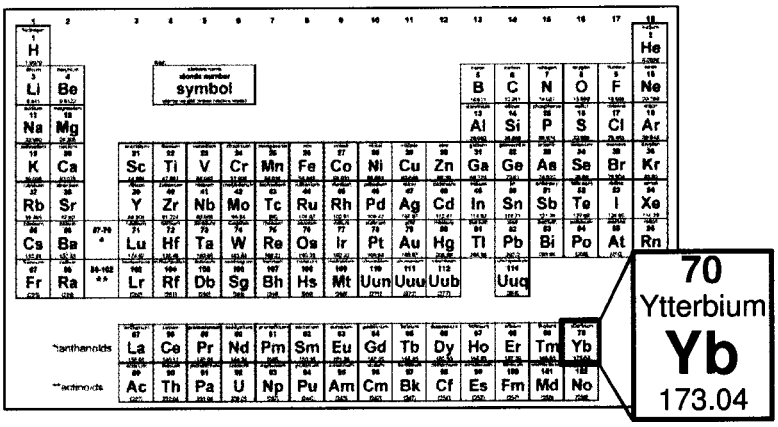

Figure 4.1: Yb in the periodic table of elements.

Section 5.1.2 for a description of the oven design). We purchased the metal as ingots from Aldrich Chemical Co. Yb has a melting point of 819 °C and boiling point of 1196 °C, and is fairly stable in air, but will slowly react with moisture in the air and vendors suggest storing it in a sealed container. No special precautions were necessary when transferring the ingots into the Yb oven aside from wearing a pair of latex gloves and using a pair of tweezers. Yb has a significant vapor pressure at temperatures much below the melting point, of 0.7 mTorr at our operating temperatures at 400 °C (see Figure 4.2). This allows for a much simpler oven design since we do not have to worry about containing the liquid form of Yb.

It is reactive when heated. A "vacuum"quartz cell pumped out with an oil-diffusion pump with a few grams of ytterbium inside was made at the University of Washington. As ytterbium has a significant vapor pressure well within the operating temperature of quartz, we expected to be able detect the absorption signal without liquefying Yb. We heated the cell to about 500 °C, still well below the melting point of Yb and well within the operating range of quartz, and tried to observe an absorption spectrum on the $^1S_0$–$^3P_1$ transition (we did not yet have a laser source at 400 nm). We took all the usual precautions such as differentially heating the cell to prevent the atoms from accumulating on the windows and blocking optical access. We never saw absorption with this cell. When we pulled the cell out from the oven, we noticed that the ytterbium had eaten away at the quartz tube

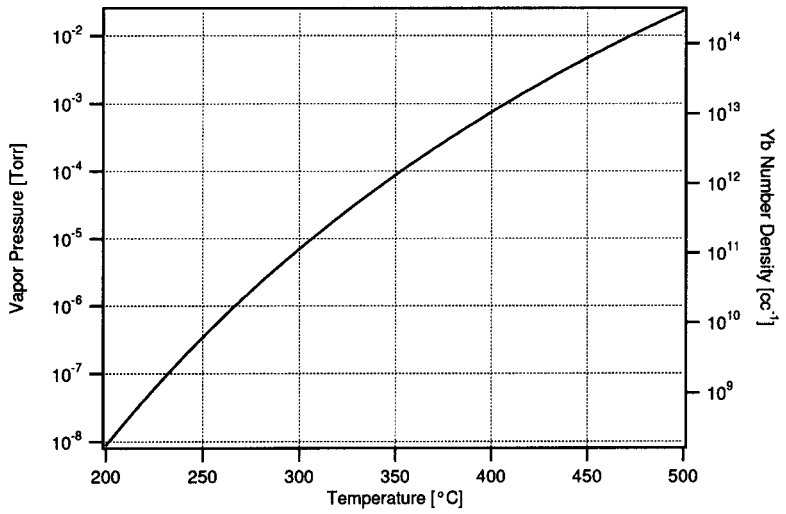

Figure 4.2: Vapor pressure in Torr of ytterbium as a function of temperature calculated from the values found in CRC Handbook [Lid02].

(see Figure 4.3). The walls appeared opaque white near the middle of the tube, and it was metallic black near the windows. After gently handling the cell for a few minutes, the tube fell apart into two pieces.

After this experience, we designed the Yb oven to carefully avoid all ceramic and glass. The current oven is built entirely from stainless steel, copper, and aluminum (see Section 5.1.2 for the oven design), with a vacuum of better than 10^{-7} Torr when the oven is on. The enclosure for the volume that contains Yb is made of stainless steel. The low pressure ensures that there is no residual gas that can react with Yb and that the mean free path of the atoms is long enough to form an atomic beam.

4.2 Isotopes and Hyperfine Levels

Yb has seven stable isotopes, most with natural abundance exceeding 10% as summarized in Table 4.1: five even isotopes with $I = 0$ (^{168,170,172,174,176}Yb) and two odd isotopes, ^{171}Yb, with $I = 1/2$ and ^{173}Yb with $I = 5/2$. The even isotopes are bosons, and the odd isotopes are fermions. Having many isotopes makes Yb a natural choice for conducting isotopic

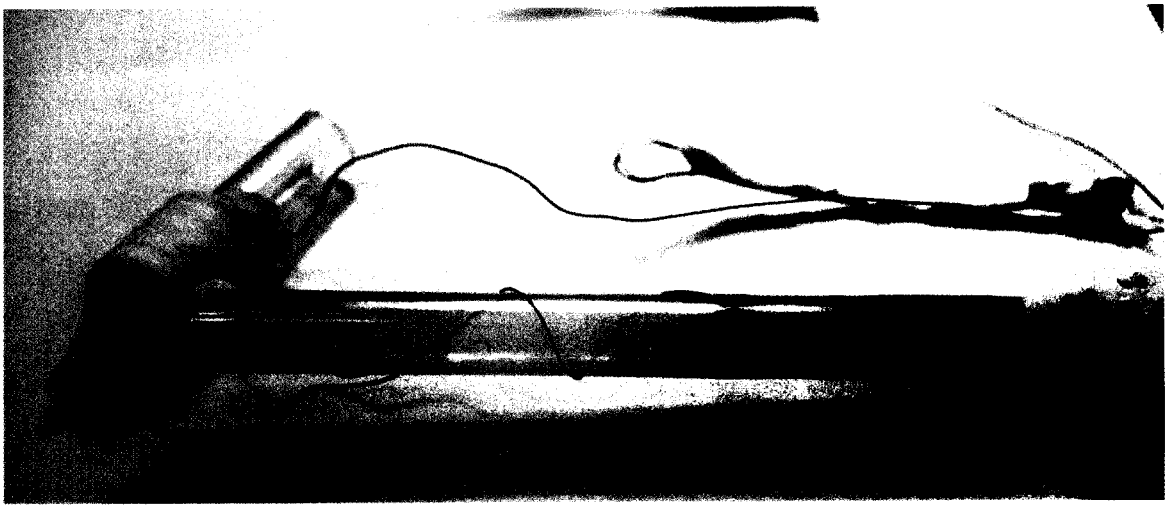

Figure 4.3: Yb in a quartz cell. The tube was sectioned off into three segments with Yb in the middle segment to try to prevent the windows from having the lowest temperature, to prevent them from being coated with Yb. The white mass seen near the ends of the tube encase some heating wires for extra heating. The cell was heated by these wires and clam-shell heaters around the entire tube.

comparisons.

The lower energy levels of ytterbium are shown in Figure 4.4. There are two transitions available for laser cooling and trapping: the strong $6s^2\ {}^1S_0 \rightarrow 6s6p\ {}^1P_1$ transition at 399 nm and the weaker green intercombination transition, $6s^2\ {}^1S_0 \rightarrow 6s6p\ {}^3P_1$, at 556 nm. We have trapped all seven isotopes of Yb using both transitions, and the lasers used for these transitions are discussed in Chapter 6. These transitions are remarkably similar to the alkaline earth (group II) elements such as strontium and calcium (see Section 2.1).

The blue transition is an allowed transition, and this is reflected in the short lifetime of the ${}^1P_1$ state of 5.5 ns, with a relatively broad width of 28 MHz. The green transition is an intercombination transition ($\Delta S = 1$), and has a long lifetime of 850 ns (187 kHz). Both of these states approximate a simple two-level optical transition, however the blue transition is not completely closed. Atoms in the ${}^1P_1$ state have some probability of decaying into either one of the ${}^3D_2$ or ${}^3D_1$ states with a branching ratio that has a lower limit of 1.2×10^{-7} [Hon99]. The atoms can then decay into one of the ${}^3P_2$, ${}^3P_1$, or ${}^3P_0$ states, of

Table 4.1: Natural abundance and nuclear spin of Yb [Lid02].

Isotope	Natural Abundance	Nuclear spin
^{168}Yb	0.0013	0
^{170}Yb	0.0305	0
^{171}Yb	0.143	1/2
^{172}Yb	0.219	0
^{173}Yb	0.161	5/2
^{174}Yb	0.318	0
^{176}Yb	0.127	0

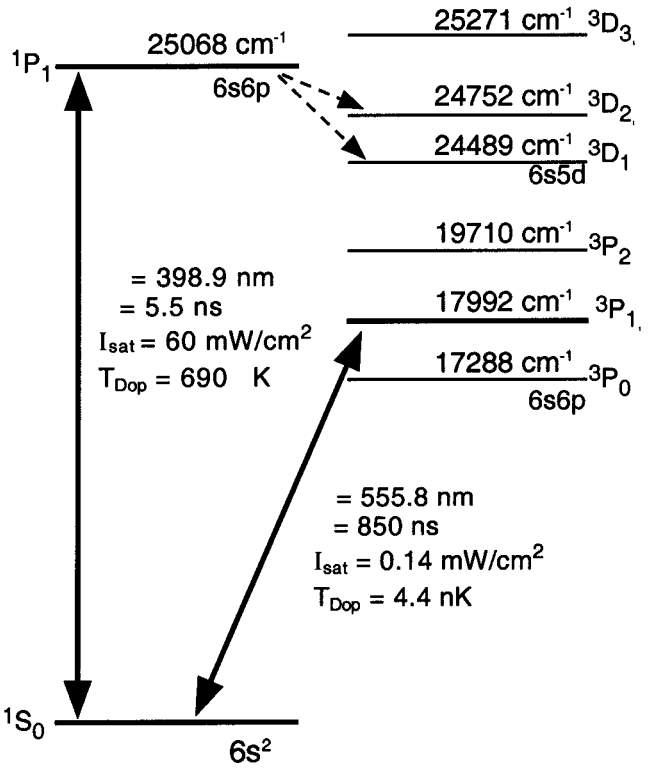

Figure 4.4: Lower energy levels of Yb [Mar78].

which $^3P_2$ and $^3P_0$ are metastable. The lifetimes of these states are extremely long (12 s for $^3P_2$, the lifetime for $^3P_0$ could not be found in the literature). This poses limitations on the lifetime and the number of trapped atoms in our blue MOT. The longest lifetime we have achieved in the blue trap is 800 ms, and we have trapped as many as 5×10^6 atoms.

The green transition is completely closed and has no such limitations. However, the slow transition rate of the $^3P_1$ state limits the maximum force one can apply on the atoms using this transition to roughly 150 times less than that of the blue transition. A Zeeman slower using this transition would be completely impractical as the minimum length required to slow an atomic beam coming out from an oven at 400 °C would be 27 m. Our Zeeman slower and initial cooling and trapping uses the blue transition, and the atoms are loaded into the green MOT once they are sufficiently cool.

Table 4.2 and Figure 4.5 show the relative strengths and the isotope shifts and hyperfine splittings for the blue ($^1S_0$–$^1P_1$) transition. Table 4.3 and Figure 4.6 show the same for the green ($^1S_0$–$^3P_1$) transition. Note that the $^1S_0$–$^3P_1$ transition is much narrower. The strengths of the even isotopes directly reflect their natural abundance. Since both ground-state electron and nuclear angular momentum are zero ($J = I = 0$), all transitions are $F_g = 0 \rightarrow F_e = 1$ in the even isotopes. The strengths of the odd isotopes include the relative strengths of the hyperfine components. For ^{171}Yb which has a nuclear spin of $I = 1/2$, the two possible transitions are $F_g = 1/2 \rightarrow F_e = 1/2$ and $F_e = 3/2$. For the ^{173}Yb isotope which has $I = 5/2$, there are three possible transitions, $F_g = 5/2 \rightarrow F_e = 3/2$, $F_e = 5/2$, and $F_e = 7/2$. The MOTs work only on the transitions with the highest F_e, that is, $F = 1/2 \rightarrow 3/2$ for the ^{171}Yb isotope and $F = 5/2 \rightarrow 7/2$ for the ^{173}Yb isotope. Most of the developmental work was done using the ^{174}Yb isotope because of it has the highest abundance and forms the largest trap in terms of the number of atoms trapped.

Table 4.2: Yb isotope, hyperfine levels, relative strength, isotope shifts and hyperfine splittings of the $^1S_0$–$^1P_1$ transition at 399 nm [Dei93].

Isotope/h.f.	Relative Strengths	Shift (MHz)
176	0.1273	0
173 (5/2 - 5/2)	0.0498	272.1
174	0.3184	509.4
173 (5/2 - 3/2)	0.0225	1008.86
172	0.2182	1039.3
173 (5/2 - 7/2)	0.0884	1092.8
171 (1/2 - 3/2)	0.1140	1352.7
171 (1/2 - 1/2)	0.0285	1654.5
170	0.0303	1690.8
168	0.00135	2388.5

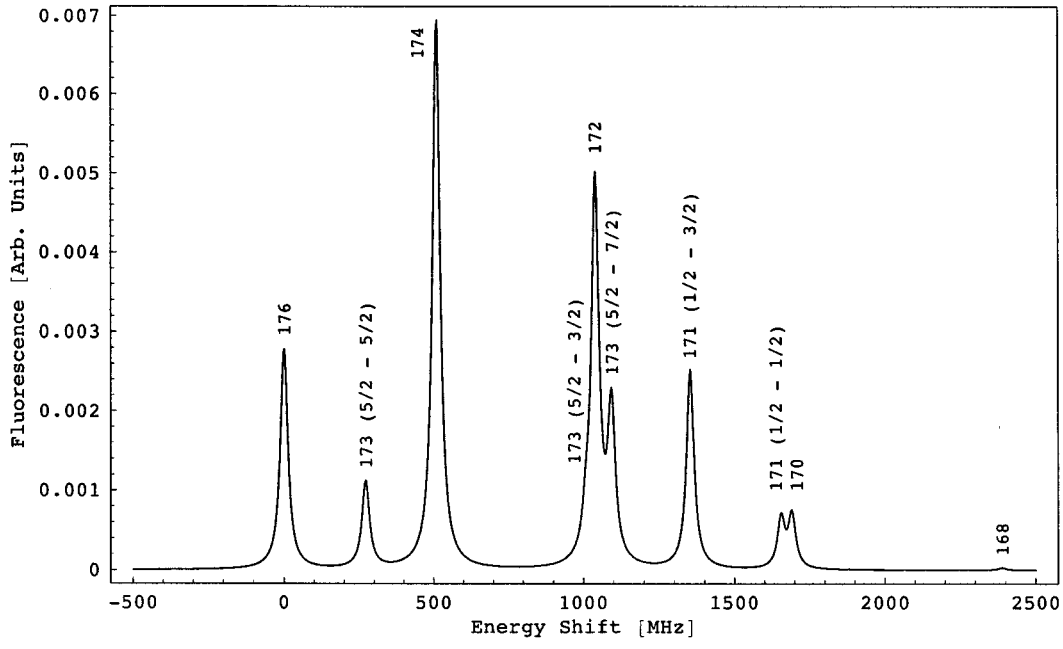

Figure 4.5: Spectrum of the $^1S_0$–$^1P_1$ transition at 399 nm.

Table 4.3: Yb isotope, hyperfine levels, relative strengths, isotope shifts and hyperfine splittings of the $^1S_0$–$^3P_1$ transition at 556 nm [vW94].

Isotope/h.f.	Relative Strength	Shift (MHz)
173 (5/2 - 7/2)	0.0715	0
171 (1/2 - 1/2)	0.0476	255
176	0.1274	1432
174	0.3187	2386
172	0.2184	3387
170	0.0303	4673
173 (5/2 - 5/2)	0.0537	4698
168	0.0014	6044
171 (1/2 - 3/2)	0.0952	6192
173 (5/2 - 3/2)	0.0358	6193

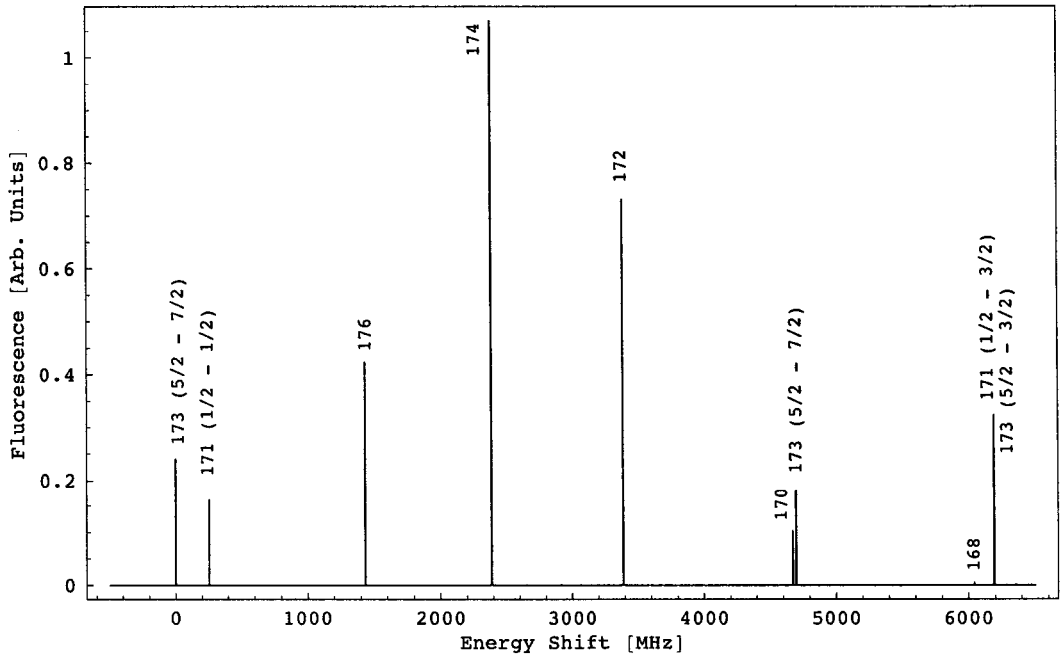

Figure 4.6: Spectrum of the $^1S_0$–$^3P_1$ transition at 556 nm.

4.3 *Properties for Trapping*

Table 4.4 lists some quantities mentioned in Chapter 3 that are useful for cooling and trapping using the two transitions of Yb: $^1S_0$–$^1P_1$ and $^1S_0$–$^3P_1$. The quantities related to Doppler cooling rely on the transition rate, and are in general, roughly 150 times weaker for the green transition. The recoil parameters depend only on the photon energy and are comparable in the two transitions.

Table 4.4: Definitions and values of parameters relevant for cooling and trapping of Yb.

Parameters	$^1S_0$–$^1P_1$	$^1S_0$–$^3P_1$	Units	Description
λ	398.911	555.798	(nm)	Transition wavelength
g_J	1.035	1.493		Landé g-factor
$k = 2\pi/\lambda$	157508	113048	(cm^{-1})	Wavenumber
$\hbar\omega_a$	3.11	2.23	(eV)	Transition energy
τ	5.5	850	(ns)	Lifetime of excited state
$\gamma/2\pi = 1/2\pi\tau$	28.9	0.187	(MHz)	Spontaneous decay frequency
$\sigma_{ge} = 3\lambda^2/2\pi$	76	147	(10^{-15} m^2)	Absorption cross section
$I_s = \pi hc/3\lambda^3\tau$	60	0.14	(mW/cm^2)	Saturation intensity
$a_{max} = \hbar k/2M\tau$	52	0.24	(10^6 m/s^2)	Maximum possible acceleration
$\omega_r/2\pi = \hbar k^2/4\pi M$	7.2	3.7	(kHz)	Recoil frequency
$\varepsilon = \omega_r/\gamma$	0.25	19.7	(10^{-3})	Recoil frequency/natural width
$v_c = \gamma/k$	1154	10.4	(cm/s)	Capture velocity
$T_c = M\gamma^2/k^2k_B$	2800	0.23	(mK)	Capture limit temperature
$v_D = \sqrt{k_BT_D/M}$	18.1	1.46	(cm/s)	Doppler limit velocity
$T_D = \hbar\gamma/2k_B$	694	4.5	(μK)	Doppler limit temperature
$v_r = \hbar k/M$	0.57	0.41	(cm/s)	Recoil velocity
$T_r = \hbar^2k^2/Mk_B$	0.69	0.35	(μK)	Recoil temperature

Chapter 5

THE APPARATUS

This chapter describes the apparatus that was developed for this experiment, including the vacuum chamber that houses the oven and the atomic beam, Zeeman slower, and the design of the magneto-optical trap. A detailed description of the lasers used in this experiment is given in Chapter 6.

5.1 Vacuum Chamber

There were a few versions of the vacuum system prior to the current one, including a simple ytterbium cell mentioned in Section 4.1 and an all-glass MOT chamber. To achieve the 100 s trap lifetime that is necessary to conduct the proposed EDM experiment, it is essential to have a very good vacuum of better than 10^{-11} Torr. The current vacuum system was designed to meet this demand. We have employed a differential pumping scheme which allows us to have different pressures in the Yb oven region and the MOT region. The pressure in the MOT region is roughly 5×10^{-10} Torr when the Yb oven on the other side is on, and less than 10^{-11} Torr when the oven is off, and we were able to observe lifetimes of up to 75 s in the green MOT, limited by the stability of the green laser. We were especially encouraged to see the 300 s trap lifetime obtained by the Thomas group at Duke [O'H99] with a background pressure of 10^{-11} Torr using an ultra-stable CO_2 far-off resonance trap (FORT). A good starting point for learning about vacuum systems in general is a book by Chambers, Fitch and Halliday [Cha99].

5.1.1 Vacuum Chamber Design

The vacuum chamber was designed for high trap loading efficiency and long trap lifetimes. It is important to have the MOT region as close to the end of the Zeeman slower as possible

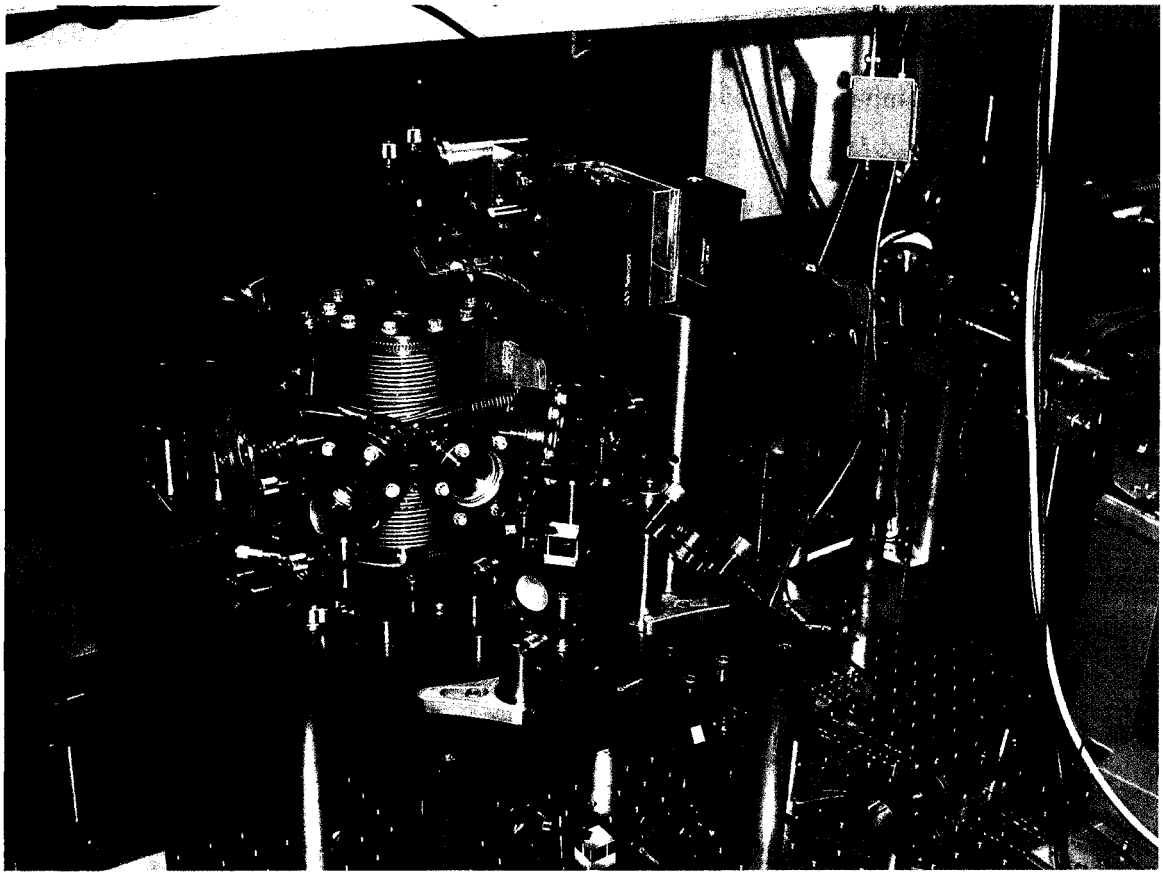

Figure 5.1: Photograph of the MOT chamber and surrounding optics.

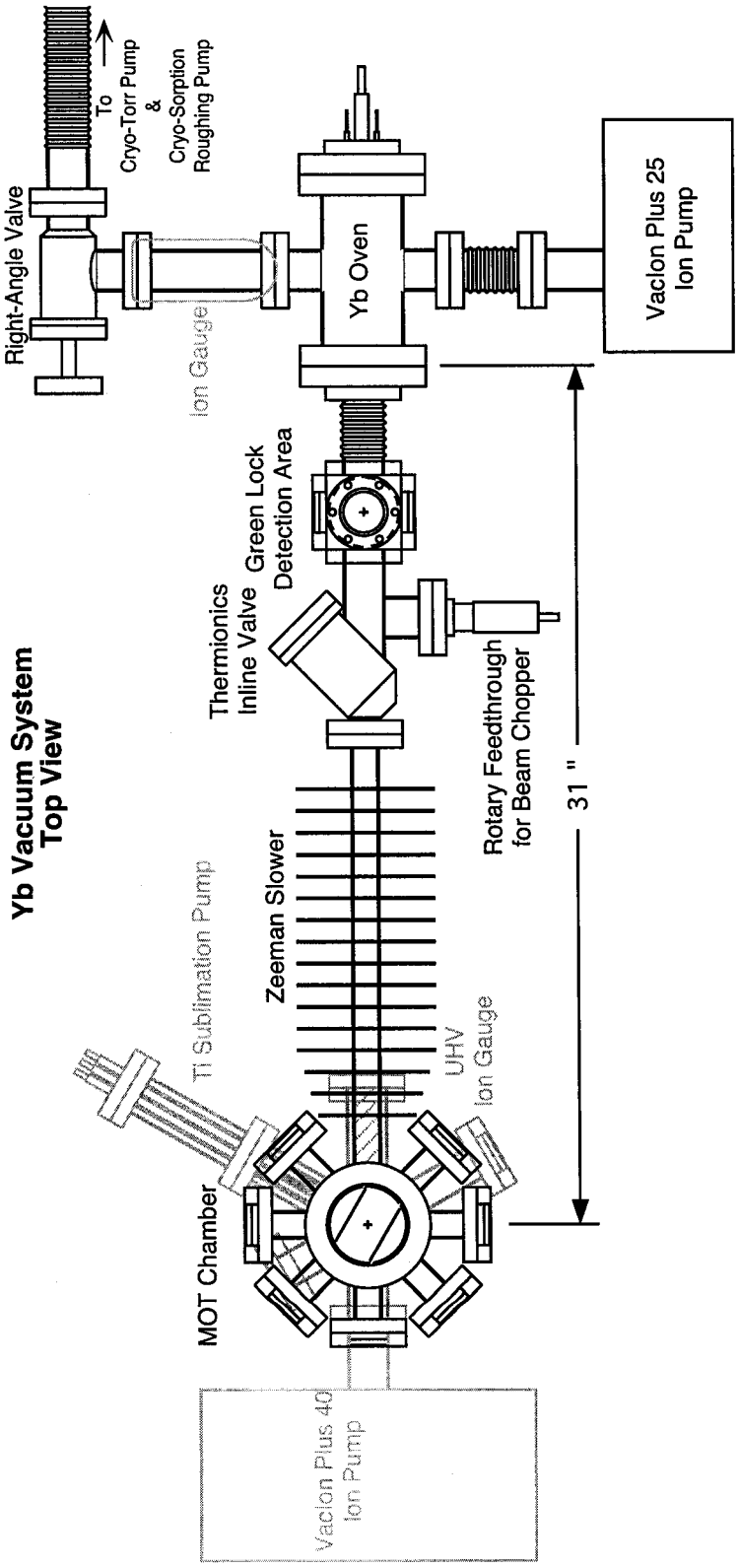

Figure 5.2: The top view of the vacuum chamber. The upper layer is in black and the lower layer is in gray. A side view of the same apparatus is shown in Figure 5.3.

and to have the pressure in the ultra-high vacuum region, below 10^{-10} Torr. Figures 5.2 and 5.3 show schematics of the vacuum chamber. The overall length from the back of the oven to the end of the MOT Chamber is 44". Most joints are 2-3/4" ConFlat flanges, with the exception of the top and bottom of the MOT chamber and Yb oven ends which are 4-5/8" Conflat flanges. The MOT Chamber was custom ordered from Kurt J. Lesker Co. to minimize the distance between the Zeeman slower to the MOT region, while having enough optical access for trapping and imaging (see Figure 5.4). The Thermionics straight-through valve allows us to reload more Yb into the oven without having to open up the clean MOT side to atmosphere. We have not had to do this yet in the three years of operation. The atomic beam can be chopped on and off by using the rotary feedthrough which has an aluminum shaft attached on the inside. The shaft has two holes perpendicular each other and to the axis of the feedthrough, and the atomic beam is chopped at four times the rate of the rotation of the feedthrough. We have added the Green Lock Detection Area for additional optical access to the atomic beam. A portion of the laser is used to excite the atoms and the fluorescence is detected with a PMT to lock the green laser to an atomic transition (more about this in Section 6.2.3). The bellows between the Green Lock Detection Area and the Yb oven allow us to move the oven to accurately position the atomic beam. The system is isolated from the roughing pumps with a right-angle valve. We employ differential pumping to achieve the low pressure in the MOT region. The atomic beam collimator located at the junction between the oven and the bellows maintains the pressure differential of 10^{-8} Torr on the oven side, and $< 10^{-11}$ Torr in the MOT region when the oven is off, and 10^{-6} Torr and 5×10^{-10} Torr with the oven running at 400 °C.

There are two ion pumps constantly pumping on the system, one on each side of the collimator. The one on the MOT side is a VacIon Plus 40 (StarCell), and the oven side has a VacIon Plus 25 (Noble Diode), both from Varian Vacuum Technologies. There are two Titanium Sublimation Pumps (TSP), on each side of the differential pumping to help pump the gettable gases such as hydrogen and nitrogen. The TSPs are turned on for 1–2 min at a time by running a 48 Amps of current when we wanted the pressure to be as low as possible, such as when measuring the lifetime of the traps. TSPs deposit a thin layer of titanium on surfaces inside the vacuum chamber which then acts as a getter. To avoid the bottom

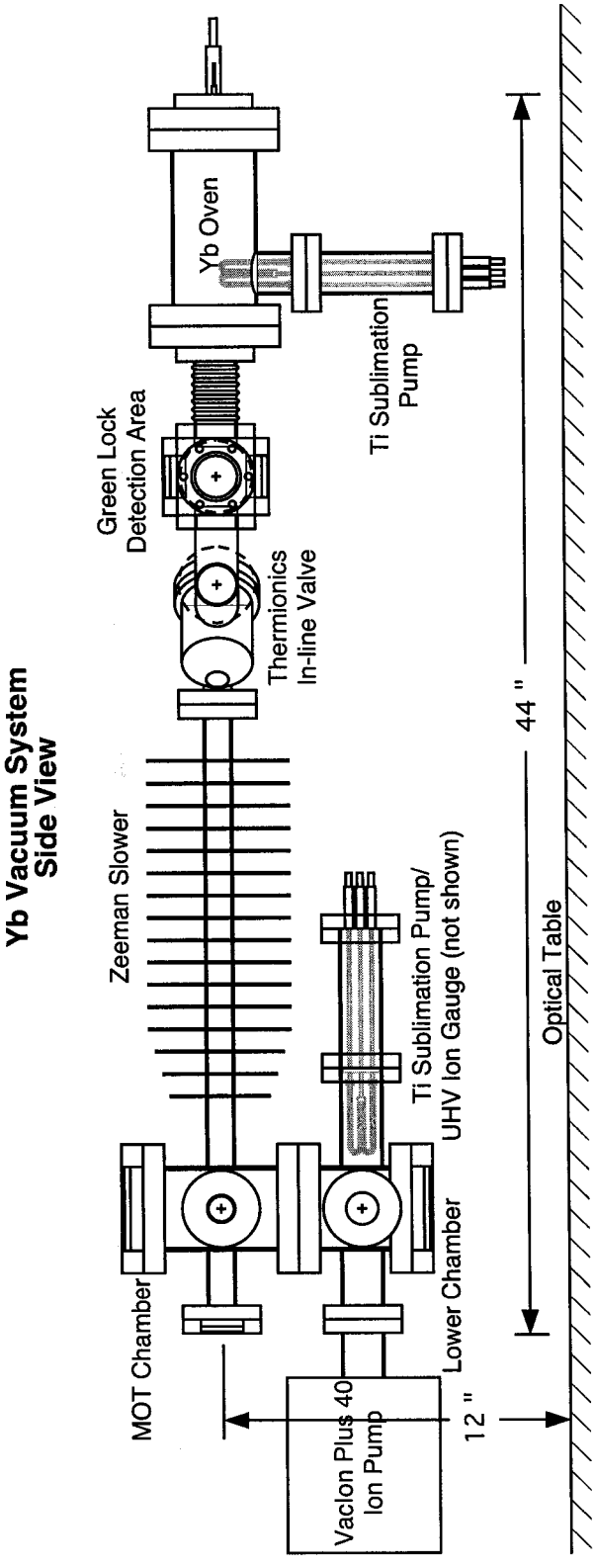

Figure 5.3: The side view of the vacuum chamber. The angles of the ports of the lower chamber are shown rotated and the ion pump on the oven side is omitted for clarity.

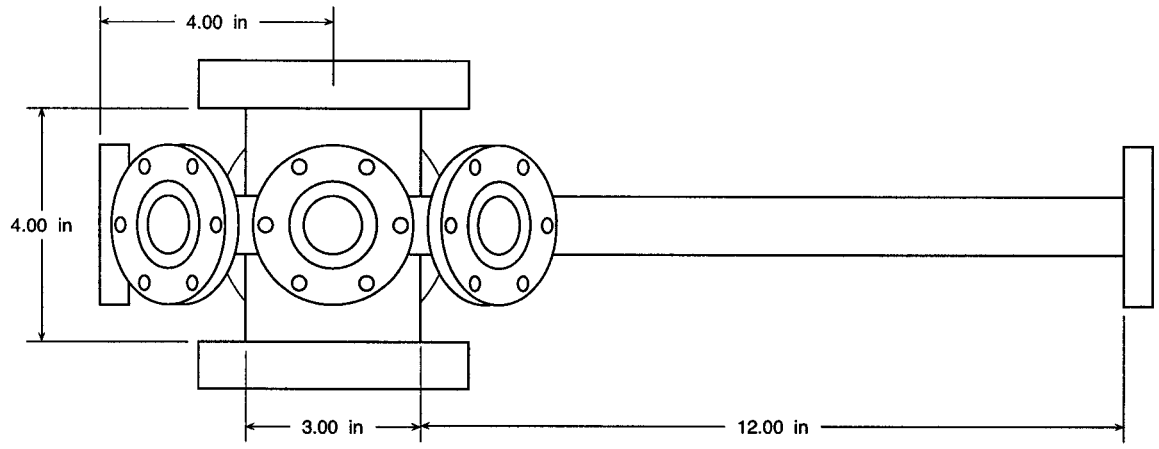

Figure 5.4: The Zeeman slower and MOT regions of the vacuum chamber. The tubes are 1" diameter, the top and bottom flange are 4-5/8" tapped non-rotatable ConFlat flanges, the rest are 2-3/4" ConFlat, rotatable along the Zeeman slower, the rest are non-rotatable.

window from getting coated, the direct line-of-sight between the bottom window and TSP was blocked by a piece of aluminum bent in ∪ shape placed on the bottom window to act as a baffle while allowing optical access, represented by the two lines in the middle of the MOT Chamber in Figure 5.2. Water cooling was installed using 1/8" copper refrigerator tubing around the tubes that house the UHV gauges and TSPs to keep the vacuum chamber cool when those components are being used.

The pressure on both sides is measured by ion gauges. On the oven side, there is a standard Bayard-Alpert type ionization gauge with 2 tungsten filaments which can measure pressure down to 1×10^{-9} Torr. On the MOT side, there is a UHV-24p Nude Bayard-Alpert type ionization gauge from Varian (dual thoria-coated iridium filament) which can measure pressure down to 5×10^{-12} Torr.

The seven 1-1/2" viewports on the MOT chamber and the two 3" viewports on top and bottom of the MOT region are from Larson Electronic Glass, anti-reflection coated to 550 nm. The two on the lower chamber and the four on the Spherical Cube for the Green-Lock-Detection Area are uncoated 7056 Glass.

5.1.2 Oven Design

The Yb oven was designed to avoid all ceramic materials because Yb can degrade these materials, as described in Section 4.1. The oven is located inside a stainless steel four-way cross, with two 4-5/8" and two 2-3/4" ConFlat ports, as shown in Figure 5.5. The oven consists of a 3/8" OD stainless steel (ss) tube with 0.01" wall thickness, closed, and folded over at the back end like a tube of toothpaste. Two ss plugs are inserted, and the front one acts as one of the collimators with a 0.07" hole which goes all the way through, and 0.2" hole drilled most of the way to prevent clogging. The back plug helps contain the Yb in a small volume. A hole at the very back where the tube is folded over ensures that this region is pumped out.

The oven is heated by running a current through the ss tube. An electrical feed through at the back of the oven provides two current/voltage feedthrough (1/4" copper rods, can support up to 5 kV) and two type-K thermocouple temperature gauges. The ss tube is connected to and supported by the 1/4" copper rods by custom-made copper clamps. Roughly 5 g of Yb ingot is placed between the two ss plugs, and the oven is typically heated to 400 °C by running 70 A AC through the tube (about 550 mV across the two feedthroughs). The current is supplied by stacking two Variacs in series to get fine-tuning sensitivity, then a 250 A transformer is attached to boost up the current. Typical settings on the Variacs are 25 and 50/130.

During operation we observed a a peculiar behavior in this oven. The current going in and coming out through the leads were the same, but the voltage drop across them seemed to be changing randomly at a rate of about 1 Hz. We found that setting the Variac at the same dial setting did not always heat the oven to the same temperature. To assure constant operating oven temperature, we closely monitored the temperature and adjusted the Variacs accordingly. It was not too much of a problem since most of the time we could leave the Variacs in the same setting for months at a time. We have also considered using different materials for the body of the oven to reduce the amount of current necessary to heat it. Though no extensive testing was done, Hastelloy alloys were considered as one of the candidates as being chemically non-corrosive and having high electrical resistivity.

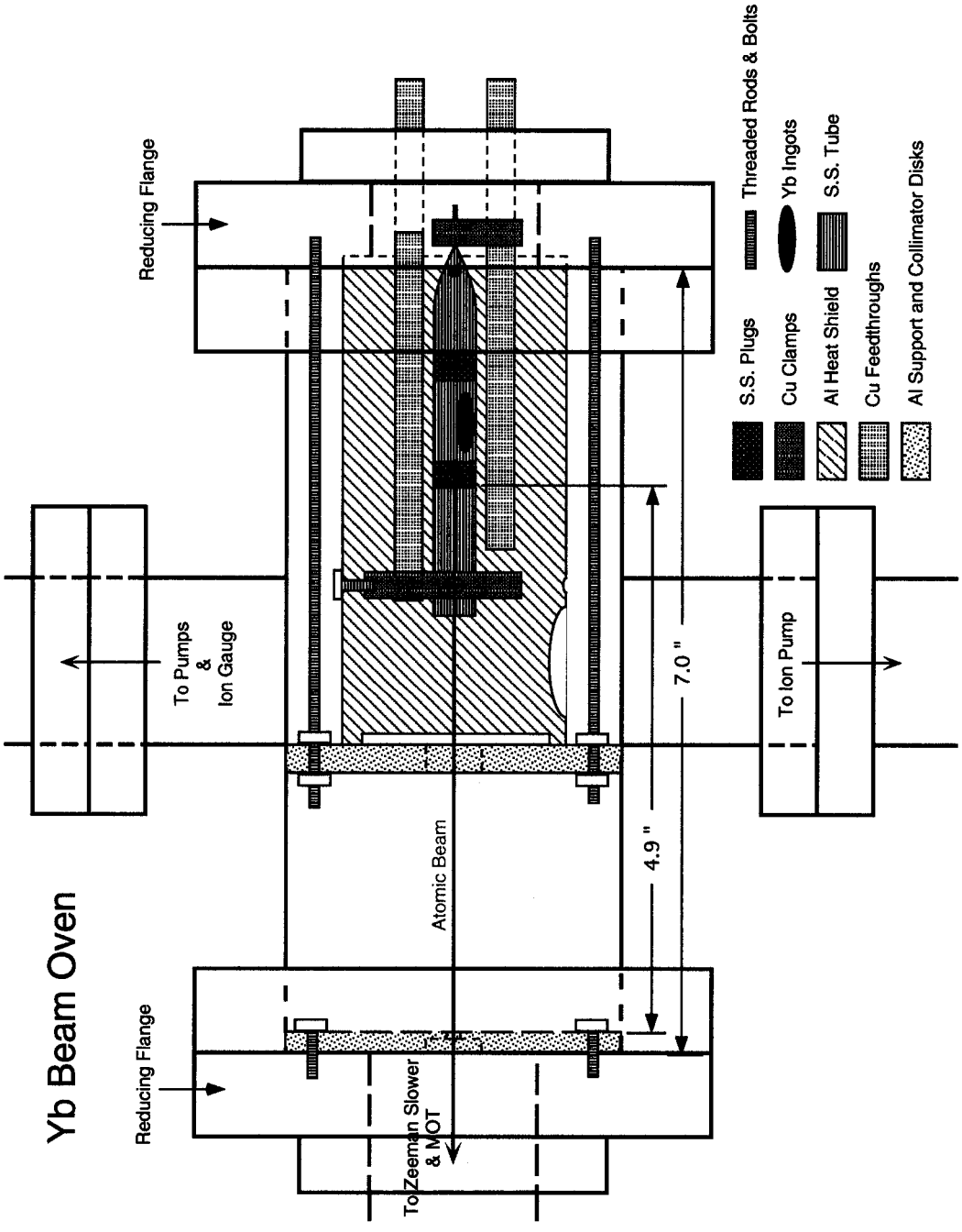

Figure 5.5: The Yb oven.

The temperature of the oven is measured in two places: at the front copper clamp, marked "Nozzle" on the thermocouple, and the back plug, marked "Middle". The operating temperature quoted throughout this dissertation is measured at the "Middle". The front thermocouple is held in place by the copper clamp, and the back is held in place by a sleeve of another layer of ss tube, 0.6" long, slit along its length and fitted over the back plug.

There are three aluminum pieces near the oven: a tube with 1.5" diameter, 4" long, which acts as a radiation shield to help heat the oven and support the front end of the oven, and two disks, one which fits snugly inside outer body to act as a support for the radiation shield, and the other acts as a collimator with a 0.08" diameter hole. The collimator is screwed directly onto the front reducing flange with the three holes that were drilled part of the way and tapped. The support disk, which has a 0.5" hole in the middle to let the atomic beam through, is held in place by three threaded ss rods which are screwed onto the back reducing flange and a couple of nuts for each rod at the aluminum disk. To avoid having trapped air in the tapped holes, the threaded rods and the bolts holding the collimator were ground down and flattened along one side. (Normally one would use vented screws with a hole through the middle, however, this cannot be done to long rods). One of the TSPs is placed in the region between the two aluminum disks to help support the pressure differential between the oven and the MOT side. When choosing materials we made sure that every alloy used is appropriate for use in vacuum. For example, aluminum jig plates have a high zinc content and should be avoided.

With the first collimator having a hole with diameter of 0.07", the second collimator with diameter of 0.08", and the distance between the collimators being 4.9", the beam divergence is 1°, which results in a 1 cm beam diameter in the MOT region. With this geometry and at 400 °C, the Yb vapor pressure is 0.74 mTorr, or 1×10^{13} atoms/cc in the oven, and the flux in the atomic beam is 1.5×10^{11} atoms/s. The density of atoms in the beam is 7×10^{6}/cc. To calculate the number of atoms in a particular isotope, multiply this by the abundance shown in Table 4.1.

The oven can be pulled out to service it or to add more Yb without affecting the vacuum on the MOT side by closing the straight-through valve shown in Figure 5.3 and 5.2, opening the right angle valve to nitrogen, then separating the two back 4-5/8" flanges.

5.1.3 Cleaning, Assembly and Bakeout

In order to achieve the ultra-high vacuum pressure of 10^{-11} Torr, it was necessary to carefully clean and bakeout the vacuum chamber. The procedure for both are outlined here. The purpose of the bakeout is to reduce surface contaminants, and to accelerate the desorption of gases that are adsorbed or absorbed on the surfaces of the vacuum chamber materials, thereby reducing the load on the pumps while in operation. When surfaces are exposed to air, large amounts of water vapor are adsorbed, as well as oxygen, nitrogen and other atmospheric gases. Hydrogen is trapped in the ss during manufacturing, and is a large source of background pressure and needs to be baked out. Some of this adsorbed gas will migrate into the bulk of the material and become absorbed. When servicing small parts of the vacuum chamber, one can vent to dry nitrogen to minimize water being adsorbed onto surfaces of the vacuum chamber.

The first step is to clean the components. All components which were worked with or machined were cleaned by immersing them in an ultrasonic bath, first of trichloroethylene, then acetone, and finally in methanol. Large components which could not fit in the ultrasonic cleaner were thoroughly rinsed with these solvents in the same order. Components that are newly purchased are cleaned by the manufacturer and do not need to be cleaned, though they should be thoroughly inspected, especially the knife-edges of the flanges for any damages.

The bakeout was carried out in three stages to bake each component at their maximum rated temperature, each for about 48 hrs. Care must be taken to ensure that the bolts and the copper gaskets which are exposed to the outside air (at least partially) do not oxidize and seize up during the bakeout. We used silver plated copper gaskets and 12-point silver plated bolts. Plate nuts also made it easier to tighten the bolts, especially in places which were difficult to reach.

In the first stage, components which could withstand 450–550 °C were baked out. This includes the main and lower MOT chambers, the Thermionics straight-through valve, the spherical cube (Green lock detection region), and the oven-side ion pump. Ports were closed with blank-offs rather than with viewports which are rated only to 400 °C. The main MOT

chamber is made of 316 LN stainless steel which has low magnetic permeability. It is more corrosion resistant and can be baked at 550 °C. The rest of the components were baked at 450 °C. We used a baking station which is equipped with its own cryogenic sorption pump (also called adsorption pump) as a roughing pump and an 30 l/s ion pump. We hooked up the components mentioned above to this, and since the baking station was designed for smaller systems, we connected another sorption pump and a Cryo-Torr 100 Cryopump from CTI-Cryogenics as an intermediate pump to go from the roughing pressure of mTorr range to 10^{-5} Torr where we can start the ion pump. The Cryo-Torr pump works by condensing and adsorbing gases and water vapors onto surfaces cooled by compressed helium, and can work in the range of 10^{-3} to 10^{-9} Torr. It was hooked outside the oven to the system by a long bellows.

The baking station consists of firebricks and oven sections which can be placed over the vacuum chamber. In addition, heater tapes were wrapped around the main chamber for additional heating. Thermocouples were placed in ten locations to monitor the temperature of the chamber, and an ion gauge was placed outside the oven to monitor the pressure. After assembly, both sorption pumps were valved off and the one at the Cryo-Torr was cooled with liquid nitrogen to rough out the system. Then the Cryo-Torr was valved off from the system to be started (see manual for start-up procedure). When it had safely started, the valve to the rest of the system was opened, and after the system was pumped down over-night down to 10^{-6} Torr, the bakeout was started. The Variacs which controlled the ovens were adjusted to bring the temperature to the desired value. When the pressure was low enough (10^{-5}), the ion pump was started. At 24 hrs, the Cryo-Torr pump was valved off, regenerated and restarted (see manual). After 48 hrs when the pressure was no longer changing, the ovens were turned off, and the system was cooled to room temperature, at which point the pressure was 7×10^{-8}, limited by the Cryo-Torr pump.

The second stage was carried out in much the same way, except that the temperature ranged from 350–400 °C. The viewports, bellows near the Yb oven, the UHV ion gauge, and the rotary feedthrough were added. This is essentially the entire system except that the insides of the Yb oven, atomic beam collimators and the titanium-sublimation pumps, and the VacIon Plus 40 ion pump were left for the final bakeout.

After the second bakeout, the main MOT chamber was taken out to wrap the magnet wires for the MOT and Zeeman slower. Three 20 AWG T-type thermocouple pairs were installed near the vacuum chamber so that the temperature of the chamber could be monitored. 1/4" copper refrigerator tubing was wound underneath the MOT coils and the Zeeman slower for water-cooling during operation to keep the vacuum chamber cool while running current through the magnet wires.

The Yb oven was filled with 3.7 g of ytterbium ingot and collimators were assembled (see Figure 5.5) and installed. The ion pump on the MOT side which was new and unused, still under factory vacuum was tested, opened, and installed. The entire vacuum system was assembled on the optical table in its final configuration supported by the custom made brackets for the final bakeout at 300–350 °C.

Firebricks were wrapped in aluminum foil to prevent brick dust from getting all over the optical table, and laid under the chamber. Ovens from the baking station were brought over and placed over the main chamber and the in-line valve and green-lock detection area, and closed off by the firebricks. The MOT-side ion pump, Yb oven, and right-angle valve did not fit under the oven and were wrapped with heater tapes. The oven-side ion pump was only partially heated since we did not have a bakeable cable for the controller.

The system was roughed out with the sorption pump, brought into the high-vacuum regime with the Cryo-Torr pump, and the ion pumps were turned on. This time the temperature was monitored at 22 locations and the pressure was monitored by the oven-side ion gauge and the current of the ion pumps. The Yb oven was turned on for a few hours for degassing, and each of the three filaments of both TSPs were degassed by running 25 Amps through one, then increasing the current slowly up to 52 Amps and leaving it there for 2 min, then repeating the same procedure for the others (see manual for details).[1] After 48 hrs, the ovens were turned off and as soon as it was cool enough to attach the UHV gauge cable, it was degassed. The Cryo-Torr pump was valved off, and the system was ready for use[2]. With the Yb oven off, and TSPs turned on for two minutes each, the pressure on the

[1] In the current setup, filament 1 on the MOT side seems be shorted to the outer chamber and is unusable.

[2] Upon baking, the ball bearings on the rotary feedthrough which are on the outside had seized up. We used 'Liquid Wrench Super Penetrant' to loosen this. It rotates freely, though not as smoothly as it did

MOT side is below 5×10^{-12} Torr, the x-ray limit of the UHV gauge, and the oven side is 5×10^{-10} Torr. When the Yb oven is on, the MOT side is roughly 10^{-10} Torr and the oven side is 10^{-6} Torr. In general, if a component is let out to air after it has been baked out, it only needs to be baked at 200 °C for about 12 hrs, as most of the absorbed gases have already been desorbed, and only water vapor that gets adsorbed onto the surfaces need to be boiled away.

5.2 *Zeeman Slower*

We have designed the Zeeman slower to get a uniform deceleration of $a = \eta a_{max}$ with $\eta = 1/3$ from initial velocity of $v_{mp} = \sqrt{3k_BT/M} = 320$ m/s at $T = 450$ °C. The magnetic field gradient is then

$$B(z) = B_0\sqrt{1 - z/z_0} \tag{5.1}$$

where $z_0 = Mv_0^2/\eta\hbar k\gamma$ is the total length of the magnet, $B_0 = \hbar k v_0/\mu'$, $\mu' \equiv (g_eM_e - g_gM_g)\mu_B$, where $g_{g,e}$ are the Landé g-factor of the ground and excited states, $M_{g,e}$ are the magnetic quantum numbers, and μ_B is the Bohr magnetron. The field was offset by about -300 gauss to avoid exerting too much force on the atoms in the MOT region.

The vacuum chamber at the MOT and Zeeman slower region was custom made to bring the Zeeman slower as close to the MOT as possible to capture as many atoms as possible out of the Zeeman slower.[3] See Figure 5.4.

A copper 1/4" refrigerator tubing is wound around the 12" long 1" diameter tube for water cooling. The Zeeman slower and the bias field coils were wound over the cooling tube by mounting the chamber on a lathe, and turning at the lowest possible RPM. The windings

---

before the bakeout.

[3]The MOT chamber was designed and purchased for an earlier setup. It is made of 316L SS for lower magnetic permeability (the lower chamber is made of 304 SS). Since then, we have come across "Spherical Cubes" made by Kimball Physics Inc (Wilton, NH, USA), which we used for the Lock-Detection area of the current setup. One of their chambers with 8 or more optical ports in one plane, in combination with a long tube with ConFlat flanges welded to either side would allow the MOT and Zeeman slower to be closer to each other. This would also greatly improve optical access to the trapping region. Wire can be wound for the Zeeman slower on the long tube more easily than if there is a chamber attached to it, and MOT quadrupole wires can be wound separately.

Table 5.1: Number of turns used in each 2 cm segment in the Zeeman slower and bias coils.

Bias	200	80	100	100	100	100	100	100	100	100	100	100	100	100	80
Zeeman	0	60	90	110	130	150	160	170	180	190	200	210	230	250	300

were divided off in to 2 cm sections by thin copper plates, which also served to carry the heat out from the wires. We chose 16 AWG "Heavy Allex" magnet wire from Essex which is bakeable to 300 °C. Its thick insulation also prevented the wire shorting to itself or the vacuum chamber as it was difficult to avoid the wire from occasionally getting snagged on the copper fins.

The magnet wire winding was sectioned by copper fins in to 2 cm segments which served to conduct heat out from the wires and to control the number of turns in each segment. The number of turns were calculated and modeled to achieve the magnetic field gradient as described in Equation 5.1. The number of turns of the magnet wire at the ends of the bias coils were adjusted to bring the field to zero outside the slower as quickly as possible. See Figure 5.6 for the magnetic field gradient of the Zeeman slower and Table 5.1 for the actual number of turns in each segment.

We typically use 4–8 mW laser power for the Zeeman slower. An AOM (acousto-optic modulator, Brimrose TEF-150-30-.400) in a double-pass configuration was employed to obtain a nominal frequency shift of 300 MHz. The double-pass configuration has the advantage over the single pass configuration in that the beam is not steered. We get about 50% of the laser power shifted to the desired frequency in each pass, for an overall efficiency of 25%. Figure 5.7 shows the optical layout.

The MOT loading is typically more efficient with higher laser power, both in the Zeeman slower and the MOT Beams. The end window directly opposite of the oven nozzle collects ytterbium and occasionally needs to be cleaned. After a few months of heavy operation, a spot of about 1 cm will appear on the window and prevent the Zeeman slower laser from entering the vacuum chamber. The ytterbium can be blown away from the window by running a heat gun about 10 cm away from the window for about 30 minutes. We monitor

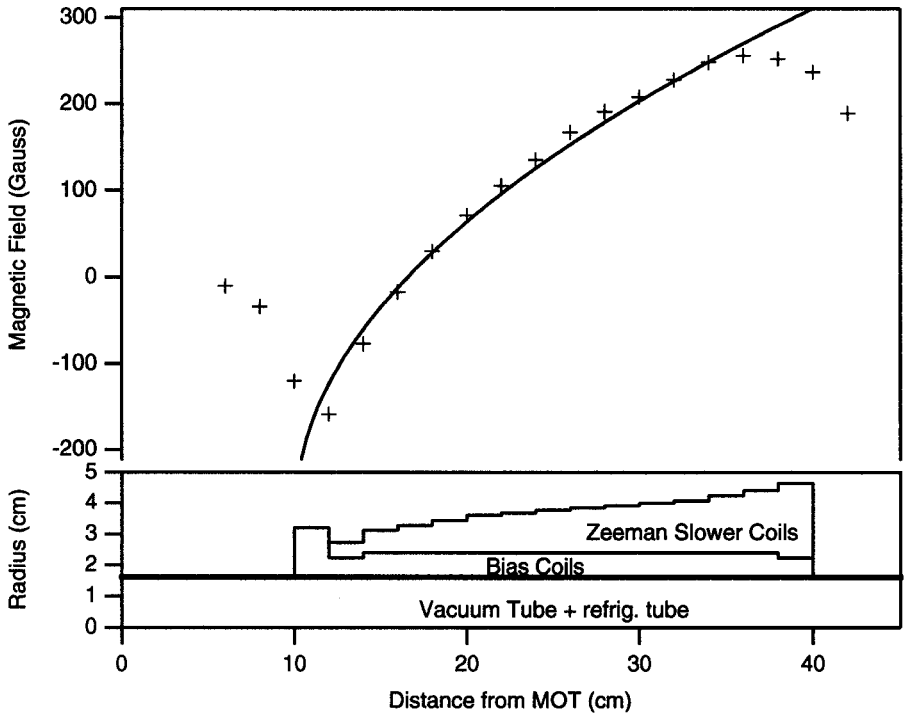

Figure 5.6: Magnetic field gradient of the Zeeman slower and the radius of each section. On top, the solid line is the magnetic field gradient calculated from Equation 5.1 with $B_0 = 580\,\text{gauss}$, $z_0 = 30\,\text{cm}$, and bias offset of $-270\,\text{gauss}$. Crosses are the field measured before the system was assembled and pumped out with 4A running through both Zeeman slower and bias coils. The bottom shows the physical size of the coils (radius) wound around a 1" tube and 1/4" refrigerator tube for cooling.

the temperature of the flange around the window to make sure that it does not go above 350 °C. The pressure in the vacuum chamber is monitored to ensure that the vacuum remains intact. Aluminum foil was placed around the flange in a funnel-like shape to shield the optics and rest of the system. The performance of the Zeeman slower is discussed in Section 7.2 and the electronics schematic of the current control driver is shown in Figure A.1.

5.3 MOT Design

The magnetic quadrupole field is produced by a pair of magnet wire coils wrapped directly on the main MOT chamber. The MOT coils were wound by hand after the second bakeout

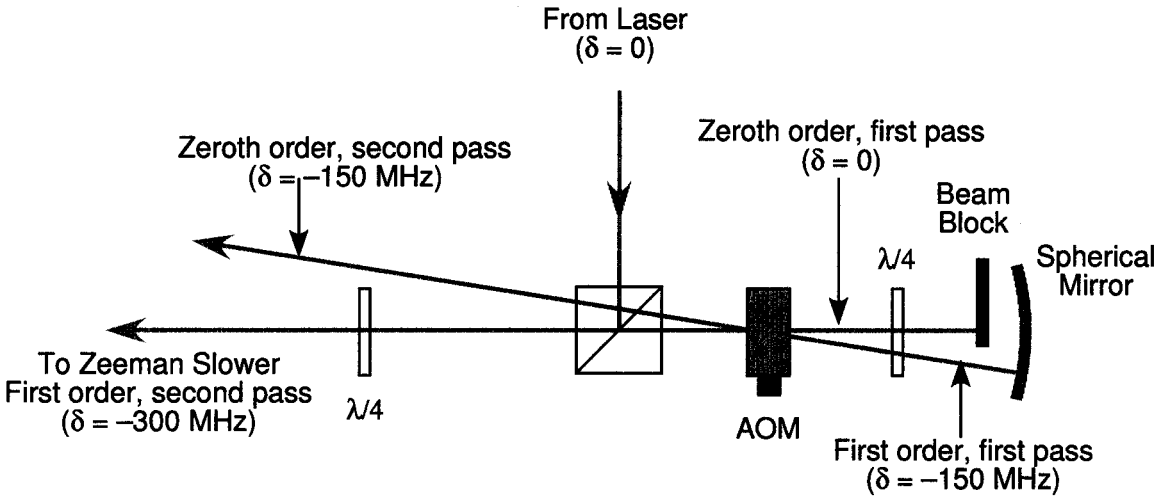

Figure 5.7: AOM double pass setup for the Zeeman slower. Note that the beam that is steered toward the RF power connector is shifted down in frequency.

and prior to the final bakeout. 1/4" thick Aluminum plates were cut into rings to fit snugly around the main part of the MOT chamber to form a channel for the quadrupole coil with the 4-5/8" flanges. There are 100 turns each for the top and bottom coils wrapped onto the 3" diameter MOT chamber cylinder. The coils have a cross section of 1" ×1", therefore the radius to the center of the cross section is $R = 1.75$", separated by $d = \sqrt{3}R = 3$" (measured between the centers of the coils). The resulting magnetic field gradient is 5 G/cm/A, and we typically run 6 A of current for the blue MOT to produce 30 G/cm.

Care was taken in designing the Zeeman slower to minimize the residual magnetic field at the center of the MOT. However, the optimal current for the Zeeman slower and bias coils change depending on the laser power, and it is not possible to design the Zeeman coils to have no field at the MOT location for all current combinations. Figure 5.8 shows the magnitude of the magnetic field near the center of the MOT along the axis of the Zeeman slower with 4 A of current in the Zeeman slower, 4 A in the bias coils, and 6 A in the MOT coils. The beginning of the Zeeman slower is located at −40 cm of the horizontal axis in this figure. As the current in the Zeeman slower and the bias coils are varied, the offset to the MOT magnetic field varies. The field can be corrected by adding an extra coil at

the viewport opposite the Zeeman slower. We did not notice an appreciable difference in the performance nor the location of the MOT with the extra coil. The current of the MOT coils is controlled by a MOSFET as shown in Figure A.1. The external current control of the MOT coils can be used to completely turn off the MOT magnetic field gradient in less than 400 μs.

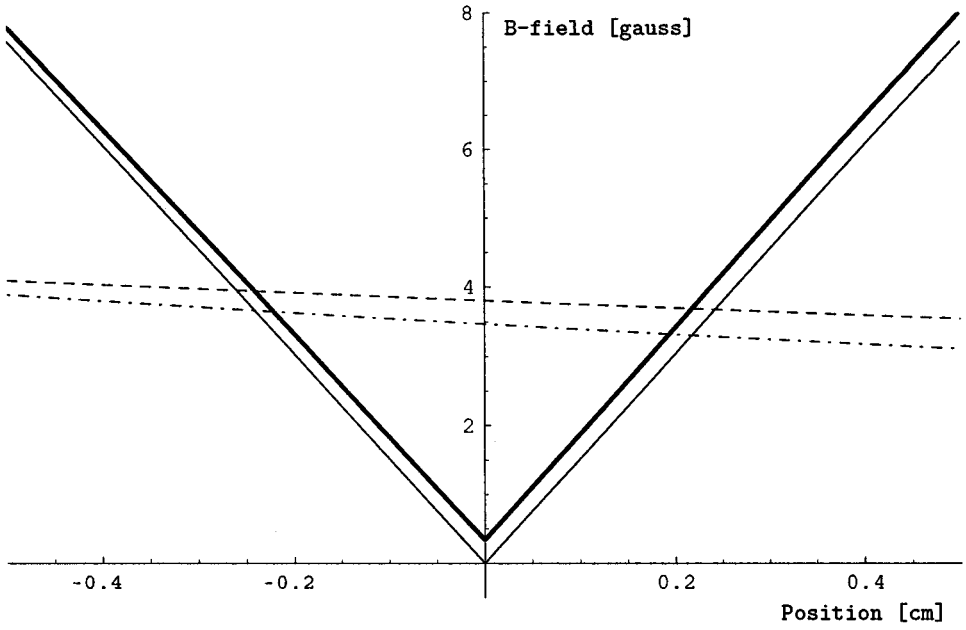

Figure 5.8: Magnetic field near the center of the MOT along the Zeeman slower axis, perpendicular to the axis of the MOT coils with 4 A of current in the Zeeman slower, 4 A in the bias coils, and 6 A in the MOT coils. The beginning of the Zeeman slower is located at -40 cm. The dashed line is the field from the Zeeman slower, skip-dashed line is the negative of the bias field, solid line is the magnitude MOT field, and the thick line is sum of all three. The vertical axis is in [gauss], and the horizontal is in [cm].

Chapter 6

LASERS

This chapter describes the laser systems for this experiment. Yb has two levels accessible from the ground state, $^1S_0$–$^1P_1$ and $^1S_0$–$^3P_1$, and needs no repumping lasers (see Figure 4.4). The required wavelengths are 399 nm and 556 nm.

The 399 nm laser is a Titanium:sapphire laser with its frequency doubled by a lithium triborate doubling crystal housed in an external enhancement cavity. This combination provides high power and stability that is essential for forming a good MOT. Because this transition has a broad width of 28 MHz, the saturation intensity (I_s) is relatively large at 70 mW/cm^2, making the required laser power higher than in alkali-metals. The details of the laser system including frequency doubling are described in Section 6.1.

The $^1S_0$–$^3P_1$ transition requires a laser at 556 nm, and a dye laser is the practical choice at this wavelength. This transition has a much narrower width of 190 kHz, making it necessary to narrow the laser linewidth from 1 – 2 MHz achieved by the commercial system. On the other hand, this transition requires less power with $I_s = 0.14\,\mathrm{mW/cm^2}$. The details of this laser are described in Section 6.2.

We were fortunate to have the use of two argon-ion (Ar^+) lasers (one Coherent Innova-400 and the other is a Sabre, both with 25 W tubes) and two Coherent 899-21 lasers, one used as a Ti:sapphire and one as a dye laser. We are indebted to Warren Nagourney and the Laser Facility at the University of Washington for the use of these lasers. This work benefits from the past and present in-house expertise in frequency doubling. Much of the details are explained in past Ph. D. theses by Burt [Bur95], and Klipstein [Kli96b] at the University of Washington, as well as the thesis by Sandberg from MIT [San93].

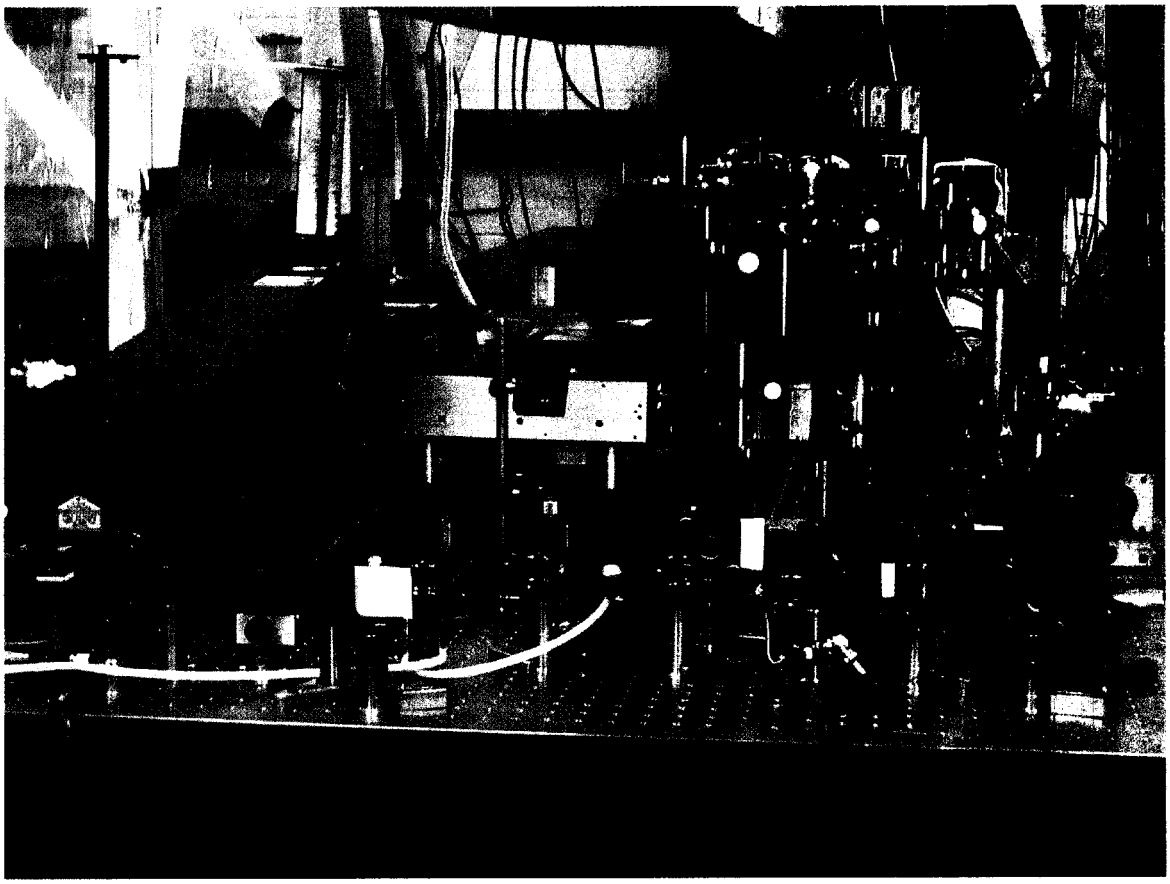

Figure 6.1: Photograph of the 399 nm laser. The black box on the left is the Ti:sapphire lasing at 798 nm, and the brightest purple glow is the LBO crystal.

6.1 Blue Laser

There are currently three types of lasers available at 399 nm: dye lasers, frequency-doubled titanium:sapphire, and blue diode lasers which became commercially available in 2001. For our experiment, an LBO crystal frequency-doubled Ti:sapphire laser (Coherent 899-21) pumped with an argon-ion (Ar^+) laser (Coherent Innova 400) was chosen for its high power output, stability, and wide tunability. Dye lasers pumped by Ar^+ can supply no more than 150 mW at the desired wavelength. Furthermore, dye lasers are notorious for being unstable and having the performance deteriorate with the age of the dye. It was not until recent that the option of blue diode lasers have become commercially available from Nichia, a company in Japan.[1] It is by chance that these happen to lase at around 400 nm, and as Nichia and Cree have recently settled some legal issues surrounding their patents and Nichia has signed an agreement with Sony for a joint development, we can perhaps look forward to these diodes becoming cheaper and more widely available. They have diode lasers between 400–420 mW which can output 30 mW, not quite enough to operate both the Zeeman slower and blue MOT, but quite sufficient to run the Zeeman slower. In contrast, 200–300 mW of laser power at 399 nm is available in our system.

6.1.1 Titanium:Sapphire Laser

Much of our effort was spent on maintaining the Ti:sapphire laser. As the laser comes with a comprehensive owner's manual which has the details on alignment and daily operation, I will only mention procedures that either deviate from it or are particular to our system. For stable intensity, it was important to have the pump beam going through the crystal in just the right place, close to the edge toward the output coupler. The laser was more sensitive than it should have been to the alignment of the two small black knobs at the front of the ICA (intra-cavity assembly). As we had access to two Ti:sapphire crystals, both were tested and we found that there was much more scattering of the pump from one. Upon discussing this with a technician from Coherent, it was decided that this crystal was damaged, and the crystal was replaced. Both crystals were found to have thermal effects,

[1] http://www.nichia.co.jp/

and it took a few minutes of having the Ar^+ pump laser going through the crystals before the Ti:Sapphire output power and frequency was stable. This is attributed to insufficient cooling of the crystal. The crystals are held in mounting blocks which are water cooled. Since we purchased the lasers, Coherent has changed the design of the Ti:sapphire crystal mounting blocks to have a larger surface in contact with the crystal for cooling the crystals more effectively.

We lose about 25% of the power when we insert the ICA to make the laser operate in a single mode. Although this is close to what Coherent specifies in their manual, there have been reports of as little as 10% loss when the ICA unit was sent back to Coherent to be cleaned and realigned [Lof02b]. This may be something we would like to try, as it may also fix the problem with the over-sensitive black knob adjustment.

The wavelength is measured with a wavemeter from Burleigh (model WA-20 DL). It has a resolution of $\pm 0.001\,\text{nm}$ in wavelength mode, or $0.01\,\text{cm}^{-1}$ in wavenumber mode. The Yb resonance lines at the doubled frequency can be found by tuning the Ti:sapphire to 797.822 nm and sweeping over 2 GHz.

6.1.2 Frequency Doubling Crystal: LBO

The doubling crystals available for obtaining second harmonic generation (SHG) near 400 nm are lithium triborate (LBO for short, LiB_3O_5), beta barium borate (BBO), or lithium iodate ($LiIO_3$). LBO was chosen for its superior second harmonic conversion coefficient at this wavelength, low walk-off angle, and high damage threshold. It is possible to achieve high conversion efficiency with the crystals placed in external enhancement cavities. 40% conversion with the fundamental at 746 nm [Kum01] and 53% at 850 nm [Jur02] have been observed in setups similar to ours. We obtain about 200 mW of SHG with 2 W of fundamental for 10% conversion efficiency, but the crystal has been deteriorating over the years, and the current efficiency is as low as 5%. The reasons for crystal deterioration and improvements that could improve the efficiency will be discussed later in this section.

There are some references which give detailed discussion of nonlinear crystals, SHG, and uniaxial crystals [Yar75, San93, Boy68] and I will only mention the parameters essential

Table 6.1: Indices of refraction of LBO at 798 nm and 399 nm. LBO is a negative biaxial crystal, with the principal axes X, Y, and Z ($n_z > n_y > n_x$) parallel to the crystallographic axes a, c, and b respectively.

wavelength	n_x	n_y	n_z
797.8 nm	1.5695	1.596	1.611
398.9 nm	1.590	1.620	1.635

to the operation and re-construction of our system. The response of ordinary materials to an electric field is linear. However, certain classes of crystals have nonlinear optical susceptibility and can produce polarization that is proportional to the square of the applied electric field, and in these crystals, electromagnetic waves at frequencies twice the incoming (fundamental) wave can be produced. To have the SHG waves generated at one plane in the crystal propagate without destructively interfering with SHG from another plane, it is important to match the refractive indices of the fundamental wave and the SHG. This is called "phase matching". In general the indices depend on the optical frequency, and it is not possible for the indices to be the same at different frequencies. However, nonlinear crystals possess birefringence, that is, they can sustain an "ordinary" and an "extraordinary" rays with different indices of refraction, n_o and n_e. The indices can be tuned with either temperature or angle of wave propagation of the fundamental with respect to the crystal axis such that the index of refraction of the ordinary wave of the fundamental, $n_o(\omega)$, is equal to the index of refraction of the extraordinary wave of the doubled frequency, $n_e(2\omega)$, that is, $n_o(\omega) = n_e(2\omega)$.

LBO is a negative biaxial non-linear crystal, and the indices of refraction at 798 nm and 399 nm are listed in Table 6.1 [Cas]. The crystal does not allow temperature-tuned phase matching at 797.8 nm fundamental, and it must be angle tuned. Frequency doubling of a laser at 797.8 nm to 398.9 nm requires type I phase matching in the principal XY plane with cutting angle of $\theta = 90°$ and $\phi = 31.9°$ of the crystal. Our crystal is cut to the Brewster angle which is 58.2° at 797.8 nm, has a physical size of $3 \times 3 \times 7$ mm, and purchased from Castech.

Calculating various parameters necessary for choosing the right crystal and designing an appropriate enhancement cavity is made simple by a software named SLNO made by Sandia National Laboratories.[2] The characteristic values calculated by this software are listed in Table 6.2. Note that the indices of refraction are equal at this angle, $n_o(\omega) = n_e(2\omega) = 1.611$, and the walk-off angle is $16.56\,\text{mrad} = 0.9°$. For comparison, the BBO crystal used in the Hg EDM experiment has a walk-off angle of about 5°. As the crystal is slightly hygroscopic, we have devised a mount which allows us to flow dry air over the crystal. Laboratory compressed air is filtered through a tube filled with desiccant pellets from Drierite, with cotton stuffed on either ends to keep the Drierite dust from reaching the crystal. The flow rate of the dry air is controlled with a valve so that when a 1/4" tube is connected and the outlet is immersed under water, there are about two bubbles forming every one second.[3] The crystal is encased in a small cap which has two small holes drilled for the light to go through, and dry air flows up from the base of the mount, and into the cap which is then slightly over-pressurized, and out the two holes. Other people using BBO (which is also hygroscopic) have reported success by flowing oxygen or dry nitrogen over their crystals.

6.1.3 Frequency Doubling: SHG Enhancement Cavity

Figure 6.2 shows the design of the SHG enhancement cavity. The goal of the design of the enhancement cavity is to have as much of the fundamental wave circulating in the cavity as possible. The output of 797.8 nm from the Ti:sapphire laser is vertically polarized, and after a periscope it is horizontally polarized. It goes through a polarizing beam splitter to clean out the residual polarization that can affect the error signal, then through two lenses which help mode-match the laser into the cavity. The cavity consists of a 98% reflective input coupler (IC) which is 0.5" dia. × 0.375" thick, a small high reflector (1/4" dia. × 1/16" thick), and two concave mirrors, both with a 7.5 cm radius of curvature, 1/4" dia. × 1/8" thick. The IC is from CVI Laser Corporation (PR1-800-98-0537), and the other three were custom coated by Research Electro-Optics (REO) for high reflectivity at 800 nm (> 99.99%)

---

[2] http://www.sandia.gov/imrl/XWEB1128/xxtal.htm

[3] This flow rate may be increased until effects of air flowing can be seen. The two-bubble rule is by no means a strict rule.

Table 6.2: Characteristic values for frequency doubling of $\lambda(\omega) = 797.8\,\text{nm}$ to $\lambda(2\omega) = 398.9\,\text{nm}$ by an LBO crystal (calculated by SNLO from Sandia National Laboratories).

Cutting angle

$\theta = 90°$

$\phi = 31.9°$

Brewster angle

$\theta_B = 58.2°$

Crystal size

cross-section = 3×3 mm

length = 7 mm

Field Gain coefficient

$7.88 \times 10^{-5}/\sqrt{W}$

Effective SHG coefficient

$d_{eff} = 0.747 \times 10^{-12}$ m/V

Crystal Angle Tolerance

1.5 mrad cm

Fundamental index

$n_o(\omega)$=1.611

$n_e(\omega)$=1.5885

walkoff(ω) = 15.16 mrad

Second harmonic index

$n_o(2\omega)$=1.634785

$n_e(2\omega)$=1.611

walkoff(2ω) = 16.56 mrad

Table 6.3: Properties of the enhancement cavity.

Cavity properties:

- Input coupler reflectivity = 98%
- Length of crystal = 7 mm
- Radius of curvature of mirrors around crystal = 7.5 cm
- Distance between two curved mirrors = 8.2 cm
- Waist = $w_0 = 25\ \mu$m
- Confocal parameter = $b = 2\pi w_0^2 n/\lambda = 7.4$ mm

and high transmission at 400 nm. Note that the reflectivities are all in terms of intensity. The substrate of the REO optics are super-polished BK7 and the coatings are ion-beam sputtered. The small high-reflector is attached to a piezoelectric transducer (PZT) by UV curing glue, which in turn is glued to an aluminum disk that can be mounted in a mirror mount. The optics forming the doubling cavity are mounted on 0.5" Lees optical mounts (recently bought by LINOS), which we find to have high stability and little hysteresis.

The cavity is designed to have a waist at the crystal of $w_0 = 25\,\mu$m with a confocal parameter of $b = 2\pi w_0^2 n/\lambda = 7.4$ mm. Boyd and Kleinman [Boy68] explored the optimal length of a crystal, l, and found it to vary between $l/b = 1.39$ for crystals with large walk-off angle and $l/b = 2.84$ for those with small walk-off angle. LBO has a relatively small walk-off angle and we may benefit from using a crystal which is as long as 20 mm.

Another improvement that can be made to the current doubling cavity setup is through astigmatism compensation. The astigmatism introduced by the optics can be canceled by the astigmatics introduced by the Brewster cut crystal. The two effects *partially* cancel each other when the angle of incidence on the mirrors inside the cavity, θ_i, meets the following criteria:

$$R \sin\theta_i \tan\theta_i = 2l(n^2-1)\sqrt{n^2+1}/n^4 \tag{6.1}$$

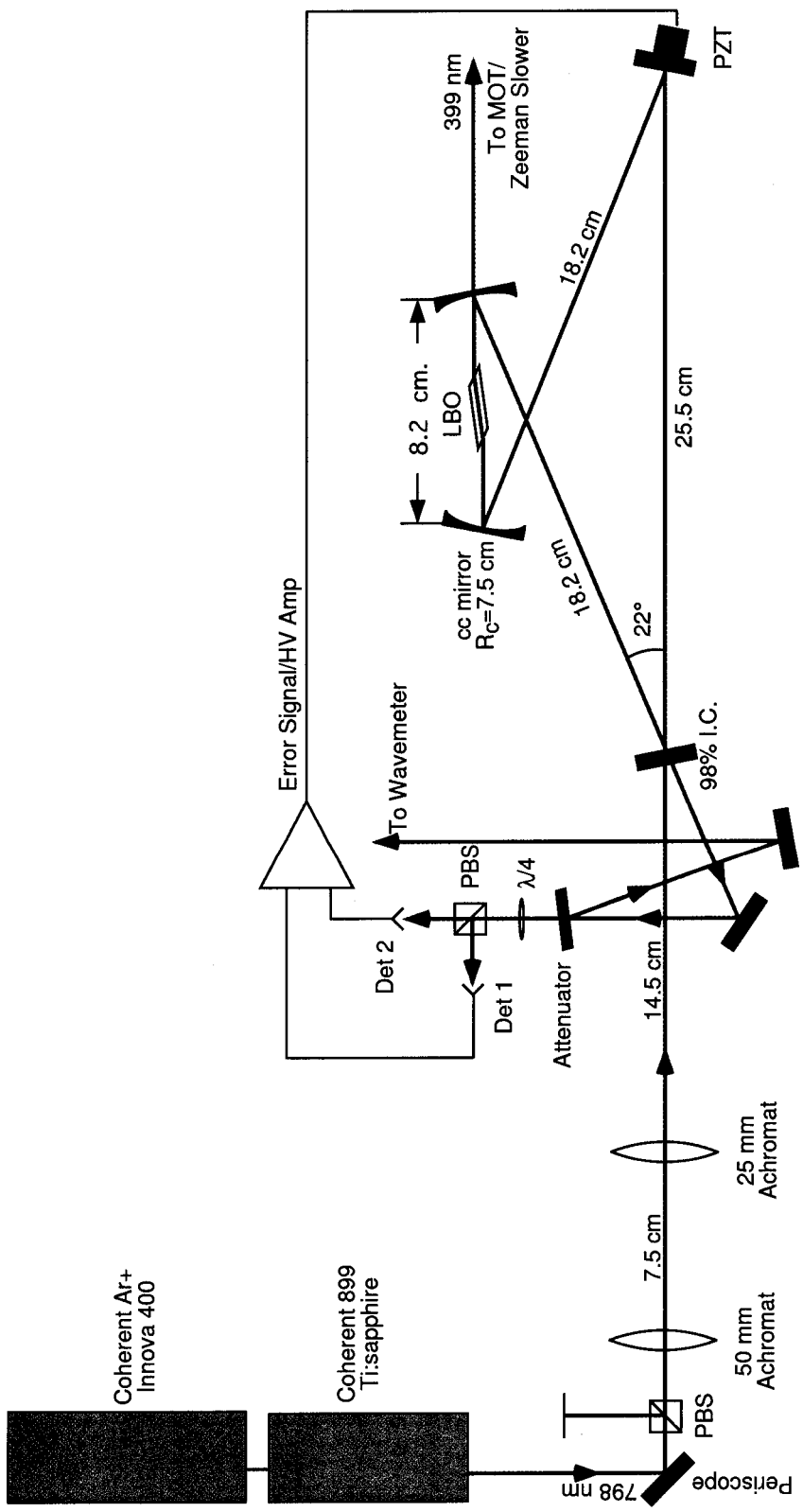

Figure 6.2: The SHG enhancement cavity. The crystal is 7 mm long (not to scale). The input coupler (IC) is 98% reflective, the other three mirrors are > 99.9% reflective at 798 nm. All are transparent to 399 nm.

where for our cavity, $R = 75\,\text{mm}$ is the radius of the curvature, $l = 7\,\text{mm}$, $n = 1.611$, $\theta_i = 16.5°$. Currently, this angle is 11°(22°shown in Figure 6.2 is $2\theta_i$), and we may be able to improve upon the cavity impedance matching by satisfying this condition better.

The enhancement, A, in a perfectly aligned and mode-matched cavity is

$$A = \frac{1 - R}{(1 - \sqrt{RV})^2} \tag{6.2}$$

where R is the IC reflectivity and V is the total fraction of power remaining in the cavity after one trip and takes into account the losses in the fundamental power from the other three mirrors and crystal. The enhancement is maximized when R is chosen such that $R = V$, and

$$A = \frac{1}{1 - V}. \tag{6.3}$$

The rough estimate of enhancement can be measured experimentally by measuring the power leaking out of the cavity from one of the mirrors when the cavity is well aligned (the left curved mirror for example), and dividing by the measured power at the same place when the input coupler is taken out. From Equation 6.3 and knowing R of the input coupler, V can be calculated. The cavity finesse, F, then is

$$F = \frac{\pi (RV)^{1/4}}{1 - \sqrt{RV}}. \tag{6.4}$$

When the doubling cavity was first set up a few years ago, the measured enhancement was about 50. With the 98% input coupler, this suggests that the losses were well matched, and V was also 98%. The recent measurement yielded enhancement of about 25, suggesting that the total loss in the cavity has increased to 4%. Indeed, we have noticed that the scattering from the LBO crystal has increased noticeably, and when the cavity is locked, a significant amount of red light is scattered. The SHG efficiency varied dramatically across the cross section of the crystal and appreciable SHG efficiency could be achieved only when the laser was going through very close to the bottom edge of the crystal, near the holes where dry air flows out into the crystal mount enclosure.

Recent work has indicated that the crystal may be damaged more readily by moisture than indicated the manufacturer. In an attempt to improve the doubling efficiency and for ease of optics alignment, the crystal holder was rebuilt. The air outlet holes in the new

design were located further away from the crystal face, and within two weeks, we began to notice further deterioration of the performance of the frequency doubling cavity. The cavity became much more sensitive to alignment, and the usable area of the crystal became increasingly small.

We have since then installed a new longer crystal. The crystal specifications are the same as above, except that the length is 15 mm. The result is a much improved performance, with less sensitivity in alignment and the conversion efficiency is much more uniform across the crystal. The crystal mount was redesigned to allow higher dry air flow rate. We noticed in developing this new setup that the astigmatism compensation approximations made to formulate Equation 6.1 are no longer valid for the long crystal. The cavity was seen to operate better with θ_i as small as possible without clipping the cap enclosing the crystal, which, in the current setup at the writing of this dissertation, is roughly 30°. With this new crystal, we are able to obtain 300 mW of SHG with 2 W in the fundamental for 15% conversion efficiency. The cavity design is still under development and we expect more improvement in the near future.

6.1.4 Frequency Doubling: Locking Electronics

To lock the cavity to the fundamental, the Hänsch-Couillaud scheme is used [Han80]. The doubling crystal acts as a polarization sensitive element in the cavity, and the light reflected from the cavity at the input coupler acquires a frequency-dependent elliptical polarization. The reflected beam goes through a quarter waveplate and a polarizing beam splitter cube sends the two polarizations to two detectors (Det 1 and Det 2 in Figure 6.2). The signal on the two detectors are compared with each other, and as the cavity is swept in length, a dispersion shape can be created. The cavity is locked to this error signal by integrating and amplifying it to control the PZT on one of the flat mirrors in the doubling cavity. The details of these electronics follow the example of the thesis by Burt [Bur95] and Sandberg [San93]. There was a slight modification made to allow us to control the gain of the two detectors independently, which accounts for slight differences in the response of individual photodiodes. To stabilize the error signal, it was necessary to

clean up the polarization of the output of the Ti:sapphire laser and a polarizing beam splitter cube was placed before the mode-matching lenses. The output coupler of the doubling cavity also reflected some SHG back toward the input coupler, which is mostly transparent to 399 nm. A color filter was placed in front of the polarization analyzer to prevent the SHG from contaminating the the error signal.

After tweaking up the cavity mirrors and crystal for maximum fringes, the lock is established with the following procedure. The cavity is swept while monitoring the error signal. With the light to the detectors blocked, the overall offset of the signal is brought to zero. With the detectors now unblocked, the $\lambda/4$ waveplate is adjusted so that the signal is either at maximum or minimum near zero depending on its sign. Then the gain of each detector is adjusted so that the error signal is centered around zero. The lock switch can now be engaged, which also shuts off the sweeping, and the overall gain of the system can be turned for minimum disturbance to the locked error signal.

6.2 Frequency Stabilized 556 nm Green Laser

The laser requirements for trapping Yb atoms using the $^1S_0$–$^3P_1$ line are discussed in Chapter 8. To trap and cool the ytterbium atoms using this transition, we need a laser at 556 nm. Because the transition has a linewidth of 190 kHz, we need to further stabilize the laser from the nominal width of the commercially available ring dye laser of ~1 MHz to a width comparable to 190 kHz.

The laser lock can be described in two parts: short term and long term stability. The short term stability, often called "jitter," refers to fast fluctuations in the laser frequency and comes from bubbles in the dye jet, acoustical coupling, or any other fast sources of noise in the system. The 899-21 comes with its own reference cavity to which the laser is locked to, and slow drift in its length affects the long term stability. It can be measured against an absolute frequency reference like an atomic transition, and the laser will drift on the order of 1 MHz/min depending on external conditions and how well it is aligned. Coherent claims a 500 kHz laser linewidth (the short term, or "jitter"), however, we found that under normal operation, 1 MHz was a more realistic measurement of the laser linewidth.

To improve the short term stability, the laser was locked to an external cavity using a FM sideband technique, also called Pound-Drever-Hall scheme, following the examples of Sandberg [San93] and Burt [Bur95], as discussed in Section 6.2.2. For long term stability, the external cavity is locked to an Yb transition, and the details of this are discussed in Section 6.2.3.

6.2.1 Ring Dye Laser

As the light source for the 556 nm $^1S_0$–$^3P_1$ transition, we use a Coherent 899-21 in a dye laser configuration with Rhodamine 560 chloride (formerly named Rhodamine 110) dye pumped by an argon-ion laser (Ar^+) lasing multi-line visible (MLVS). Coherent recommends pumping this particular dye with a single line Ar^+ at 514 nm. To get the necessary power at 514 nm, we had to run the Ar^+ at full current of 60 A. We found that we can run the Ar^+ laser at 35 A to get 6 W of MLVS and still get the same power out from the dye laser. The result is that the dye has a slightly shorter lifetime. Rhodamine 560 is a a relatively robust dye, and as our power requirements are not very strict, we found that we could run for two weeks of heavy use without a dye change, allowing us to work in a condition which puts less strain the Ar^+ laser. We typically obtain 300 mW of 556 nm single mode with 5.5 W of pump.

Coherent has built the 899-21 laser to optimize flexibility, tunability, and cost. It can be made to lase anywhere between 370 to 975 nm simply by changing the dye, a few optics, and in some cases, the pump laser, and scan up to 30 GHz without a mode hop, with linewidth down to 500 kHz. It can also be turned into a Ti:sapphire laser, which can operate between 700 to 1100 nm, as described in Section 6.1.1. In all of these configurations, the same electronics and scheme are used for stabilization. Sandberg describes in detail the workings of a Coherent 699 laser, the predecessor to the 899 series which also uses the same stabilization mechanisms. The electronics are still exactly the same, and the driver electronics schematics that Coherent used to provide with the 699 manual can be used to debug the 899 electronics.

The 899 without its mode selection optics will lase with many different longitudinal

modes. There are three etalons in the cavity that help select the mode: the birefringent filter, thick etalon, and thin etalon. The birefringent filter selects about 10 modes. The thin and thick etalons are encased in the ICA (Intra-cavity assembly), the thin etalon narrows it down to two or three modes, and the thick etalon selects the last mode. Typically, 30% of the power is lost when the ICA is inserted to go from multi-mode to single mode lasing.

The 899-21 is actively stabilized to its own reference cavity with a Brewster plate for low-frequency corrections and a mirror mounted on a PZT (also called tweeter) for high-frequency corrections. The Brewster plate has a bandwidth of approximately 50 Hz and can provide frequency excursion of up to 30 GHz. The tweeter can respond with a bandwidth of approximately 5 kHz, and up to 1 GHz of excursion.

Several modifications in addition to the narrow lock were made to improve the stability of the dye laser. Because the lasing medium is a moving dye, the dye jet and the dye circulating system are handled with great care to ensure smooth dye flow. We have placed a flow damper between the circulator and the dye jet, into which the dye first flows into a reservoir along its side wall, and the trapped air above it damps any fluctuation in the pressure, and minimize the bubbles formed in the dye (see Figure 6.3). We also replaced the string-wound dye filter in the circulator originally supplied by Coherent with a paper cartridge (Filterite AXVR200-05M10S). It is expected to introduce fewer bubbles to the dye jet. Sandberg's thesis also mentions replacing the dye jet and circulator with those manufactured by Radiant Dyes to allow for higher pressures and higher flow rate in the dye jet. Our requirement is not as stringent as theirs, and we decided to use the original dye jet and circulator. To minimize disturbance in the reservoir in the circulator, it was important to have enough dye while in operation so that the return tube is filled near the reservoir. With the addition of the damper, 1 L of ethylene glycol as specified in the manual is no longer enough, and instead, the recipe is now 1.26 g of Rhodamine 560 dissolved in 80 mL of methanol, mixed with 1.75 L of ethylene glycol.

The electronics was modified as well. The error signal path of Coherent 899 electronics was broken at R17 on board 1A9 (see Figure 6.4), and routed to the back of the driver box to allow us to insert our own signal to control the servo transducers. The details of this will be described in Section 6.2.2.

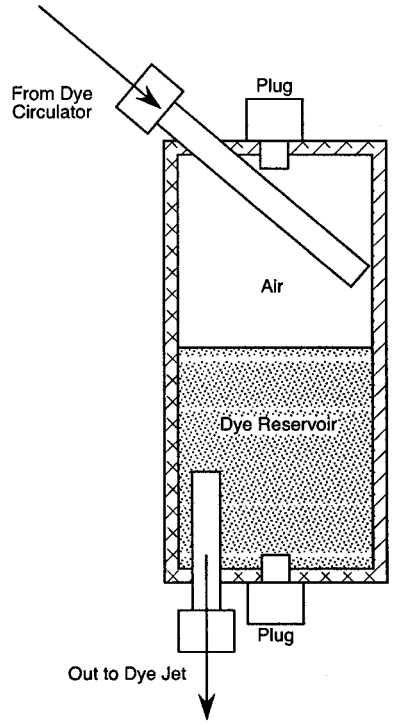

Figure 6.3: The dye damper reservoir. The dye comes in from the circulator through the connection on top, runs down the wall and collects at the bottom. The volume of the air acts to damp out the pressure fluctuations, and bubbles are taken out, and the dye is forced out the bottom. The bottom plug can be taken out to drain the reservoir when changing the dye.

To increase the response bandwidth of the feedback, an intracavity EOM (electro-optic modulator) was introduced in the laser cavity between M5 (upper fold mirror) and M4 (output coupler). An aluminum mount was constructed to hold the EOM at a Brewster angle. The EOM was purchased from Linos Photonics (model PM 25), and is equipped with Brewster windows and separate banana plugs for the two electrical inputs to allow for fast low voltage signal on one side, and slower, high voltage on the other (more on this in Section 6.2.2). The two Brewster windows are oppositely tilted to cancel out beam displacement, and the EOM can be inserted into the cavity without loosing the lasing and with only a few percent of power loss.

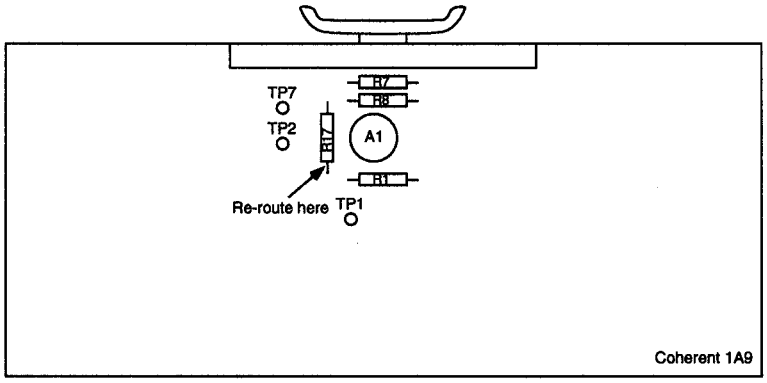

Figure 6.4: Modification to Coherent electronics. The error signal path was broken at R17 of the board 1A9 and was routed to the back of driver box.

6.2.2 Short Term Stability: FM Sideband Locking

To accommodate the narrow 190 kHz linewidth of the $^1S_0$–$^3P_1$ transition, it was necessary to stabilize the laser to < 200 kHz, down from the 1 MHz width we were getting from the Coherent servo. We employed the Pound-Drever method, also called frequency modulation (FM) sideband method [Dre83]. Much work has been done on the subject, and laser stabilization at the millihertz level has been achieved using similar methods [Sal88]. See [Boy96] for an introductory text on the subject. We have followed closely the scheme described in Burt's dissertation, and as the stability requirements are much less stringent than these earlier works, I will only describe the essentials specific to our system.

Figure 6.5 summarizes the overall scheme of our system. A portion of the output from the Coherent 899-21 laser is sectioned off for the laser narrowing. Sidebands at 14 MHz are added to the laser by introducing phase modulation with an EOM, and the light is mode-matched into the TEM_{00} mode of the Fabry-Perot interferometer (FPI) cavity with two lenses. With a quarter waveplate placed in front of the FPI and a polarizing beam splitter cube, the beam that is reflected off from the input coupler and the beam which comes back out from the cavity (leakage beam) are sent toward a fast detector (Err. Det. in the figure). The error signal is produced by phase-sensitive demodulation of the signal detected by the photodiode with a double-balanced mixer against the rf source driving the EOM.

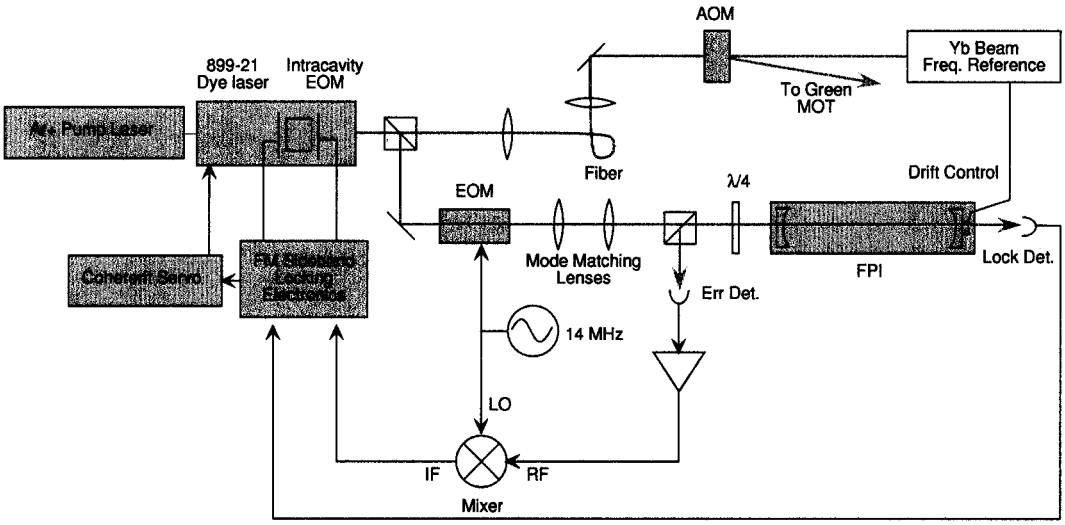

Figure 6.5: The schematic of the FM sideband frequency stabilization.

Figure 6.6 shows the transmission from the FPI cavity and the error signal (IF output from the mixer) as the cavity length is scanned. The sidebands are at 14 MHz from the center (carrier) peak, and the width of the carrier is roughly 1 MHz. To understand how the error signal is produced, consider the cavity when it is on or near resonance with the carrier. The sidebands are not on resonance with the cavity and are mostly reflected by the input coupler. The carrier that is reflected and the leakage field coming back out from the cavity are 180 degrees out of phase with each other. When heterodyned with the local oscillator sidebands with the double-balanced mixer, the result at the IF port of the mixer is an antisymmetric frequency discriminator curve as seen in Figure 6.6.

The amount of energy put into the sidebands can be adjusted by changing the RF power that drives the external EOM. The best error signal is produced when the carrier intensity transmitted from the FPI is reduced to 68% of it unmodulated value (see p. 49 in [Bur95]). The EOM is driven by a Mini-Circuits voltage-controlled oscillator (VCO, model # JTOS-25) set to 14 MHz which is amplified by a Motorola wideband RF linear amplifier (CA2832C) and stepped up with a coil. The VCO output was also routed to a phase shifter, JSPHS-26,

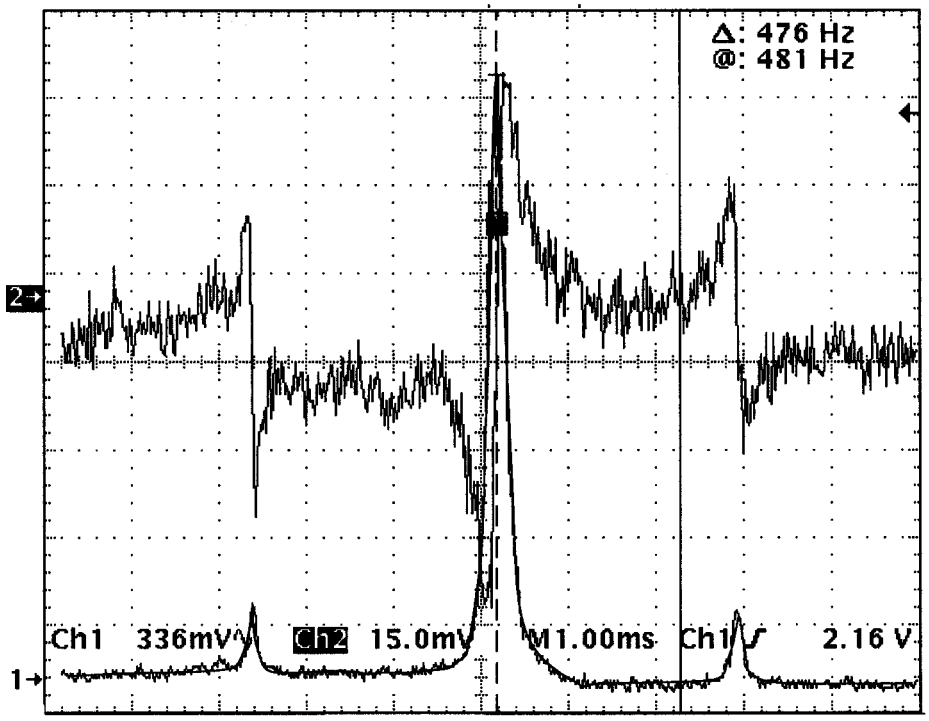

Figure 6.6: A screen shot of a digital oscilloscope of the FPI transmission signal and the fast error signal (output of the mixer) as the length of the FPI is scanned with the PZT. The FPI transmission trace has been highlighted in red, and the sidebands are at 14 MHz, the width of the cavity (FWHM) is 1 MHz.

also from Mini-Circuits.[4]

The external FPI cavity was built at the University of Washington, modeled after the Burleigh spectrum analyzer CFT-500. The body is made of stainless steel (the original Burleigh is made of Invar), and the length is adjustable around 50 cm. The original cavity was designed as a confocal cavity, however, we purchased mirrors with a 60 cm radius of curvature so that the cavity is no longer confocal. Confocal cavities with two curved mirrors that are separated at a distance at exactly equal to the radius of curvature are useful in that they are very easy to align and there is no need to mode-match. However, all of the longitudinal modes are nearly degenerate, and it is nearly impossible to keep the distance

[4]The working frequency range of JSPHS-26 is specified as 18–26 MHz for phase range of 180°, however it gives us enough range to produce a good error signal at 14 MHz.

between the mirrors at exactly the right distance, leading to the modes spreading out, ambiguous line-center, and broader width. We purchased the mirrors from CVI Optics (model # TLM1-550-0-0537-0.60cc) which has 99.7% reflectivity at 0° incidence and 60 cm radius of curvature. The front mirror is attached on a cylindrical PZT (EDO Electro-Ceramic Products EC65). The free-spectral range of this cavity is $FSR = c/2nl = 300\,\mathrm{MHz}$[5], where c is the speed of light, n is the refractive index of the space between the mirrors and l is the distance between the mirrors. The measured width is about 1.5 MHz, which means a finesse of 200. Finesse, F, can be calculated empirically from the reflectivity, and for two identical mirrors,

$$F = \frac{\pi R}{(1-R)^2} \tag{6.5}$$

where R is the reflectivity of the mirrors. For $R = 99.7\%$, $F = 520$, about a factor of 2.5 higher than the measured finesse. The cavity was wrapped with a heater tape and placed inside a polyethylene tube. A thermistor was placed in the center of the tube. We had a spectrum analyzer control box from Burleigh (model # RC-45) available to us. It has a temperature stabilization circuit built in which could keep the temperature stable to 0.01 °C. The heater tape and the thermistor were chosen to match the original design as well as possible, and connected to the box for temperature stabilization of the cavity.

The error signal is amplified by CLC 425 and splits into three paths. Two are used to drive the intracavity EOM: the first goes directly to one side of the intracavity EOM for to control the high bandwidth response, and second is amplified further (HV op-amp Apex PA41) for slower, HV response, and applied to the other side of the EOM which has a unity gain at about 1 MHz and a roll-off at several kHz. The third path goes to the "slow path transfer" circuit which smooths over the gain near the frequency crossover point between the EOM and the slower elements which come with the 899, i. e. the tweeter and the Brewster plate. The signal is then routed back on to the Coherent dye laser driver board 1A9 at resistor R17 as mentioned in Section 6.2.1 to drive the PZT and the galvanometer which control the tweeter and the Brewster plate. Sandberg has done an extensive analysis of the Coherent system and describes in detail the results and how this was done.

[5]You may at times see $FSR = c/4nl$. This is for confocal cavities where the resonance frequencies of the transverse modes either coincide or fall halfway between the longitudinal modes.

When designing a lock system, one has to balance between the performance and its robustness. A very narrow FPI cavity can produce an error signal with very steep slopes, but any disturbance that lies outside of its width can take the laser out of lock. On the other extreme, as the cavity is broadened, the extent of the error signal is also wider, and the slope of the error signal is small. The redundant lock is a compromise between these two extremes. A part of the error signal which goes back onto the 1A9 Coherent board to drive the tweeter and Brewster plate is also fed into the "External" control of the Coherent box. By setting the scan width on the control box to the correct gain (0.33 GHz in our case), the Coherent reference cavity is kept on resonance with the external FPI. A photodiode monitors the output from the FPI (Lock Det. in Figure 6.6). When this signal dips below a certain level, the electronics turns off the intracavity EOM and the laser is switched over to be locked to the Coherent reference cavity, using the original servo. When, usually in a very short time, another disturbance brings the external cavity into resonance, the lock switches back over to the servo system built here. This saves us from having to reacquire the lock, however, this process of switching over can kick atoms out of the MOT. Currently this occurs once every 5 s or so, and is the limiting factor in the lifetime of the green MOT.

We measured the performance of the short term lock by using a 30 cm spectrum analyzer (SA), from Melles Griot, in a confocal configuration. The PZT on the SA was deactivated to let it stabilize, the green laser narrowing was activated, and the frequency was tuned so that the transmission is at half-maximum of a resonance peak of the spectrum analyzer. Figure 6.7 shows the transmission from the spectrum analyzer as the laser is locked to the external FPI and scanned (plotted against the bottom axis), and as the scan was turned off to monitor the stability of the lock (plotted against the top axis). When the scan was turned off, the laser was tuned and "parked" at half-maximum, and the transmission from the spectrum analyzer was monitored and recorded as a function of time. The transmission peak is asymmetric because the SA was not exactly confocal, and the different modes are somewhat spread out. The width of the peak at the height where the laser was "parked" is 3.8 MHz. The FSR of this second cavity is 250 MHz (FSR of a confocal cavity is $FSR_{cf} = c/4nl$). The standard deviation of the "parked" signal gives a laser width of 40 kHz. The maximum deviation in this 50 ms time duration is only 170 kHz, which is primarily due to

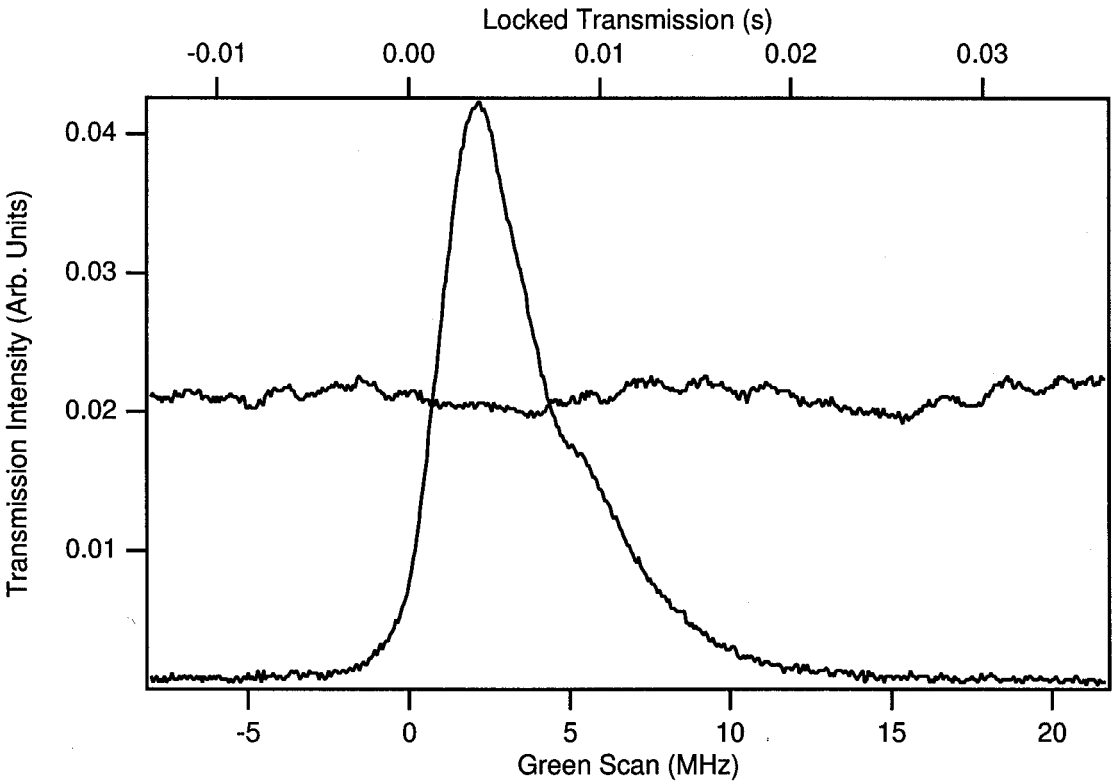

Figure 6.7: Summary of the performance of the short term lock. The transmission from the spectrum analyzer (SA) is shown against the bottom axis which was calibrated by another scan which scanned across one free-spectral range at the same scan rate. The transmission from the SA with the laser parked part way up the peak on the left-hand side is plotted against the time axis along the top of the figure.

the drift in the length of either the SA cavity or the FPI cavity, and is taken out by the long-term stabilization described in the next section.

Perhaps a more dramatic demonstration of the performance of the narrowed laser was evident when we looked at atomic fluorescence from the blue MOT. We trapped Yb atoms using the blue ($^1S_0$–$^1P_1$) transition and probed the atoms with 5 mm diameter green laser. The green fluorescence was collected while scanning the green laser in frequency. Figure 6.8 (a) shows such a scan with the narrowed green laser, where the external FPI cavity was scanned over 80 MHz, and (b) shows a scan with the dye laser locked only to the original Coherent reference cavity. The three peaks barely visible in (a) are the Zeeman sublevels

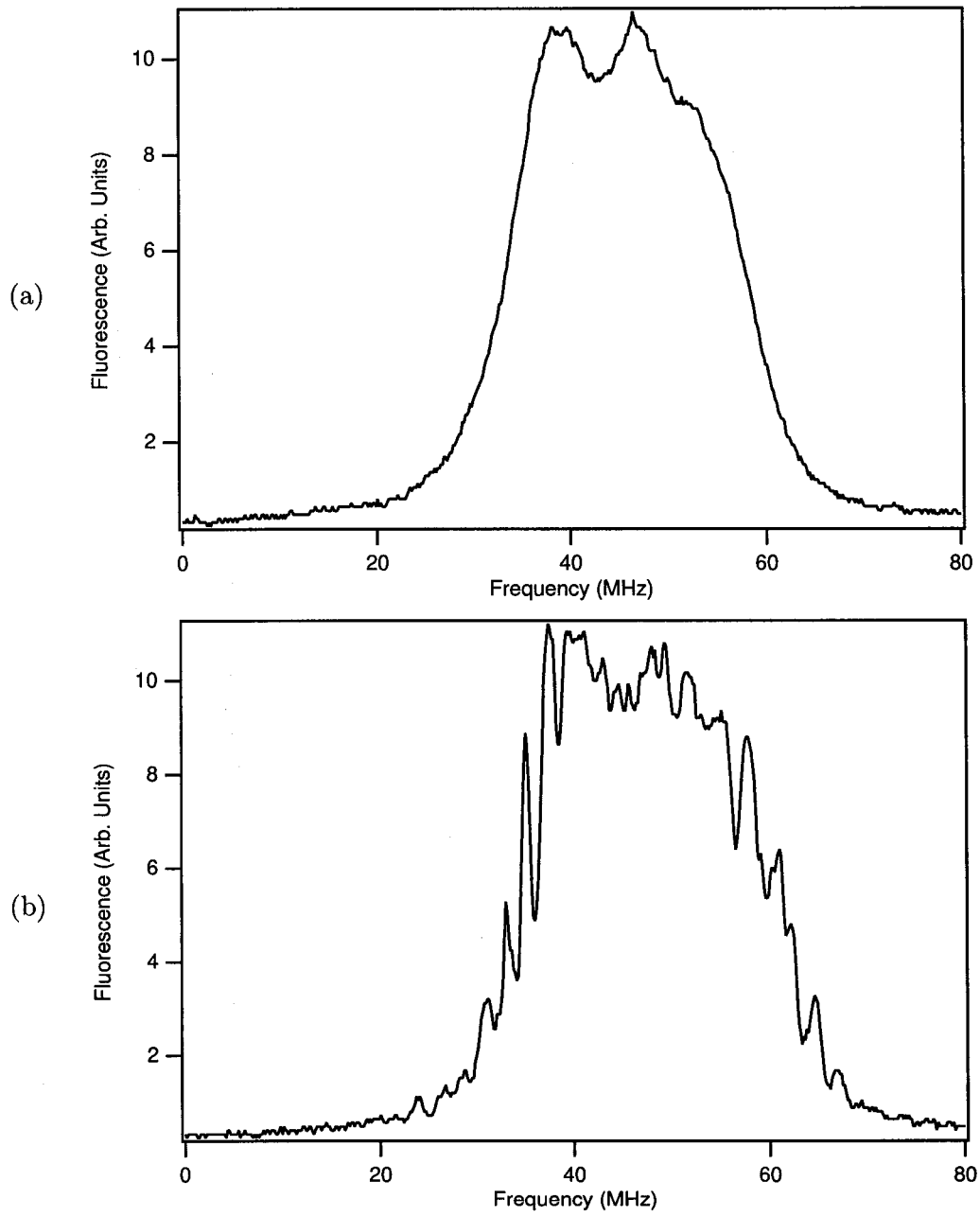

Figure 6.8: The fluorescence in green from Yb atoms trapped in blue MOT. The green laser is scanned roughly 80 MHz in frequency while (a) the dye laser was locked to an external cavity via Pound-Drever method and (b) the dye laser is locked only to the Coherent supplied reference cavity.

of the blue-trapped atoms which were slightly displaced from the center where the average magnetic field would be zero. The narrowed laser is much more stable in frequency than is observed in the narrowed laser. The fluctuations seen in (b) is probably more due to frequency fluctuations than laser power because the fluctuations near the peak is much smaller than those seen where the slope is steeper.

6.2.3 Long Term Stability: Atomic Beam Lock

The long term stability in the frequency of the green laser comes from locking the external FPI cavity to the desired transition of Yb. We use a portion of the Yb atomic beam, right after it comes out of the oven, before it enters the Zeeman slower (see Figure 5.3). The green laser and the Pound-Drever stabilization setup are on a second optical table due to space constraints, and the laser beam is transported via an optical fiber to the main optical table which has the blue laser and the MOT vacuum chamber. The output of the fiber is collimated by a microscope objective and goes through an AOM. We use the zeroth order for the long term stabilization as a frequency reference, and the first order goes toward the MOT. This allows us to turn off the laser beam going toward the MOT without turning off the frequency reference beam.

The reference beam intersects the atomic beam at 90°, and the fluorescence from the atoms is collected by a lens (diameter = 2 in.), located to collect light which goes in a direction orthogonal to both the atomic beam and the laser beam, and detected by a PMT. Although we have implemented spatial filtering of the light collected by the lens, some blue light from the Zeeman slower scatters off the collimator and is seen by the PMT. We have placed a color filter in front of the PMT to block out the blue light, but some still gets through. Using an atomic beam instead of a vapor cell for locking essentially gives us peaks which are much narrower, which in the case of the green transition are limited by the transverse velocity spread of the atomic beam. The blue transition is wider, and the Doppler width is narrower than the natural linewidth. In our beam, we have measured a width of 10 MHz, consistent with the 0.9° spread of the atomic beam as described in Section 5.1.2.

It was important to retro-reflect the laser beam back onto itself to avoid it from steering

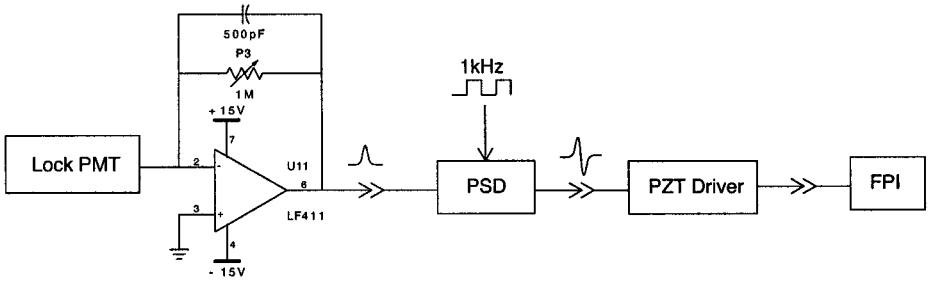

Figure 6.9: The Zeeman-modulated fluorescence is detected by a PMT. After the photocurrent is converted to voltage and amplified, the signal is demodulated by a lock-in amplifier (phase-sensitive detector, or PSD) to produce the error signal. The signal is then amplified by a PZT driver, and fed back to the PZT which controls the length of the stabilization FPI.

the atomic beam (this effect was more exaggerated when we tried this scheme with the blue laser since this is a much stronger transition and the blue laser can apply a much stronger force on the atoms). The laser polarization is turned into σ^- with a quarter waveplate to select the $m_g \rightarrow m_e = m_g - 1$ Zeeman transition, and a pair of Helmholtz coils supply a magnetic field parallel to the laser beam propagation to provide a Zeeman shift as an offset for the laser lock frequency reference. The coils provide 39 gauss per 1 A of current and for the $^1S_0$–$^3P_1$ transition this translates to 8 MHz per 0.1 A of current.

The error signal is generated by modulating the magnetic field at 1 kHz (250 mA modulation on top of DC current), and the overall offset is tuned by changing the DC offset to the magnetic field. The fluorescence from the atomic beam is collected with a PMT, and the amplified signal is sent into a lock-in detector. A glass color filter (Coherent GG495, 36-9439) was inserted in front of the PMT to block the blue Zeeman slower laser which scattered off the atomic beam collimator. The PMT signal is demodulated by a lock-in amplifier (EG&G model # 128A 0.5 Hz – 100 KHz), integrated, and fed to the external control of the PZT that controls the length of the external FPI cavity. The analysis of the error signal excursion while the laser is locked indicates that the lock can hold the cavity to within 50 kHz. The general layout of the electronics is sketched in Figure 6.9.

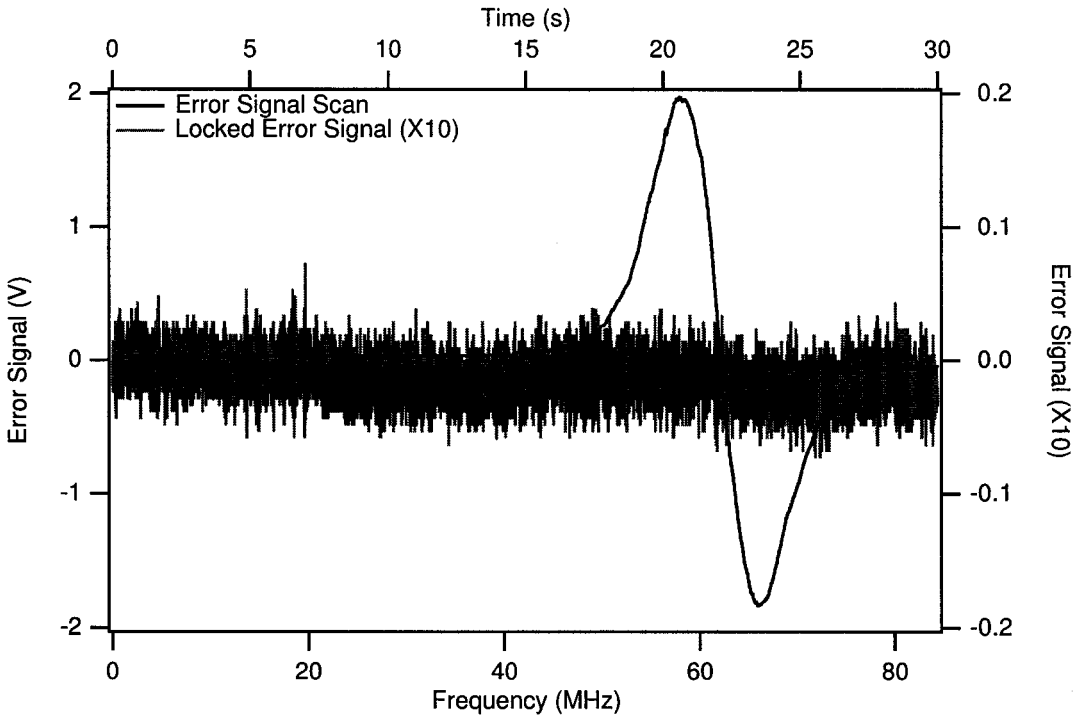

Figure 6.10: The error signal for the longer-term green laser frequency stabilization. The dark black line, plotted against the left and bottom axes, is the error signal as the laser is swept in frequency across the ^{174}Yb $^1S_0$–$^3P_1$ resonance at 90° to the atomic beam. The gray line is the error signal as the laser was locked to this signal, and is shown plotted against the right and top axes. The vertical scale of the locked signal is ten times that of the scanned signal.

The performance of the long term stability was measured by monitoring the error signal output from the EG&G lock-in amplifier. The black line in Figure 6.10, plotted against the left and bottom axes, shows the error signal when the laser is swept across the ^{174}Yb resonance. The peak is 10 MHz wide. The gray line in Figure 6.10 which is plotted against the right and top axes shows the error signal over 30 s while the lock was engaged (the right axis scale is ten times the left axis). The lock-in detector was set to have 10 mV sensitivity and 0.1 s of integration time with no post-integration filter. The RMS noise in this bandwidth corresponds to 20 kHz noise in laser frequency.

Chapter 7

BLUE MAGNETO-OPTICAL TRAP

The blue transition ($^1S_0$–$^1P_1$) is used for initial cooling and trapping. It is a very strong line and can be used to rapidly cool the atoms. As described in Section 3.2, a Zeeman slower using this line is much shorter than those used for alkali atoms, and the trap loading efficiency can be higher. Much of the initial work was done using this transition to try to get temperatures as low as possible and to get as many atoms as possible. The goal was to cool the atoms enough to load a FORT (far-off resonance trap) directly from the blue MOT. Our estimates indicated that it would be feasible to load a dipole trap with an Ar^+ laser if the temperature was less than 2 mK. We were only able to reach 4 mK with the blue MOT, and possible reasons for this will be discussed in Section 7.3.3.

When we started the project, we were uncertain as to how effective the blue Zeeman slower and the blue MOT would be. There was some ambiguity as to what the branching ratio of the $^1P_1$ to the D-states is and whether a repumping beam would be necessary to get the atoms out of the $^3P_0$ and $^3P_2$ states which are metastable (see Figure 4.4). Theories predicted a range of lower limit for the branching ratio between the decay of the 6s6p $^1P_1$ state to the ground state and the decay to all other states: 1×10^7 in one model and 6×10^5 in another [Mig91]. Experimental work on a Yb MOT in Kyoto in 1999 determined the upper limit on the ratio to be 8.3×10^6 [Hon99]. The branching ratio limits the lifetime of the blue MOT, though no repumping laser is necessary.

I will first describe the overall setup of the Zeeman slower and blue MOT in Section 7.1. The Zeeman slower and its performance are discussed in Section 7.2. The following Section 7.3 describes the blue MOT and its performance, loading efficiency, lifetime, and temperature measurement.

7.1 Overall Layout of Blue Laser and Optics

Figure 7.1 shows the overall layout of the lasers and optics for the blue MOT. Section 6.1 describes the details of the laser at 399 nm. The output of the laser is split 50/50 by a non-polarizing beam splitter cube, one half going toward the MOT, the other going to the Zeeman slower. The Zeeman slower half goes through an AOM in a double-pass configuration which can shift the laser by −270 MHz to −330 MHz. The efficiency of the double-pass AOM in shifting the laser is about 25%. The Zeeman slower beam goes through a quarter waveplate and is raised 12" off the table by a periscope to be level with the atomic beam. The beam diameter is about 10 mm when it enters the vacuum chamber through the end window, and is focused at the Yb beam collimator near the Yb oven.

The MOT beam goes through a couple of beam shaping lenses, then gets divided again by a non-polarizing beam splitter cube. 50% goes toward the vertical MOT beam, and the other 50% goes toward the horizontal MOT beams, which are raised 12" above the table by another pair of periscope mirrors. We have installed two optical bread boards at a height of 9" above the table, one in front of the MOT, and another in the back for more flexibility in the layout and mechanical rigidity of the optics. The horizontal beam is divided again into two. Each of the three beams for the MOT, one vertical and two horizontal, go through a quarter waveplate (zero-order for 399 nm), into the vacuum chamber through their respective anti-reflection coated viewports, out through another set of viewports, through another set of quarter waveplates and retro-reflected. The MOT laser beams are about 10 mm in diameter at the first viewport, and to compensate for losses in the mirrors, they are slightly focused down to be roughly 7 mm when they come back to the same viewport. This ensures that the laser intensity in the two directions is roughly the same to compensate for the losses in the windows, waveplates, and absorption by the trapped atoms.

The fluorescence from the atoms is collected by a lens at the back viewport and detected by either a PMT or a CCD camera. A flip up mirror directs the light to either the PMT or the CCD camera. A small part of the MOT beam is split off before the chopper to serve as a probe beam. The probe beam enters the vacuum chamber upward from the bottom window. One of the steering mirrors is mounted on a translation stage so that we can translate the

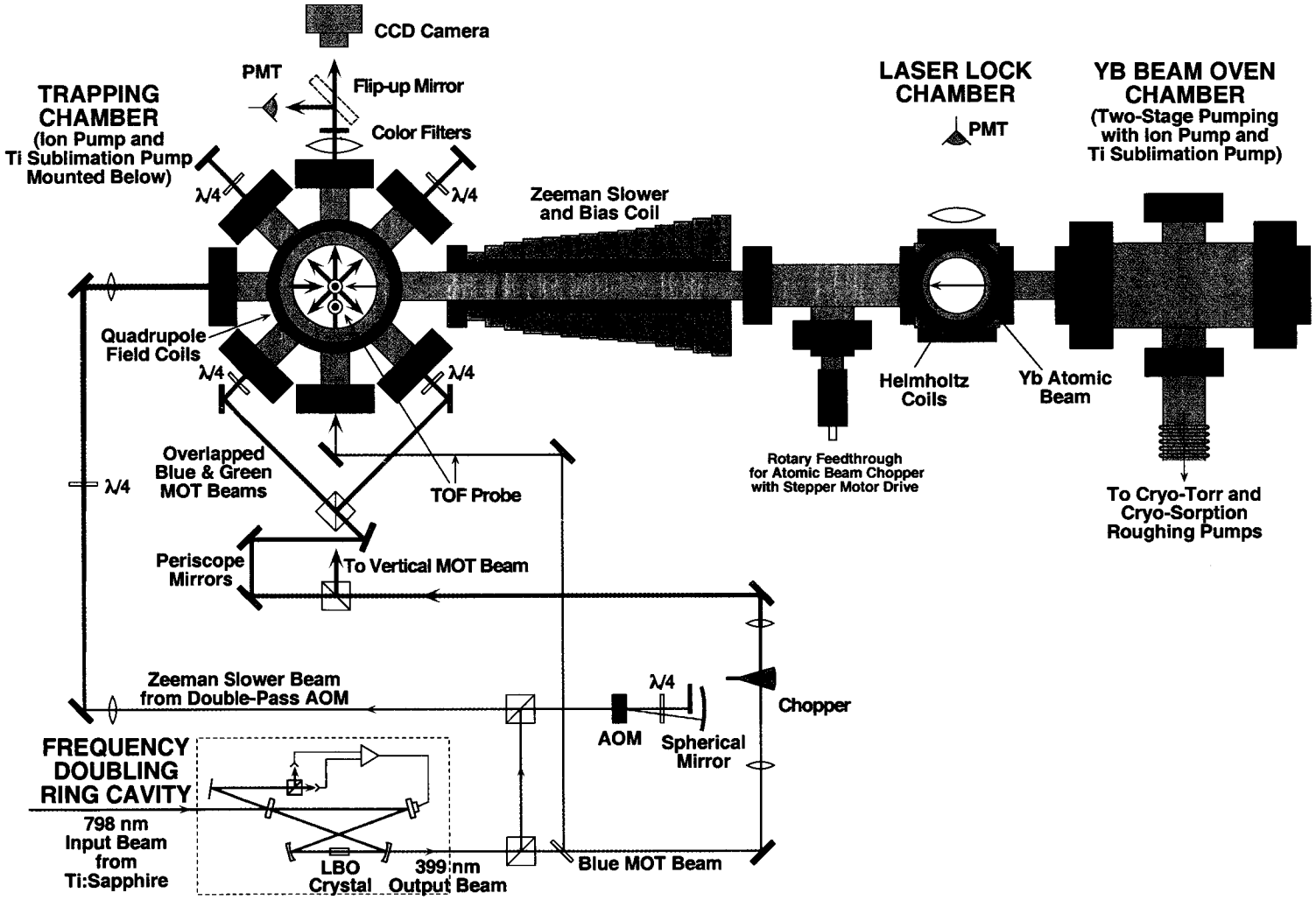

Figure 7.1: Schematic for the blue MOT setup.

probe beam. The atomic beam can be turned on and off with a mechanical chopper made of an aluminum cylinder. It is connected to a rotary motion feedthrough controlled by a stepper-motor. The cylinder has two holes drilled in the shaft perpendicular to each other and to the shaft for a total of four on/off cycles per rotation. The atomic beam is on when one of the holes is horizontal and is aligned with the beam. There is a disk mounted to the shaft on the outside of the vacuum chamber with four holes which are aligned with the atomic beam chopper to monitor the rotation. The phase of the rotation is detected by monitoring when the light from an LED reaches the photodiode which is mounted on the other side of the disk.

7.2 The Zeeman Slower

The Zeeman slower consists of a spatially varying magnetic field and a laser beam which is counter-propagating with the atomic beam. The laser beam is 1 cm in diameter at the end window opposite the Yb oven and focused at the atomic beam collimator to match the spread in the Yb beam. The mechanical dimensions of the Zeeman slower were discussed in Section 5.2. The magnetic field is set up such that its magnitude decreases as the atoms travel down the beam. An additional coil provides an overall bias so that the atoms exiting the Zeeman slower fall out of resonance with the Zeeman slower laser beam. The field gradient is set up so that with 4 A of current running in the coils, the Zeeman slower can slow atoms which are going slower than 300 m/s, the mean speed of Yb atoms in the beam at 400 °C. The bias field produces 250 G with 4 A of current running in the coils, which offsets the resonance by 350 MHz. The operating current may vary depending on the application. The Zeeman slower magnetic field gradient was set up for constant deceleration of the atoms, and with 4 A of current through the coils, the field varies by 540 G in 30 cm.

To measure the speed of the atoms in the atomic beam, one of the horizontal MOT laser beams that intersects the atomic beam at an angle of 45° (single pass) was used. A probe which is perpendicular to the atomic beam does not contain information about the longitudinal velocity along the atomic beam, only the transverse. A probe at 45° to the atomic beam can detect the Doppler shift, and by comparing the frequency to the peaks

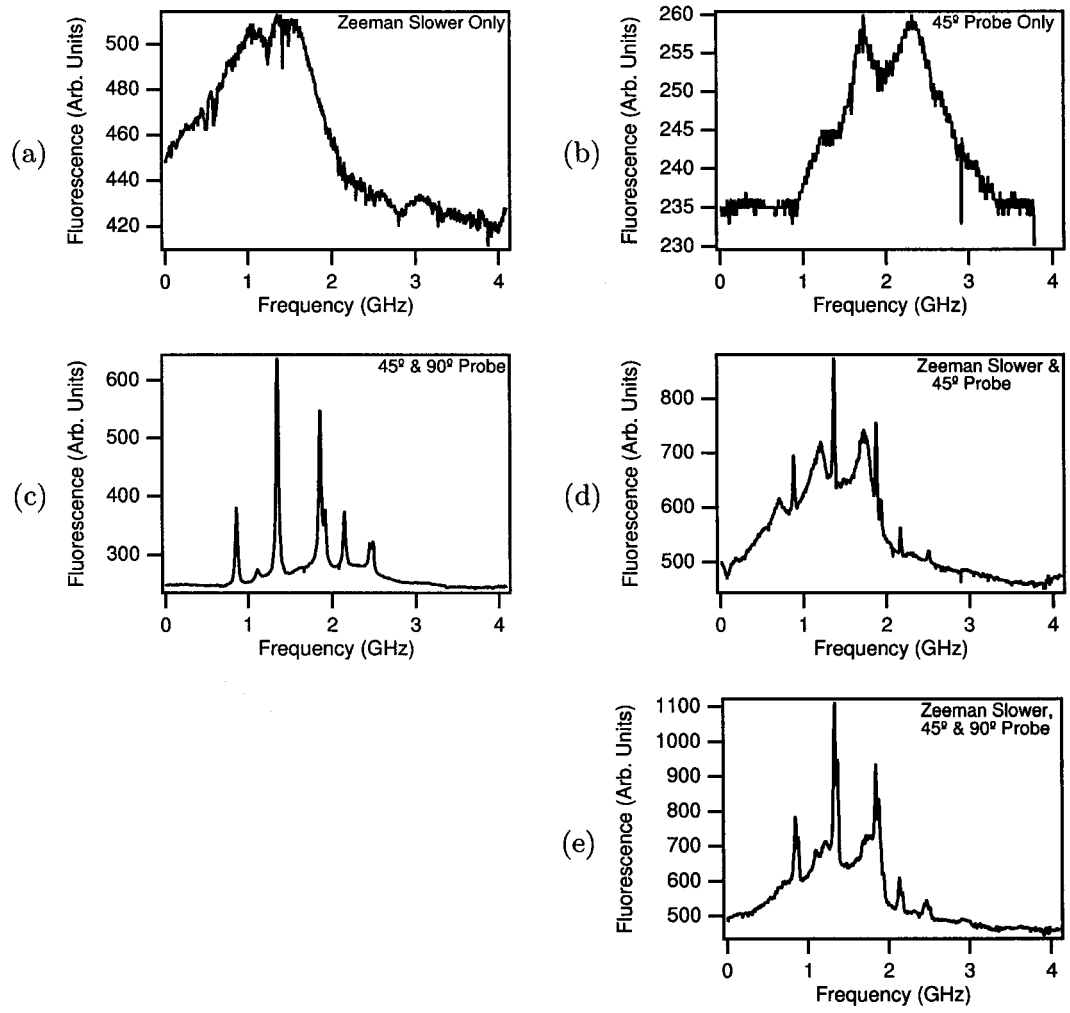

Figure 7.2: The fluorescence from the MOT region as the laser frequency is scanned. (a) shows the fluorescence from the Zeeman slower, no probes. (b) has only the 45° probe, (c) is the probe beams at 45° and 90° and no Zeeman slower. (d) shows the fluorescence from the Zeeman slower and the 45° probe, and (e) has all three. In this particular figure, there is a 55 MHz Doppler shift between the 90° and the 45° probes, corresponding to an atomic beam velocity of 30 m/s. Note that the vertical scale and gain are not kept constant.

detected from a probe beam at 90° (the vertical MOT beam), we can calculate the velocity of the atoms,

$$v_a = c(\nu_s/\nu_t)/\cos(45°) \tag{7.1}$$

where ν_s is the difference in the frequencies between the 90° and 45° probes, $\nu_t = c/\lambda = 7.5 \times 10^{14}$ Hz is the ${}^1S_0$–${}^1P_1$ transition frequency, and c is the speed of light. Figure 7.2 shows the fluorescence detected from the MOT region when the laser frequency was scanned over 4 GHz. The Yb oven was at 400 °C (mean velocity, $\overline{v} = 300$ m/s). The Zeeman slower was shifted by −280 MHz with an AOM, 3.9 A of current in the Zeeman slower, and −2 A in the bias field. The laser was scanned by feeding a DAC signal from the computer into the external control input of the Coherent 899 Ti:sapphire laser. Figure 7.2 (a) shows the fluorescence from Zeeman slower and no probes, (b) shows just the 45° probe, (c) shows the two probes at 90° and 45°, (d) shows the Zeeman slower and the 45° probe, and (e) shows the scan when all three, Zeeman slower and both probes, are on. The atoms are cooled by the Zeeman slower to a narrow range of velocity. The 45° probe sees atoms that are Doppler shifted by $v_D = \nu_t(v/c)\cos(45°)$. In Figure 7.2, the shift between the two probe resonances is 55 MHz, corresponding to an atom velocity of 30 m/s. Roughly 10% of the atoms below $\overline{v}$ are slowed.

In general, when the laser power for the Zeeman slower was low, the magnetic field gradient also had to be turned down for optimal loading of the MOT. The bias could be operated somewhat independently of the Zeeman field as long as the Zeeman AOM was adjusted accordingly. For 5 mW in the Zeeman slower, the optimal current in the Zeeman slower is roughly 2.5 A.

7.3 The Blue MOT

The Yb MOT behaves in many ways differently than alkali atom traps. Because the even isotopes of Yb and group II atoms have only one level in the ground state, sub-Doppler cooling is absent. This results in a few differences in the behavior of the MOT. First, the temperature is higher: the lowest temperature we saw was 4 mK, roughly five times the Doppler limit of 690 μK. It seems to be more sensitive to alignment and imbalances in the

counter-propagating laser beams than the alkali traps. To get the lowest temperature, it is necessary to align the beams very carefully, and the center location of the trapped atoms could easily be moved simply by aligning the laser beams differently. The temperature is also strongly dependent on the focusing of the MOT laser beams.

The daily alignment of the MOT is as follows: The starting point for MOT loading is the Zeeman slower. We optimize the Zeeman slower laser alignment and magnetic fields using the method described in Section 7.2. The MOT laser beams are aligned with the middle of the viewports of the vacuum chamber, and the retro-reflected beams are aligned to come back on themselves (a piece of paper with a hole cut out is useful for this). The isotope and hyperfine resonances are found by scanning the Ti:sapphire laser across 2 GHz (4 GHz at 399 nm) while monitoring the fluorescence with a PMT: a broad peak comes from the Doppler broadened Zeeman slower and the two horizontal MOT beams, and sharper peaks comes from the vertical MOT beams. At this point, a small MOT can be seen by zooming in on one of the peaks of the vertical MOT beam and sweeping the Ti:sapphire laser over 40 MHz (80 MHz at 399 nm). The signal on the PMT appears as a small asymmetric peak slightly to the red in frequency of the vertical resonance. Once this signal is detected, the MOT beams alignment and current settings for the magnetic fields are adjusted to maximize it.

The signal from the MOT is much larger and sharper in frequency than the signal from the vertical beams, as can be seen in Figure 7.3. It shows the fluorescence detected by the MOT PMT as the 399 nm laser is scanned over 4 GHz with a 2 GHz scan of the Ti:sapphire laser. Both the MOT and the Zeeman slower laser beams are scanned in frequency for this figure. The solid line shows the fluorescence from the MOT, and the dotted line shows the fluorescence from the vertical beams only. The vertical beam data was taken with a PMT sensitivity which is 56 times that at which the MOT fluorescence was taken. The frequency range at which the the atoms are trapped when both the Zeeman slower and the MOT are scanned is much narrower than the natural linewidth of Yb of 28 MHz.

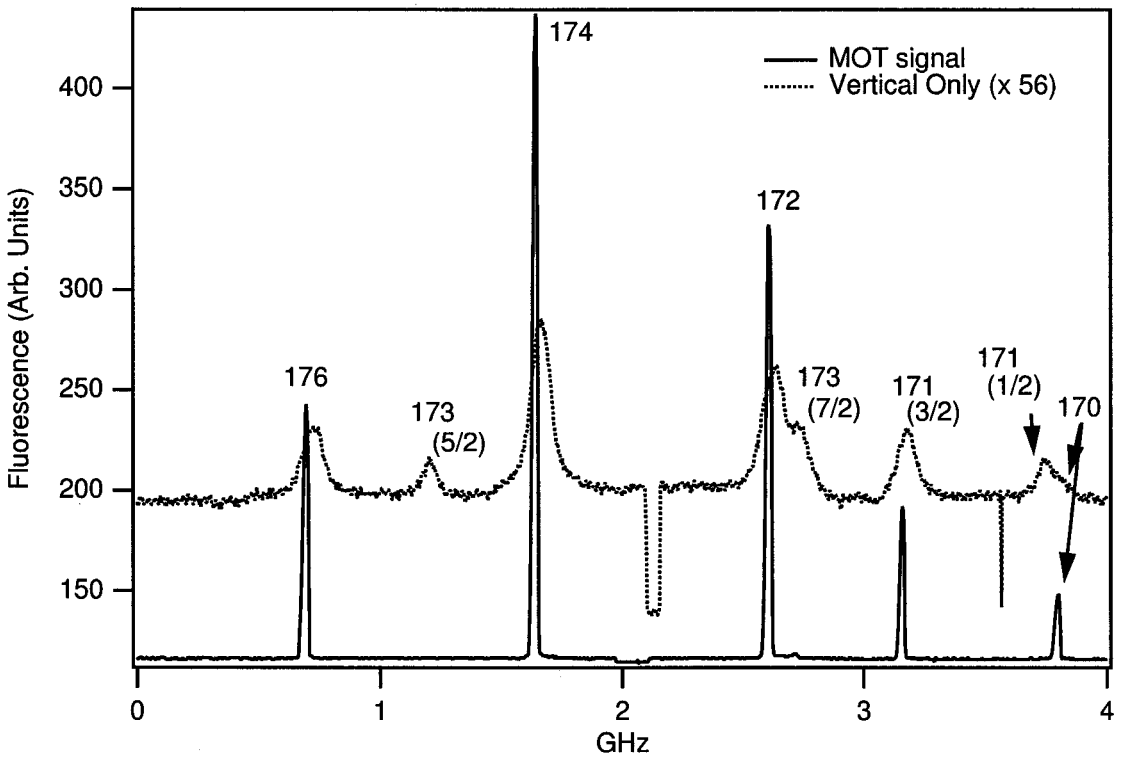

Figure 7.3: The fluorescence from the MOT region as the 399 nm laser is scanned over 4 GHz. The solid line is the fluorescence from the MOT and the dotted line is the fluorescence from the vertical beams only. The high voltage was at 300 V for the MOT scan, and 500 V for the vertical beam scan, which makes the gain 56 times higher for the vertical beam scan. These particular scans are not wide enough to see isotope ^{168}Yb.

7.3.1 Blue MOT Number and Isotopes, Number Density Distribution

For a well-aligned trap and sufficiently small number of trapped atoms, the number density distribution is Gaussian, as expected from a damped harmonic potential. The size of a cloud is determined by the temperature of the atoms,

$$k_B T = M v_{rms}^2 = \kappa \sigma_{rms}^2 \tag{7.2}$$

where κ is the spring constant of the harmonic trap determined by the magnetic field gradient and optical transition rate (see Section 3.3), and σ_{rms} is the rms-width of the cloud which has a Gaussian distribution. The spring constant, κ, in the x-direction derived from

the simple two-level MOT model is given by Equation 3.18. Because the quadrupole magnetic field and laser intensity are both twice as strong in the vertical than in the horizontal direction in our trap, the trap is not spherical, but flattened vertically. In the low density regime, the size stays constant as more atoms are loaded into the trap. For a larger number of atoms where the optical density is much greater than one, radiation trapping occurs, where photons emitted by atoms in the trap are re-absorbed by other atoms in the trap. This leads to an increase in the size while the density remains constant [Wal90]. For alkali atoms, radiation trapping starts to have an effect on the density and atom distribution at a number of $N \gtrsim 10^5$ atoms. In alkaline-earth atoms and Yb, the lack of sub-Doppler cooling leads to a higher temperature and larger trap volume. For a trap which is a few mK, the trap size is roughly 1 mm in the horizontal direction, and we do not expect radiation trapping to start occurring until the number of atoms exceeds 10^7, with a density greater than $10^{10}\,\mathrm{cm}^{-3}$.

For slightly misaligned trap beams, a coordinate-dependent vortex force (CDVF) is introduced and it is possible to achieve different spatial distributions including a ball, ring, and ring with a central core [Wal90, Ses91, Bag93, Gue94]. It was shown that the ring size is dependent on the degree of misalignment of the trap beams. We have observed a ring and a ball, but not a ring with a central core. The size of the ring could easily be changed by changing the misalignment of the mirrors. In the papers mentioned above, misalignment in the horizontal beams is discussed. We were able to see a ring which has a vertical component as seen in Figure 7.4 (a) which was taken with a CCD camera in the horizontal plane as shown in the schematic in Figure 7.1. Figure 7.4 (b), (c), and (d) show the trapped clouds in Gaussian distribution with slightly different alignments. The irregular shape comes from fringes introduced by optics and windows.

The location of the atom cloud trapped in the blue MOT is very sensitive to the trap beam alignment. The MOT magnetic field gradient used for most of the time is 30 G/cm. This was produced by 6 A of current in the MOT coils: the maximum current of the power supply used. We ran the field gradient with the current as high as 10 A with a different power supply, but did not see a noticeable change in the number of atoms in the MOT. However, there was some evidence that the overall positioning is less sensitive to trap beam

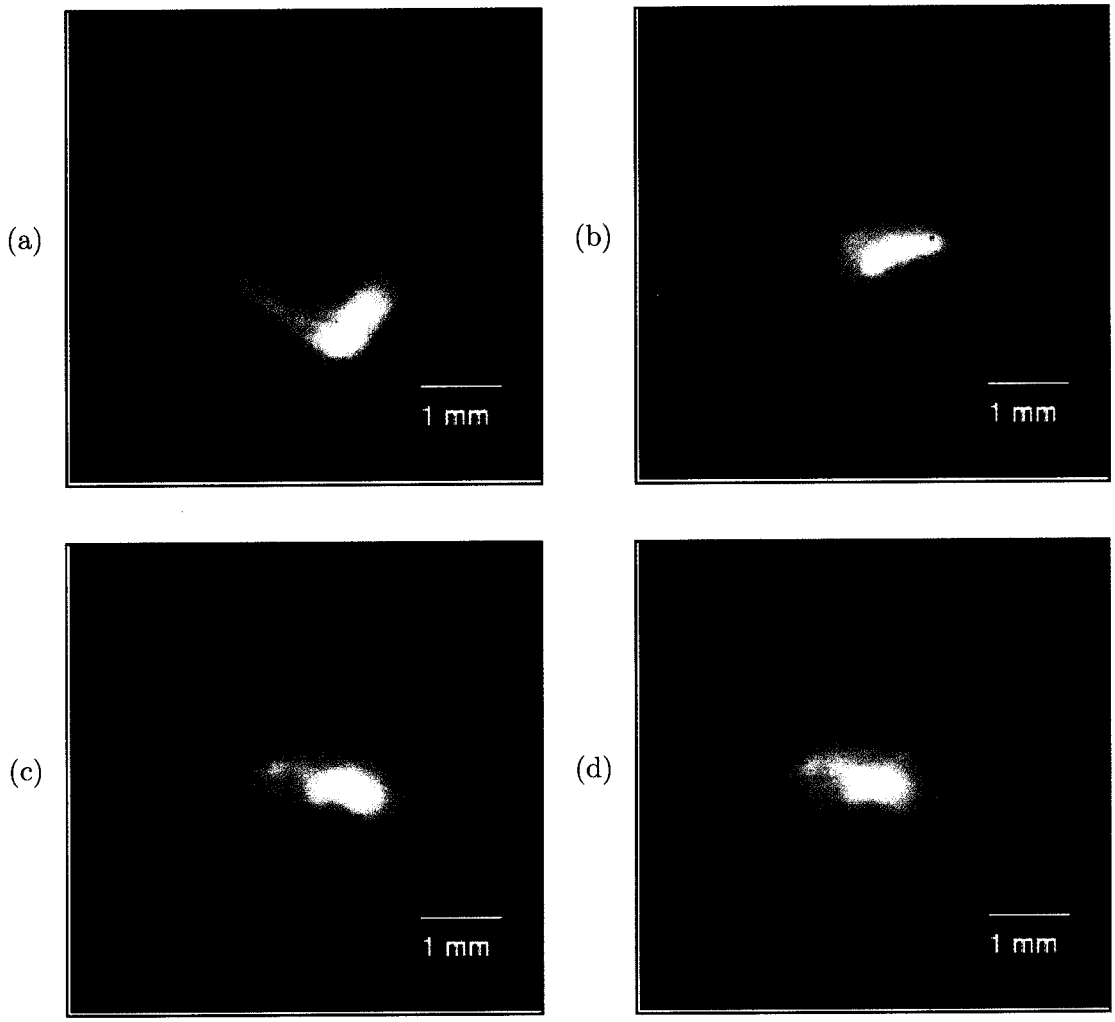

Figure 7.4: Fluorescent images of atoms trapped by the blue MOT taken in the horizontal plane at different alignment of the trap beams. (a) shows a ring distribution, (b) is a very well aligned trap, (c) and (d) are not as well aligned and larger.

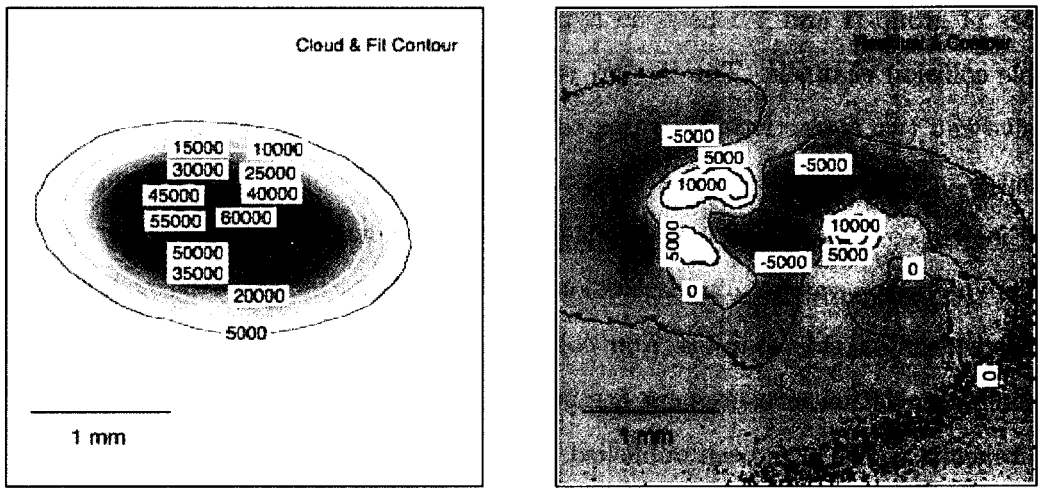

Figure 7.5: Contours of the fit of Figure 7.4(b) to a two-dimensional Gaussian shape and its residual of an atom cloud in a blue MOT.

alignment with a higher magnetic-field gradient. Ref. [Din99] mentions a magnetic field gradient of 70 G/cm for a Sr MOT.

7.3.2 Blue MOT Lifetime

Atoms can leave the trap through a number of mechanisms. This includes collisions with the background gas atoms, decays from the upper-state into a metastable state, or collisions among Yb atoms. When the trapped atoms collide with background gases, enough momentum may be transferred to the Yb atoms to overcome the trap potential, leading to trap loss. The branching ratio into the D-states will take the atoms out of the cooling cycle, and out of the trap. Laser-induced collisions also cause trap loss. At low temperatures, atoms can undergo a long-range R^{-3} dipole-dipole interaction when one of the atoms is excited. Once this excited "molecule" forms, there are two ways that they can be kicked out of the trap: radiative escape and fine-structure changing collision.

Much work has been done on the subject of trap-loss in alkali-metals, both experimental [Wal92, Mar93, Let95, Gen98, Pet94] and theoretical [Jul93, Jul93]. In these studies, the existence of hyperfine structure has made quantitative verification difficult. The even

isotopes of group-II and Yb have no hyperfine structure, vastly reducing the number of possible collision channels. The $^1S_0$–$^1P_1$ transition has only four molecular potentials, two repulsive and two attractive. Trap loss collisions come from the two attractive potentials. The surge of interest in cold and ultra-cold collisions is related to the recent success of Bose-Einstein condensates for which it is essential to know the scattering lengths.

There ha been a number of recent theoretical studies [Mac99, Mac01, Tie02, Mac02], and on the experimental side, trap-loss from cold collisions has been studied in strontium [Din99], and photo-association measurement has been done in cold calcium atoms [Zin00]. Lifetime measurements on Yb have been published by the Mossberg group in Oregon [Lof00b]. They measured the power-dependent loss from the blue MOT, but saw no decays which were due to atoms collisions, that is, they detected no number or density dependent decay.

The number density of atoms in the trap is described by the rate equation,

$$\dot{n} = L_n - \Gamma n - \beta n^2 \tag{7.3}$$

where n is the number of atoms in the trap, L_n is the loading rate, Γ is the linear loss rate due to the branching ratio and collisions with background gas, and β is the coefficient for density dependent loss coming from two-body collisions. When considering the total number of atoms in a trap, one must integrate over the volume of the trap. The number of Yb atoms in our trap is low enough that the density distribution is still in the constant volume regime, and occupy a Gaussian distribution. When integrated, Equation 7.3 becomes

$$\dot{N} = L_N - \Gamma N - \beta' N^2 \tag{7.4}$$

where $\beta' = \beta(\sqrt{2\pi}a)^{-3}$[Din99]. The solution to this equation is

$$N = N_{ss}\left(\frac{1 - e^{-\gamma t}}{1 + \xi' e^{-\gamma t}}\right) \tag{7.5}$$

where N_{ss} is the steady-state number, $\gamma = \Gamma + 2\beta' N_{ss}$ is the loss rate and $\xi = \beta n_0/(\beta n_0 + 2\sqrt{2}\Gamma)$ is the collision loss fraction. Here, n_0 is the peak density of the trapped atom cloud, where the atoms are distributed by $n = n_0 e^{-(r/a)^2}$. In the absence of β', the rate of loading and decay from MOTs are exponential.

The blue MOT lifetime is limited mainly by the branching ratio of the rate at which the Yb atoms in the $^1P_1$ state decay to the $^1S_0$ state to the rate they decay to the D-states (see

Figure 4.4). From the D-states, the atoms can decay to the triplet P-states, $^3P_{2,1,0}$. The $^3P_2$ and $^3P_2$ states are metastable, and if the atoms end up in these states, they become invisible to the trapping lasers and they are no longer trapped. This process limits the lifetime of the blue MOT.

The lifetime of the blue MOT was measured by monitoring the decay in the fluorescence from the MOT as the Zeeman slower AOM was turned on and off. Everything else, including the MOT lasers, atomic beam, and magnetic field gradient were left on. Without the Zeeman slower, the loading of the MOT was negligible and undetectable at the PMT sensitivity being used. As the Zeeman slower is turned off, loading of the trap is stopped, and the number of atoms in the trap decay, primarily due to the branching ratio. We made a cursory search for a non-exponential decay behavior. A typical decay seen in our trap is shown in Figure 7.6. The Zeeman slower and the trap was loaded for roughly 2 s, then turned off for about 3 s. Figure 7.6(a) shows an exponential fit to the curve and (b) shows a fit to Equation 7.5. Although there was some non-exponential component to the decay, we did not detect any systematic density dependence. The total laser power (sum of all MOT beams) is between 10 mW to 50 mW, detuning Δ of -2 MHz and -20 MHz. The number of atoms of between 10^4 to 10^6 was investigated. With the trap size of roughly 2 mm, the density studied was between $10^6\,\mathrm{cm}^{-3}$ to $10^8\,\mathrm{cm}^{-3}$. In the paper on cold-collisions in Sr, number densities ranging from $1 \times 10^9\,\mathrm{cm}^{-3}$ to $25 \times 10^9\,\mathrm{cm}^{-3}$ were studied [Din99]. It may have been that our number density was too low and the trap lifetime too short to get appreciable Yb–Yb interaction. To increase the density, we will need to load more atoms, and increase the magnetic field gradient to get a smaller trap volume.

7.3.3 Blue MOT Temperature

We measured the temperature of the blue MOT by a time-of-flight method, The velocity distribution of the atoms in the trap is determined by monitoring the fluorescence of the atoms as they pass through a probe beam after the atoms are released from the MOT.

The probe region was displaced horizontally from the MOT, directly on the other side of the MOT from the PMT and the camera, and introduced into the vacuum chamber

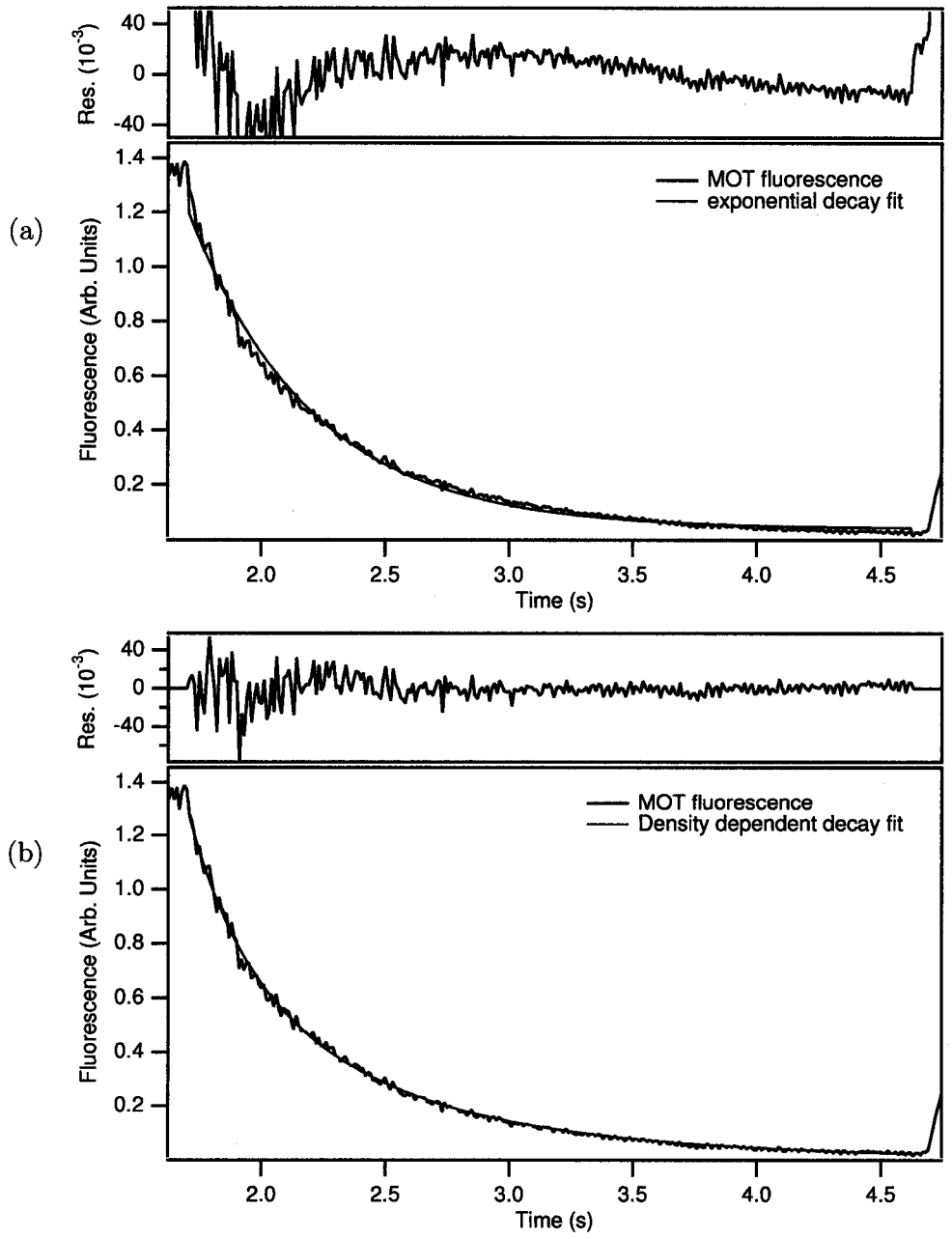

Figure 7.6: Decay of the number of trapped atoms with time. The fluorescence from the MOT region is monitored as the Zeeman slower is chopped. (a) shows a fit and its residual to an exponential curve, (b) shows a fit to Equation 7.5.

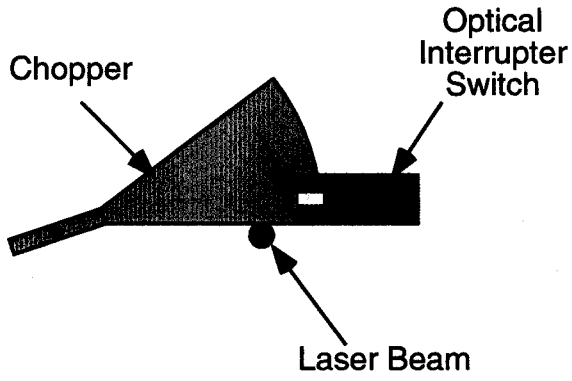

Figure 7.7: Blue MOT chopper and trigger for TOF measurement.

from the bottom window. One of the mirrors steering the probe beam was on a translation stage so that we could displace the beam perpendicular to its own axis by a distance of 5–10 mm. To figure out its distance from the MOT center, the probe beam was moved onto the MOT while monitoring the MOT with a simple CCD camera. The center of the MOT was determined as the center of the travel of the translation stage where the MOT was disturbed by the probe. Then the translation stage was moved by a known amount, and from simple geometry, the distance of the probe from the MOT was determined.

The MOT was turned off by turning off the MOT laser beams. The quadrupole magnetic field was left on, and the Zeeman slower AOM was turned off to avoid the Zeeman slower pushing the atoms as they left the MOT. We found that it was important to turn off the MOT laser beams quickly. A simple mechanical chopper was too slow and the uneven spatial profile of the laser beam as the chopper went across the beam had the tendency to heat up the atoms even when the chopper was placed at a tight focus of the laser.

We took advantage of the fact that we are using an external enhancement cavity for frequency doubling of the laser. By knocking out the lock of the external cavity, the MOT beam could be turned off within 5 μs. this was accomplished with an optical interrupter switch. A mechanical chopper driven by a stepper-motor that rotates the chopper at between 1 Hz and 3 Hz. We installed a photodarlington optical interrupter switch slightly above and

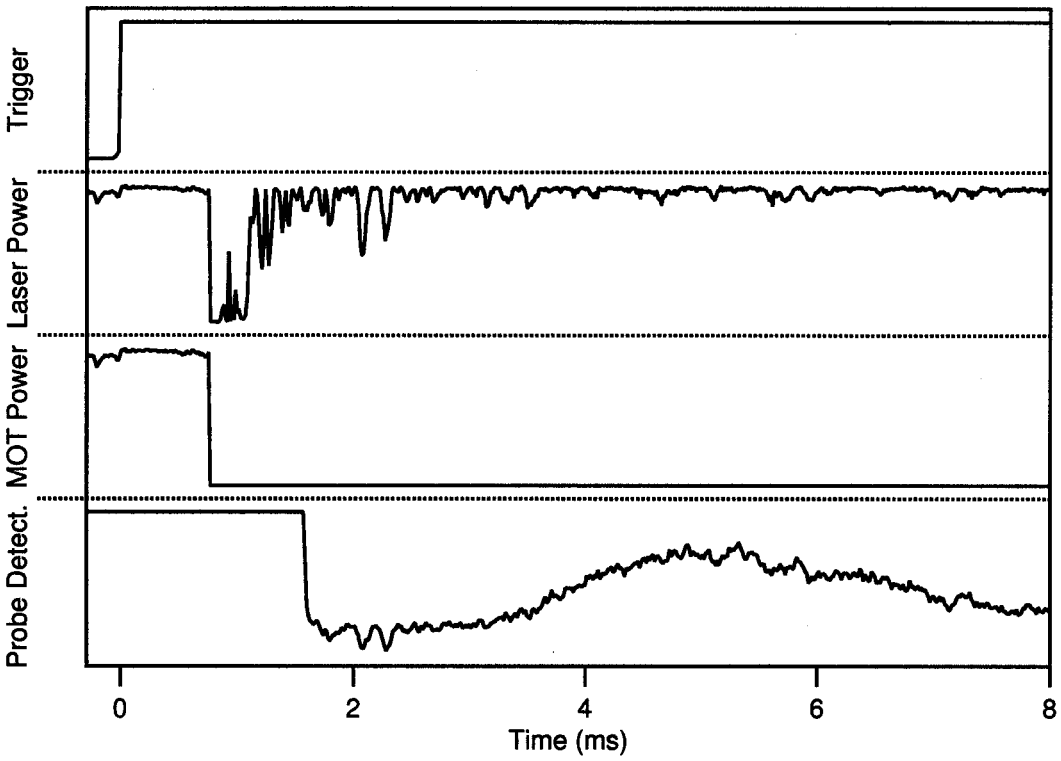

Figure 7.8: The time sequence for TOF temperature measurements of the blue trap.

to the side of the tightly focused MOT laser beam such that the chopper triggers the switch about 1 ms before the chopper reaches the laser beam (see Figure 7.7).

The switch, when triggered, sends a signal to a pulse generator, which sends a pulse to the error signal in the locking electronics of the doubling cavity. The doubling cavity gets knocked out of resonance temporarily, until it recovers after 0.5–1 ms. This time sequence is shown in Figure 7.8. The height of the optical switch is adjusted such that the chopper intercepts the laser beam during the 0.5–1 ms that the doubling cavity lock is knocked out. Meanwhile, the probe beam, which is not blocked by the mechanical chopper recovers when the doubling cavity lock recovers, and is ready to monitor the atoms that are expanding from the MOT region. The PMT sensitivity was turned up for this process, and is completely saturated while the MOT is still on. It takes about 1 ms for the current in the PMT to

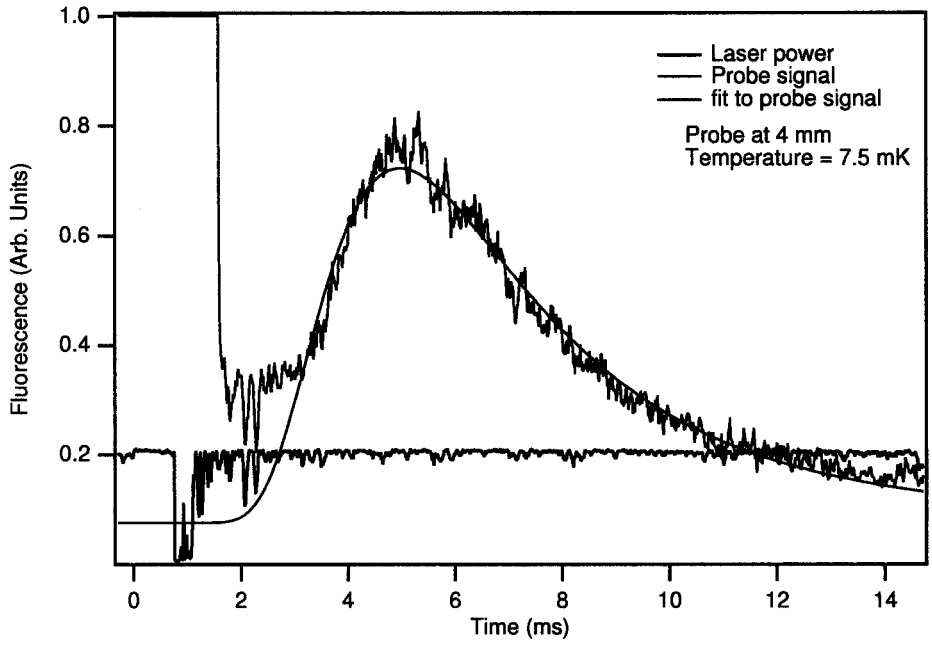

Figure 7.9: The TOF signal for the blue MOT of 7.5 mK for with the probe at distance 4 mm from the MOT.

come down to the level at which we can detect the escaping atoms.

To optimize the trap temperature, we had a pseudo-real-time measurement of the temperature. The computer triggers on the optical switch, and monitors the MOT PMT and laser power. The PMT signal is fed via a DAC board into a PC, fitted to a model, and the temperature is extracted in a program named "TFit." For fast fitting, it was found that it was adequate to model the cloud as a point source having a velocity distribution which is Maxwell-Boltzmann, and the probe beam at a constant radial distance from the cloud. Equation 3.7 converted to the time domain is

$$f(t) \propto \frac{d^3}{t^4} e^{-M(d/t)^2/2k_BT} \tag{7.6}$$

where t is the time elapsed from the release of the atoms, and d is the distance of the probe from the atom cloud. Figure 7.9 shows such a fit for a 7.5 mK cloud with the probe at 4 mm away from the cloud. We verified that at this temperature, gravity does not have a significant effect on the atoms, as it does in traps at lower temperatures in alkali

traps [Let88]. Because the measurement method is destructive, the entire cycle is repeated at a rate of 1–3 Hz, limited by the loading rate of the MOT. For each measurement, the fitted temperature was displayed on the computer monitor, allowing us to optimize the alignment of the optics. The lowest temperature we observed in ^{174}Yb was 4 mK, about 6 times hotter than the Doppler limit of 690 μK. For high number densities of trapped atoms and low temperature, it was also crucial to have the beams well aligned so that returning beams are exactly reflected back onto themselves. Others working on $^1S_0$ ground state elements have found similar temperatures. In Yb, 2 mK was reached in Oregon [Lof00a], 3 mK in Ca [Zin00], 2 mK in another experiment on Ca [Cur01], 3 mK in Mg [Sen94], and 1 mK in Sr [Kat99b].

The temperature depends strongly on the MOT alignment and it was difficult to reproduce the same conditions on a day to day basis. However, comparison made on the same day verified that the temperature extracted from the fit is not dependent on the distance of the probe. Distances between 4–9 mm were investigated. The results presented in this section so far are for ^{174}Yb. We also measured the temperature for two other isotopes, ^{172}Yb and ^{171}Yb. Under similar conditions, the temperature for the ^{172}Yb was similar to ^{174}Yb, but the ^{171}Yb was twice as cold, hinting at sub-Doppler cooling due to the multiple ground states. The TOF signal from the ^{173}Yb trap was too small to detect. More on the role of the hyperfine structure of the odd isotopes on sub-Doppler cooling will be discussed in the context of the $^1S_0$–$^3P_1$ transition in Chapter 8.

7.3.4 Blue MOT with Green Probe

The difficulty in locating the center of the magnetic quadrupole field center was discussed in Section 7.3. The task was made easier by the introduction of the green laser for the intercombination line, $^1S_0$–$^3P_1$. Because the green transition is much narrower than the blue, we could use it to probe low temperatures while they were trapped in the blue MOT. The quadrupole field of the MOT causes Zeeman shift and broadening in the $M = 0 \rightarrow \pm 1$ transitions, but not in the $M = 0 \rightarrow 0$ transition, and with this information, we were able to move the blue trap until it coincided with the magnetic field zero.

Figure 7.10 shows three scans: atoms were trapped by the blue transition and the green laser at 556 nm was scanned in frequency while the green fluorescence was monitored by a PMT. To filter out the overwhelming signal from the blue transition, a color filter was placed in front of the PMT (Coherent GG-495, 36-9439) which has an internal transmittance of less than 10^{-5} at 400 nm. In Figure 7.10 (a), only the vertical beam was used as a probe. The center peak is the $\Delta m = 0$ transition, and as it is not susceptible to any magnetic field. The only source of broadening is Doppler and power broadening. The two side peaks are the $\Delta m = \pm 1$ transition, and when the atoms are not at the center where the average field is zero, there is an overall shift to the peaks, as well as broadening from the magnetic field gradient. The green laser power in this particular figure is 5 mW.

Figure 7.10 (b) shows the scan when 20 mW of the green laser is combined with the blue laser at the beam splitter cube which divides the laser between the vertical and the horizontal MOT beams as in the case for the green MOT. All six beams comprising the blue MOT are accompanied by a green beam as well. The side peaks are much narrower and have less center shift than shown in (a), suggesting that the cloud is closer to the center where the average magnetic field is zero, and cloud size smaller. In (c), all three peaks are indistinguishable, and the MOT is well centered. Ref. [Lof00a] discusses in detail measurements of the position, size, and temperature from the split in the Zeeman components and the widths of the peaks.

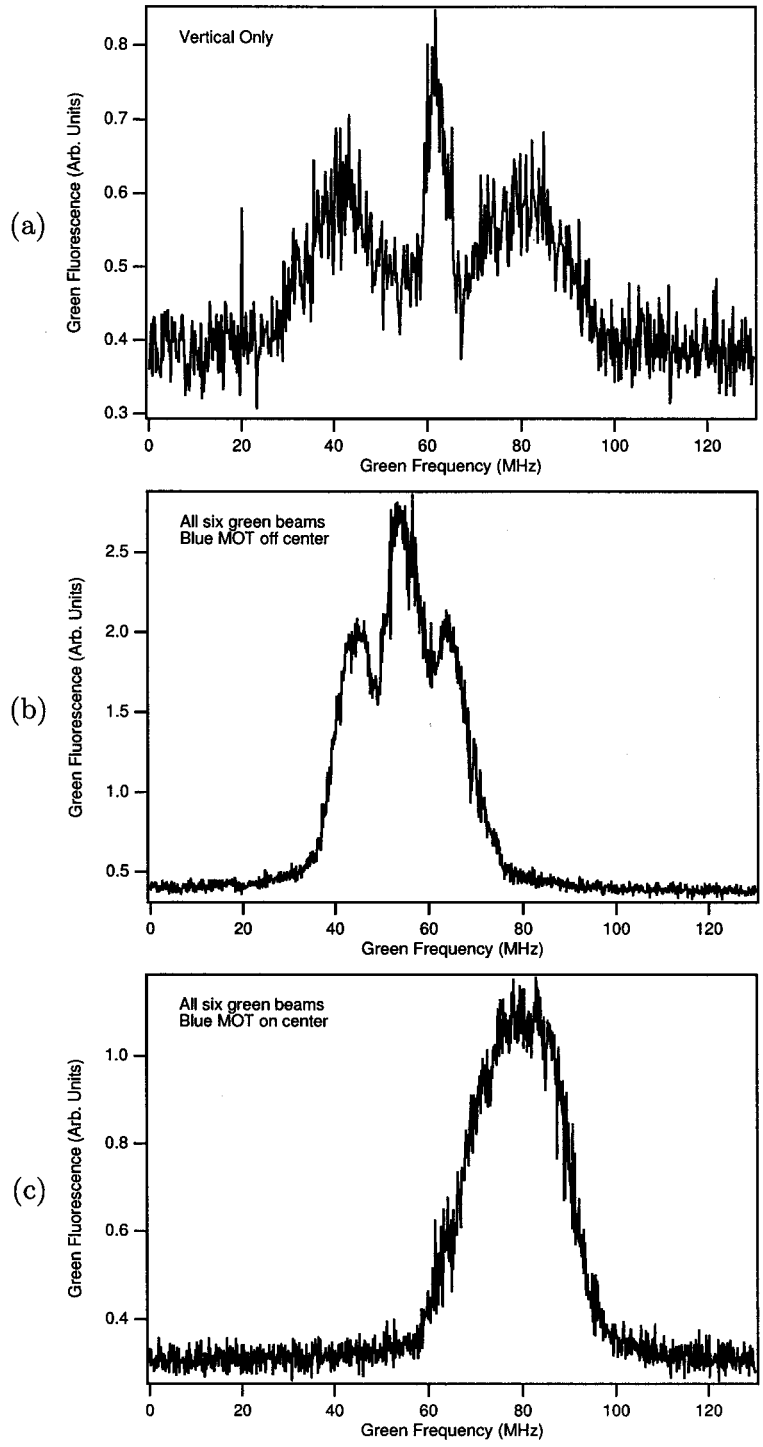

Figure 7.10: Green fluorescence from the blue MOT as the green laser was used as a probe. (a) shows the scan when only the vertical green beam was on, (b) shows the scan when all six of the blue MOT beams had green beams overlapped, and the MOT was off-center, and (c) is the same as (b), except that the MOT was more in the center.

Chapter 8

GREEN MAGNETO-OPTICAL TRAP

While it is possible to apply a large force on the atoms using the blue transition, there are limitations to the blue MOT. The short lifetime and high temperature of the trapped atoms limit the performance and utility of the blue trap. To continue with the preliminary EDM experiment and other experiments mentioned in Chapter 2, it is necessary to cool the atoms further and keep them trapped for a longer time. A MOT using the much weaker $^1S_0$–$^3P_1$ intercombination line at 556 nm offers these opportunities.

The green trap has several advantages over the blue trap. The narrower linewidth of 190 kHz results in a lower Doppler cooling limit of 4.4 μK as compared to the 690 μK of the blue transition. The lifetime of the blue trap is limited to 800 ms due to the branching ratio into the D-states. The $^1S_0$–$^3P_1$ transition is a completely closed transition, and the trap lifetime is limited only by collisions, either among the Yb atoms or with background gases. In the blue trap, the number of trapped atoms is limited by the trap lifetime and the loading efficiency. With the longer trap lifetime in the green MOT, more atoms can be trapped, and this will be important for future experiments with collision studies, cooling properties, or creation of quantum degenerate gases. The colder temperature in the green MOT and the addition of a high quality CCD camera which can be triggered from an external signal have added more flexibility that allow us to study cooling properties of atoms with $^1S_0$ ground state in a MOT.

Having multiple even isotopes and two odd isotopes with different spins allows us to conduct comparison studies with only a slight change in the laser tuning. In particular, sub-Doppler cooling mechanisms such as Sisyphus and corkscrew cooling depend on the number of magnetic sublevels in the ground state. Doppler cooling can be studied in the even isotopes without the dominating sub-Doppler cooling. Since $J = 0$, any cooling mechanism which requires multiple sublevels can only occur in the isotopes which have nuclear spin $I \neq$

0. Yb has three different spins represented in seven stable isotopes. We have compared laser cooling in three isotopes of Yb: ^{174}Yb ($F_g = 0 \rightarrow F_e = 1$), ^{171}Yb ($F_g = 1/2 \rightarrow F_e = 3/2$), and ^{173}Yb ($F_g = 5/2 \rightarrow F_e = 7/2$). This is the first observation of Sisyphus cooling in atoms with ^{1}S$_0$ ground state, that is, with no electron angular momentum.[1]

8.1 Experimental Setup: Green MOT

The overall green trap schematic including the optics layout is shown in Figure 8.1. The vacuum chamber did not need any modification from what was used for the blue MOT, and remains unchanged from what is shown in Figures 5.2 and 5.3 (some components such as pumps, rotary feedthrough, and valves have been omitted for clarity in Figure 8.1). Because the $^1S_0$–$^3P_1$ transition is weak, the initial cooling and trapping is carried out with the blue transition as described in Chapter 7.

The green 556 nm laser is located on a second table. The light is transported over to the primary optical table with an optical fiber. The polarization of the output of the fiber is corrected by a half-waveplate and a polarizer to rotate the laser polarization coming out of the fiber which is rotated by an unknown amount depending on how the fiber is coiled on the table. The laser is then focused into an AOM. The zeroth order goes toward the long-term frequency stabilization lock chamber, and the first order goes toward the MOT. The MOT beam intensity can be controlled by changing the power of the RF driving the AOM. This AOM is also used as a switch to completely turn off the MOT beams. In addition, sidebands can be added to the green MOT laser when a broader laser is required. The laser-lock beam is reflected upward into the lock-chamber with a mirror, going through a quarter-waveplate, through the lock chamber, and retro-reflected back down to avoid steering the atomic beam. More details on the long-term laser frequency lock is found in Section 6.2.3.

The laser that comes out from the fiber has a nice Gaussian mode. However, the beam is distorted when it goes through the AOM, and needs to be spatially filtered to produce a Gaussian profile by creating a tight focus with a microscope objective lens and sending the

[1]We have recently become aware of a study by a group at JILA led by Jun Ye which is currently under review by the Physical Review Letters. They have conducted studies on sub-Doppler cooling in Sr atoms in a MOT using the $^1S_0$–$^1P_1$ transition [Xued].

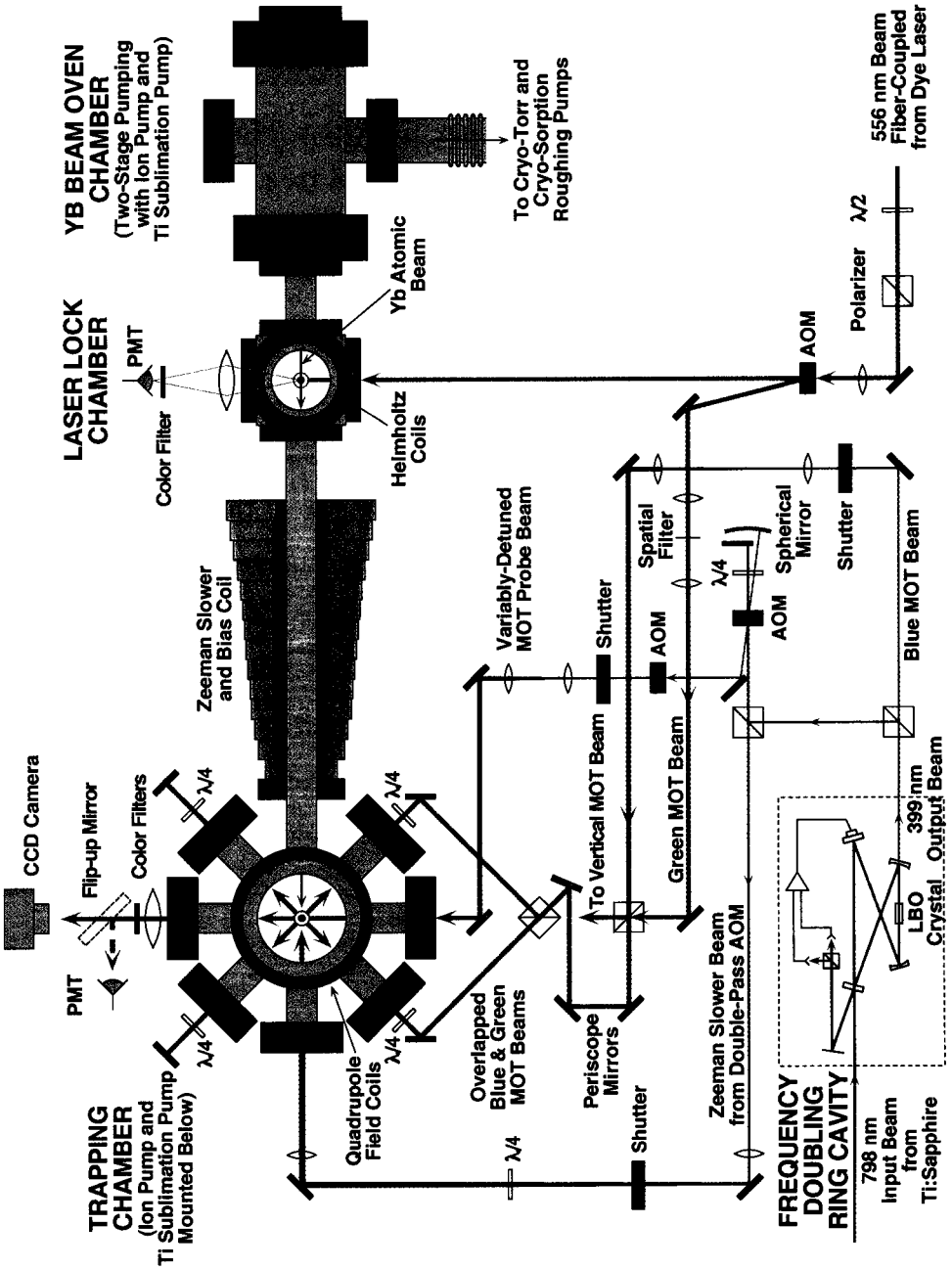

Figure 8.1: Green MOT apparatus schematic. The 556 nm dye laser and laser narrowing scheme which are shown in Figure 6.5.

beam through a 25 μm pinhole. The beam is shaped with another lens for the MOT, and combined with the blue MOT beams at the beam splitter cube that separates the vertical and horizontal MOT beams. From there, the MOT beams copropagate throughout the MOT setup. The blue beam can be turned off further upstream by a mechanical shutter (Uniblitz LS3), which has a 500 μs closing time. The laser beam is focused near the aperture of the shutter, and is shut off by a blade of the shutter within 50 μs.[2] The MOT beams are slightly converging and are roughly 10 mm in diameter as they enter the chamber, and 8 mm when they come back out from the MOT.

We use quarter-waveplates made for 556 nm (Special Optics 8-8008-1/4-556) rather than for 399 nm. We expect roughly 90% of the blue trap beams to be in the correct circular polarization from calculations, and we found that the performance of the blue MOT is not affected significantly by this change. The polarization of a linearly polarized 399 nm laser as it passes through waveplates made for 556 nm on either side of the MOT are shown in Figure 8.2. The first quarter-waveplate is set at 45° and the optimal angle for the second waveplate on the other side of the MOT is at 90° with respect to the first plate. The retroreflected beam has the same amount of circular polarization, but rotated by 90°.

For probing the MOT, we use the stronger $^1S_0$–$^1P_1$ transition. The blue absorption probe beam is taken from the zeroth order of the second pass of the Zeeman slower AOM (nominally −150 MHz from atomic resonance), and passed through another AOM to shift it back on resonance. With this configuration, the blue MOT and Zeeman slower can be tuned independently from the probe for optimal performance. There is a mechanical shutter for the Zeeman slower (Uniblitz LS3) so that the Zeeman slower can be turned off for the green trap without turning off the probe.

The probe beam is sent in horizontally through the optical ports perpendicular to the atomic beam, through the MOT, an imaging lens, and into a CCD camera by Princeton Instruments (now Roper Scientific, TE/CCD-512), controlled by MicroMax/ST-133. The imaging lens is set so that the images of the trapped clouds have a magnification of 1.4. A

[2]In comparison, the shut-off time was 5 μs with the doubling-cavity lock kick technique used for the time-of-flight temperature measurement of the blue MOT. For the purposes of transferring the atoms into the green MOT, the mechanical shutter is sufficient.

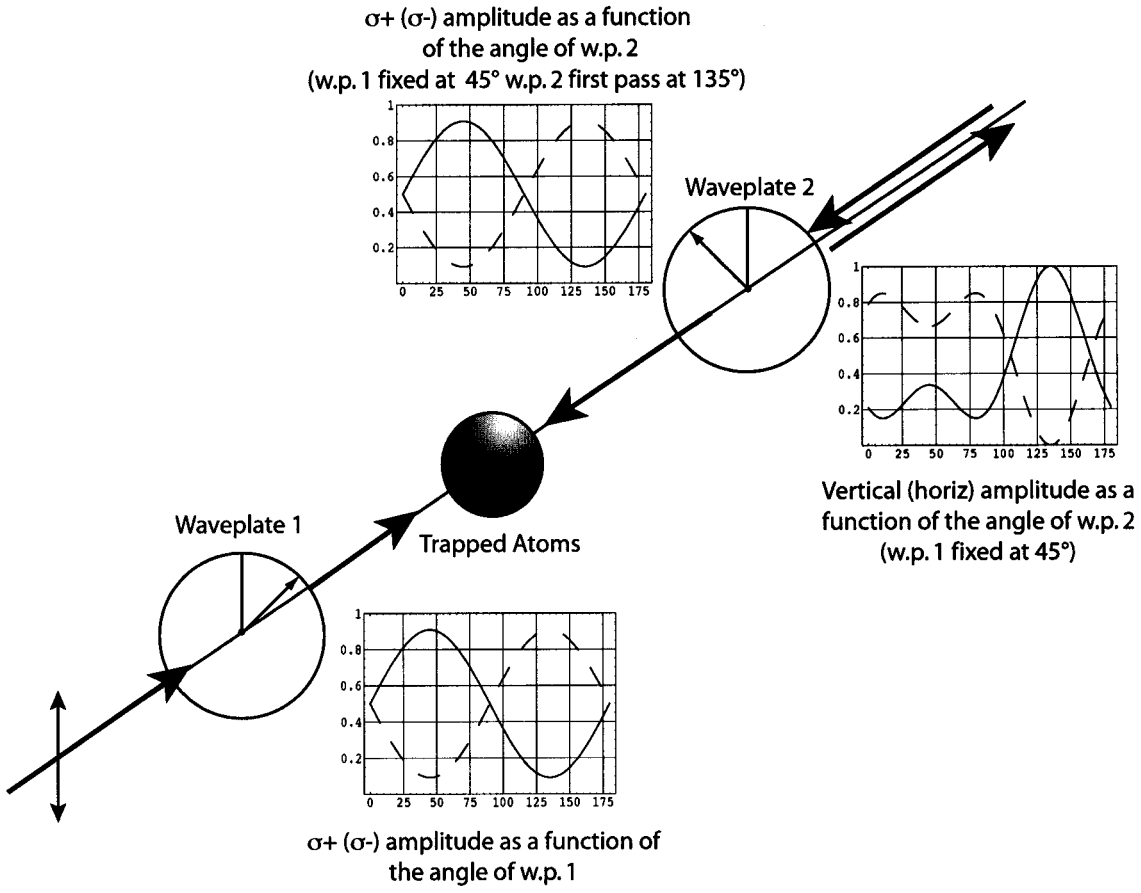

Figure 8.2: Resulting polarization when quarter waveplates made for 556 nm are used for 399 nm.

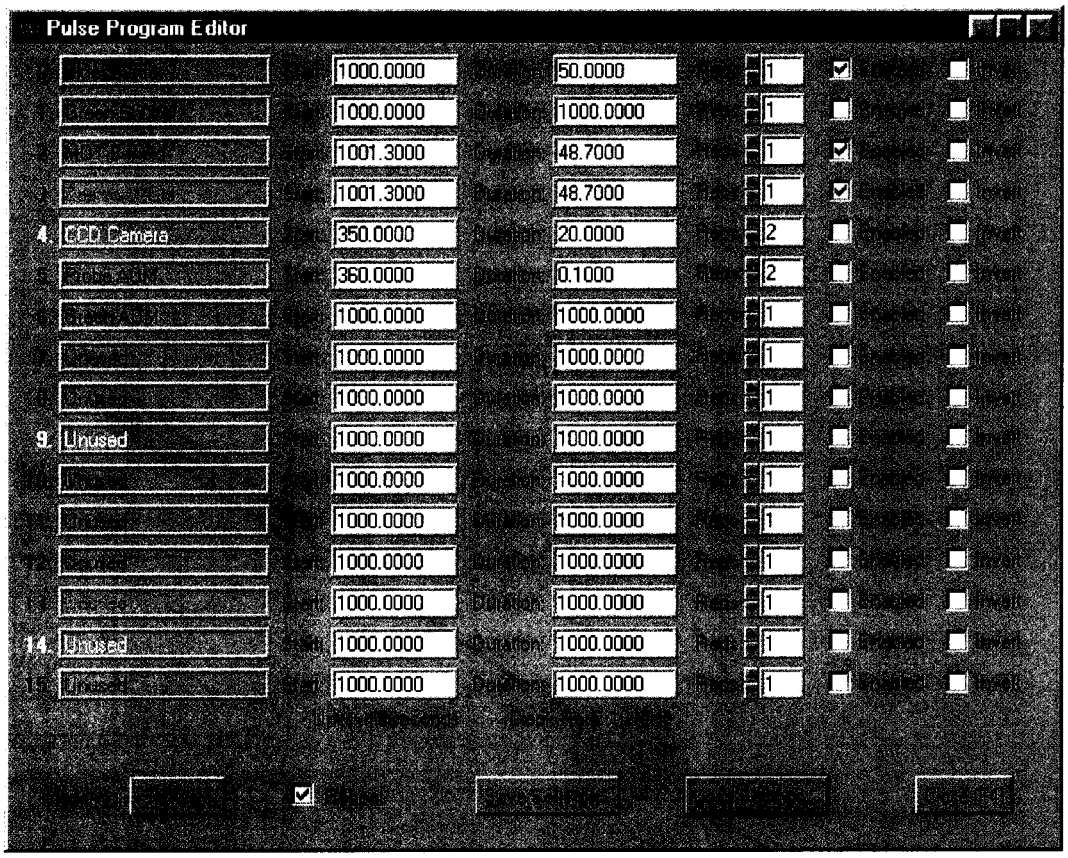

Figure 8.3: Timing sequence sent to the pulse generator for loading the green MOT.

mirror mounted on a flip-up mount is used to monitor the MOT with a PMT when necessary. A filter wheel allows us to insert either a blue or green color filter in front of the PMT and the CCD camera to block the unwanted color. The blue filter, Coherent BG3 36-9207, blocks green light to better than 10^{-3}, and the green filter, Coherent GG495 36-9439, blocks the blue light to better than 10^{-5}.

The timing for the mechanical shutters, AOMs, changing the magnetic-field gradient, and CCD camera shutter are controlled by a pulse generator card, PulseBlaster from SpinCore Technologies. It has 24 channels of TTL output, individually programmable to 10 ns. We have developed a software which allows us to set the timing of the desired channels with ease. Figure 8.3 is an example of such a timing sequence, used to optimize the green MOT

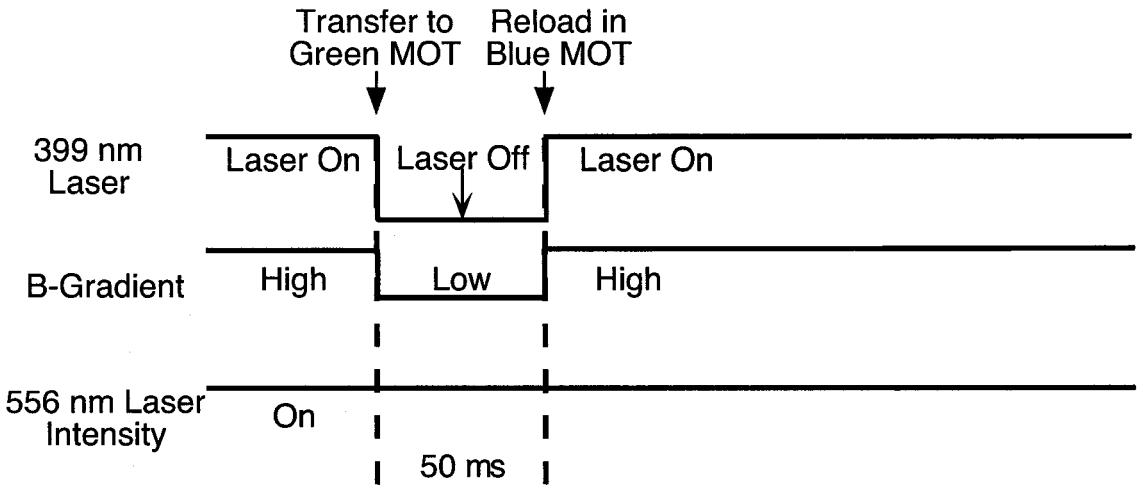

Figure 8.4: Timing schematic for R&R diagnosis of the green MOT loading efficiency.

loading condition described in Section 8.2. The channels checked "Enabled" will wait low until the start time (all time in units of ms), and goes high for the specified duration, and repeats itself by the number of times specified in the "Reps" box. If the "Invert" box is checked, the pulse is initially high and goes low at the time specified by "Start". If the "Repeat" box at the bottom is checked, the pulse generator the channels that finish their cycles first will wait until the other channels have completed their cycle, and the entire sequence is repeated.

8.2 Loading the Green MOT

Loading the green MOT is slightly more subtle than loading the blue MOT. The atoms have to first be trapped in the blue MOT, then transferred into the green MOT. The green trapping beams are left on during the initial cooling and trapping with the stronger blue transition, and the transfer into the green MOT is accomplished by turning off the blue beams with a mechanical shutter and turning down the magnetic field gradient.

To guide us in optimizing the conditions for high transfer efficiency, we use what we call the "Release and Recapture" (R&R) procedure. In this procedure, the green fluorescence is

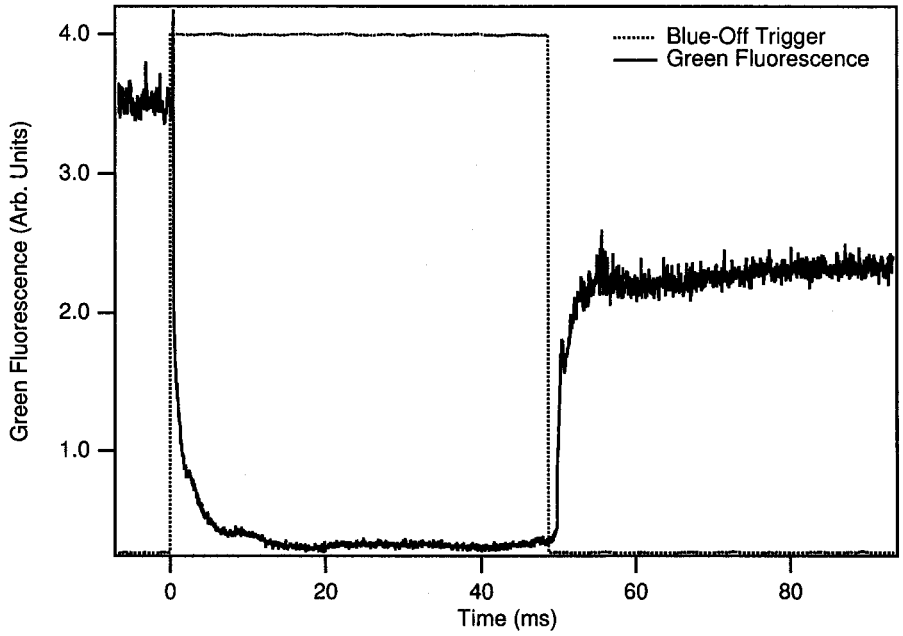

Figure 8.5: Release and recapture: successful atom transfer into the green MOT. The green fluorescence is monitored with a PMT. Both the green and blue lasers are on until t = 0. Only the green laser is on between $0 \leq t < 50\,\text{ms}$, and at t = 50 ms the blue laser comes back on. The atoms are trapped in the green MOT, and 70% of the atoms still remain when the blue laser turns back on at t = 50 ms. In this figure, the laser is tuned to $\delta = -60\gamma$ ($-12\,\text{MHz}$), and the laser intensity is $I = 20\,\text{mW/cm}^2$. The atoms fluoresce more in the green when the blue MOT is on due to various line broadening and shifts induced by the blue laser.

monitored with a PMT while the green laser is left on and the blue MOT is turned off and on again. If the atoms are successfully transferred into the green MOT, the atoms are still in the trap region when the blue MOT comes back on. If the atoms are not trapped in the green MOT, the blue MOT has to build up its population from zero. The timing sequence is repeated while the conditions for the transfer such as laser intensity, frequency, and the magnetic-field gradient are optimized for the most efficient transfer. The blue fluorescence is blocked from the PMT by a color filter, and the "TFit" program records the fluorescence.

R&R refers to what is happening to the atoms from the blue trap. Figures 8.5 and 8.6 show the monitored green fluorescence as a function of time. The blue laser is turned off at time t = 0 and back on after 50 ms, while the green laser is left on continuously. During those 50 ms, the atoms are held only by the green MOT. An example of atoms being successfully

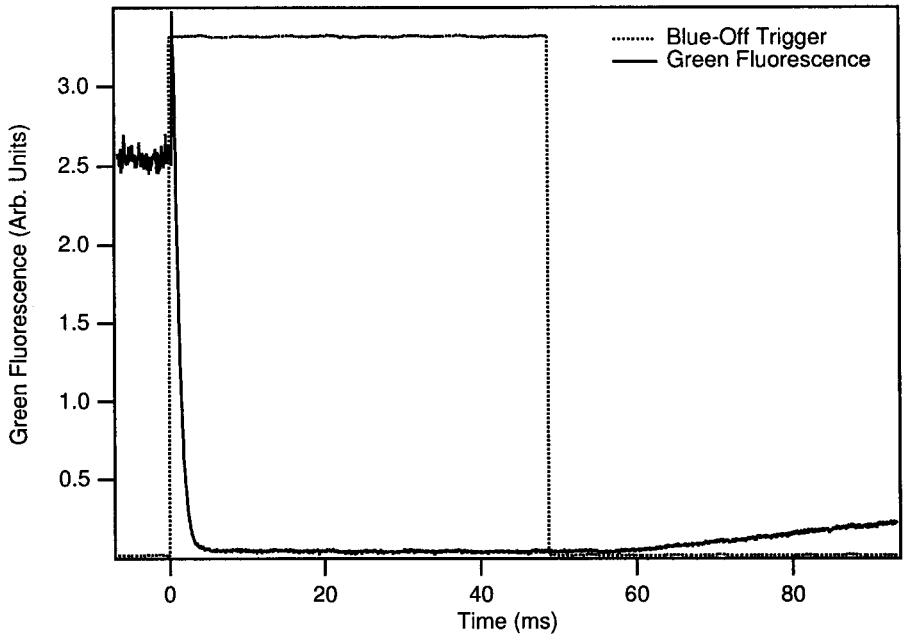

Figure 8.6: An unsuccessful transfer of atoms from the blue to the green MOT. Release and recapture employed with the green frequency tuned higher than resonance. No atoms remain when the blue laser comes back on at t = 50 ms. The laser is tuned to $\delta = +5\gamma$ (1 MHz), $I = 20\,\mathrm{mW/cm^2}$.

transferred into the green MOT is shown in Figure 8.5. The blue trap is turned off at t = 0. When the blue laser comes back on after t = 50 ms, 70 % of the atoms still remain in the MOT region, and are recaptured by the blue MOT. Figure 8.6 shows an unsuccessful transfer, and the blue MOT has to rebuild its population from nothing when it comes back on at t = 50 ms.

Figures 8.5 and 8.6 show that there is more green fluorescence when both lasers are on than when only the green MOT beam is on. There are several reasons for this: When the atoms are trapped by the green MOT, they are colder and occupy a smaller volume (the blue trap is about 2 mm in diameter whereas the green is about 0.4 mm). In the green trap, the region where the red-shifted laser is on resonance with the Zeeman shifted sublevels lies outside of the volume of the trapped atoms. In this condition, the atoms hardly fluoresce. If both blue and green trap lasers are on, the atoms are hotter and occupy a larger volume. The spatial distribution of the atoms and the Doppler broadening help bring more atoms

closer to resonance.

We found that the transfer works well when the green laser is detuned by -13 to -60γ (-2 to -12 MHz), the magnetic-field gradient changes from 30 G/cm for the blue down to 15 G/cm for the green MOT, and the green laser intensity is $I_{tot} \geq 20\,\mathrm{mW/cm^2}$. It takes less than 400 μs to turn down the magnetic field gradient, and 50 μs to turn off the blue laser with a mechanical shutter. The sequence is cycled at 1 Hz while monitoring the signal to optimize the laser alignment, frequency, intensity, and magnetic field gradient for the maximum recapture. An example of the timing sequence used to control the pulse generator is shown in Figure 8.3.

8.3 Trap Lifetime

The R&R method described in Section 8.2 can also be used to monitor the trap lifetime by extending the time that the blue MOT is off. We have observed some evidence of density dependent loss in the green trap (see Section 7.3.2), but it was difficult to make a systematic study of the lifetime due to drop-outs and instabilities in the green dye laser. The possible sources for the instabilities include bubbles in the dye jet, mechanical, and electrical noise.

Figures 8.7 and 8.8 show a lifetime measurement at $I/I_s = 100$ with $\delta = -5\gamma$ and $\delta = -10\gamma$. An exponential fit to the signal gives a lifetime of 14 s and 77 s respectively. With the smaller green trap laser detuning, atoms are much more likely to experience light-assisted collisions and the lifetime of the trap is greatly reduced. The trace shown in Figure 8.7 also deviates from an exponential. A fit to the number-dependent decay in Equation 7.5 gives a better fit.

The sharp drop in the fluorescence at roughly 19 s in Figure 8.7 is due to the laser instabilities. Disturbances to the laser causes the lock to come undone, sometimes swinging the frequency to the blue of the resonance. When this happens, the atoms are pushed out of the trap region, and when the laser lock comes back on, all the atoms are gone. The signal that remains after the lock is reacquired is only the background light seen by the PMT. The longer drop in the signal in Figure 8.8 is due to the MOT beams being blocked on purpose and establishes the background level. It was rare to go for more than a few seconds

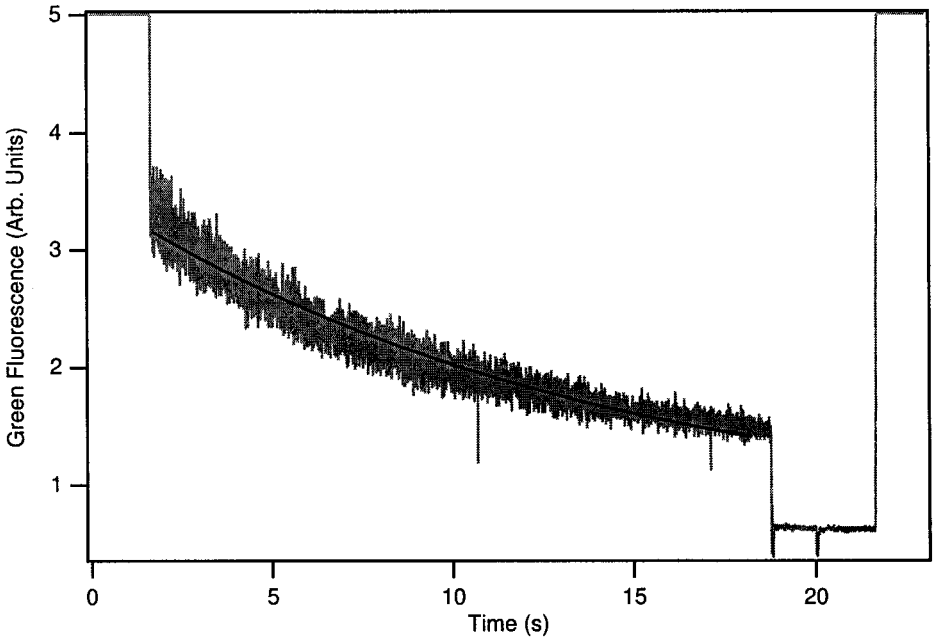

Figure 8.7: Green fluorescence vs. time for ^{174}Yb at $I/I_s = 100$, $\delta = -5\gamma$, and $\tau = 14\,\mathrm{s}$. The black line shows an exponential fit.

between the laser lock drop-outs, and this is certainly one of the improvements that needs to be made to the system.

8.4 Time-of-Flight (TOF) Temperature Measurement

Two absorption images are taken for each cloud to determine the temperature of the clouds of trapped atoms with a time-of-flight method, one while the trap is still on, and one after the trap is turned off and the clouds are allowed to expand for a prescribed time. By determining the size of the initial and the expanded clouds, σ_i and σ_f, and knowing the time that the atoms were allowed to expand, τ_{TOF}, the root-mean-square velocity of the atoms is given by

$$\langle v_{rms}^2 \rangle = (\langle \sigma_f^2 \rangle - \langle \sigma_i^2 \rangle)/\tau_{TOF}^2. \tag{8.1}$$

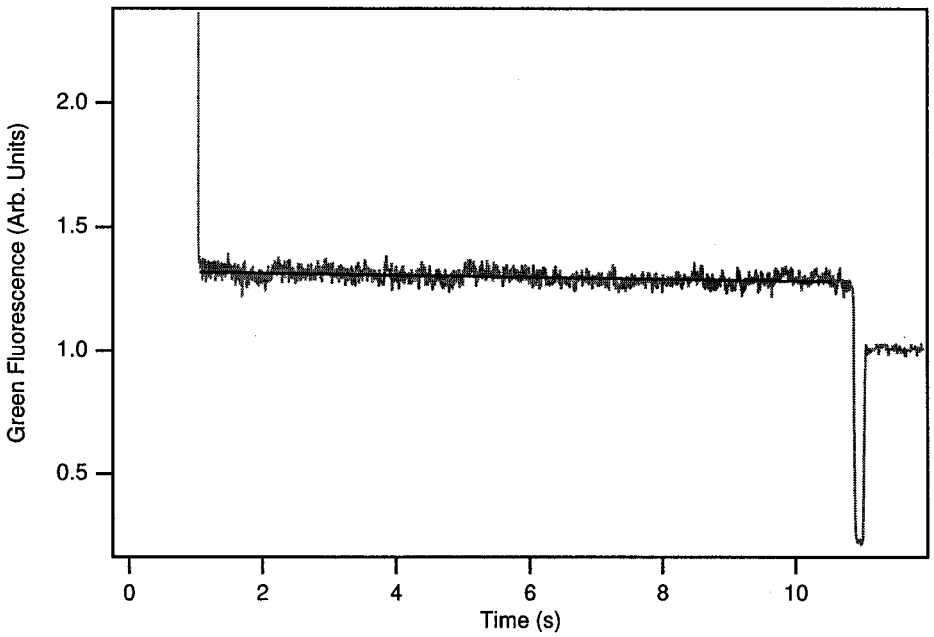

Figure 8.8: Green fluorescence vs. time for ^{174}Yb at $I/I_s = 100$, $\delta = -10\gamma$, and $\tau = 77\,\mathrm{s}$. The black line shows an exponential fit.

The solution to the Fokker-Planck equation gives a Maxwell-Boltzmann velocity distribution of the trapped clouds [Met99] and we can assign a temperature accordingly as

$$T = M\langle v_{rms}^2 \rangle / k_B. \tag{8.2}$$

The size of the initial and final clouds are extracted by fitting a two-dimensional Gaussian surface to each image as described in Section 8.5. The size of the images are compared and the temperature is calculated by Equation 8.2. The total number of atoms in the trap can also be extracted by integrating the amount of light absorbed by the atoms across the image, and pairs of images where the number of atoms did not agree to within 30% were rejected.

The conditions for optimal transfer from the blue to the green trap are not necessarily the same as the conditions desired for the temperature study, and the laser frequency, intensity, and magnetic field gradient were adjusted after the transfer was complete. The timing sequence for imaging is outlined in Figure 8.9 and 8.10. The blue trap, Zeeman slower, and

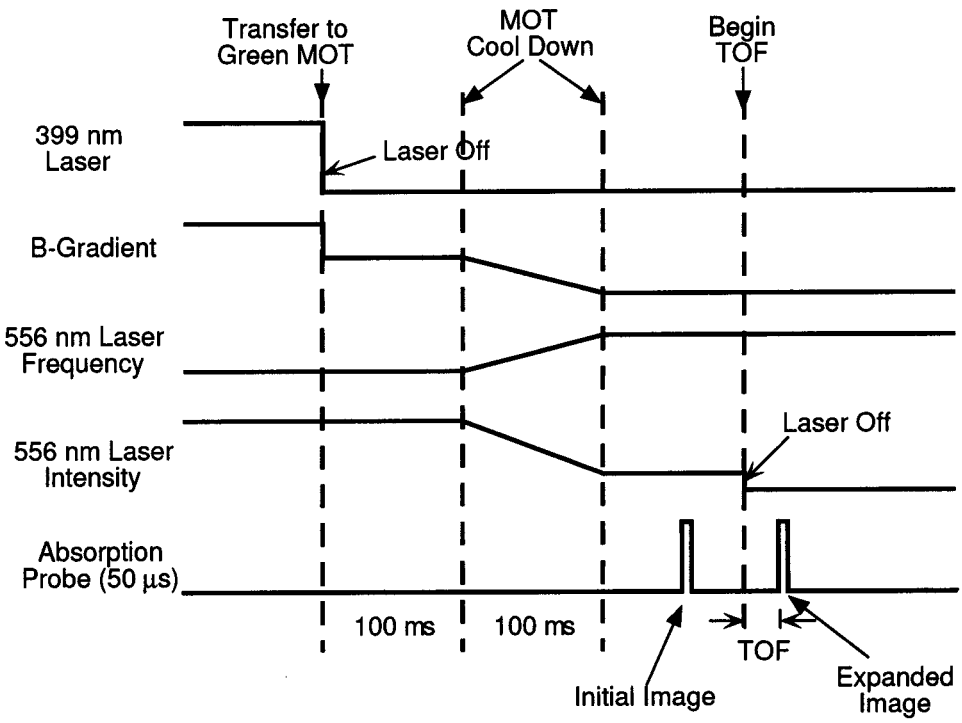

Figure 8.9: Schematic of the timing of the pulses for TOF measurement used to control the blue laser shutter, green laser intensity, magnetic field gradient, and blue probe AOM. In addition, the Zeeman slower, CCD camera shutter, and shutter for the probe were also controlled by the pulse generator. This figure is not to scale.

green laser are left on for 1–2 s while accumulating the atoms into the blue MOT. Then the blue MOT laser is turned off with a shutter and the atoms are transferred into the green MOT as described for the R&R method. At the same time, the acousto-optic modulator (AOM) for the Zeeman slower is shut off by an RF switch, and the magnetic field gradient is turned down.

The timings of the response of the mechanical shutters and the CCD camera shutter are somewhat unreliable due to the delays in the instruments that vary from shot to shot. To ensure that the camera shutter is completely open when the absorption probe comes on, it is necessary to send the TTL to the camera trigger before the probe beam is pulsed on. The 10.5 ms duration of the camera pulse ensures that the sum of the camera and probe

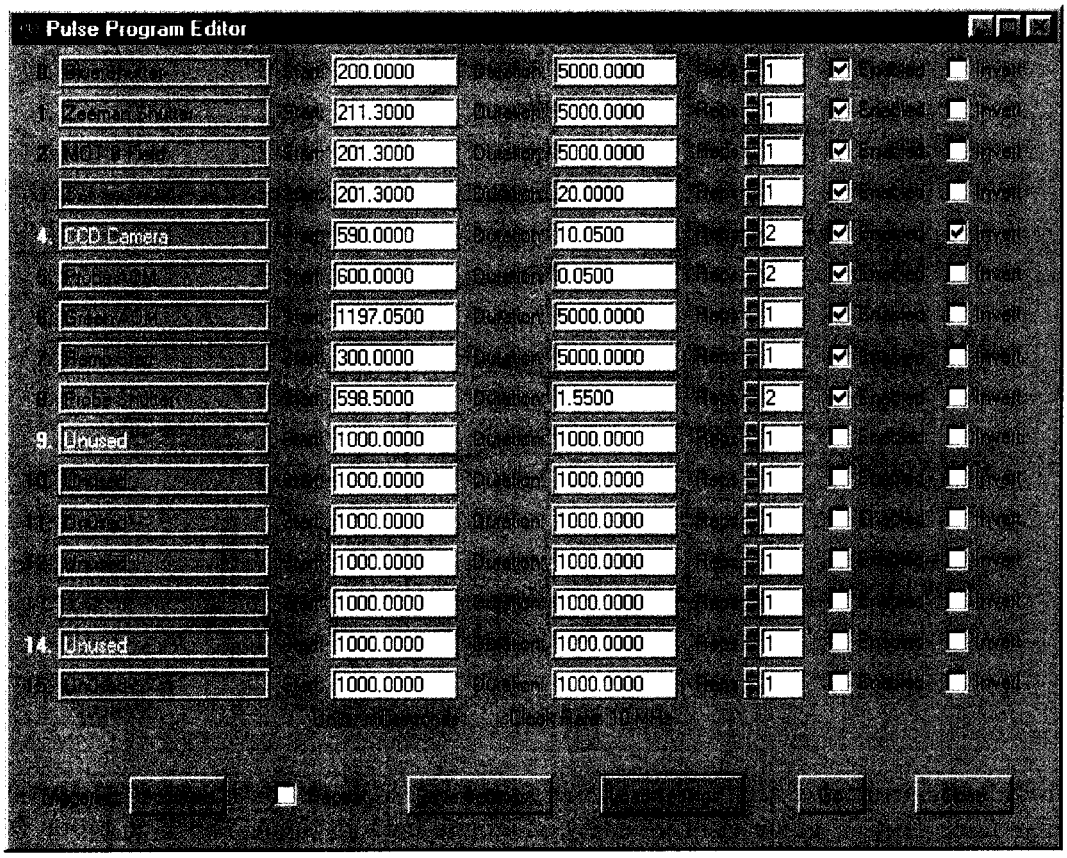

Figure 8.10: Pulse generator setting for TOF image capture timing.

times are equal, and the timing of the repeated cycles of the camera and the probe are synchronized for the second image. The Uniblitz shutters require that the TTL be sent 1.3 ms earlier than the desired shutter close time.

After the transfer from the blue to the green MOT, we wait for 100 ms to let the atoms come to an equilibrium while the atoms go through damped oscillations and settle in the potential of the new MOT. The green laser intensity, frequency, and magnetic field gradient are gradually changed over 100 ms to bring the MOT to the condition of interest. After the atoms are allowed to come to an equilibrium again over 100 ms, the first image is taken. The probe beam used for the absorption imaging is on resonance with the $^1S_0$–$^1P_1$ transition. It has a 1 cm diameter, power of 0.1 mW, and duration of 50 μs. We have verified that no

detectable number of atoms are lost from turning on the probe beam if the trap is still on. After a delay of 350 ms (limited by the refresh rate of the camera), the green laser is turned off with an AOM, and another image is taken after the cloud expands for a specified time of flight.

8.5 Image Analysis

The absorption images are taken by sending a pulse of probe beam which is resonant with the stronger blue transition, through the trapped atoms, and onto the CCD camera. The atoms absorb the light, casting a shadow in the probe laser profile, and dark regions in the image indicate where the atoms are. The amount of light intensity, I, that remains after a laser beam goes through a sample of N atoms is

$$I = I_0 \, e^{-\eta\sigma N/A} \tag{8.3}$$

where I_0 is the intensity of the incident light, $\sigma = 3\lambda^2/2\pi$ is the maximum cross-section for photon absorption, $\eta \leq 1$ is the fractional reduction of the cross-section due to broadening or laser detuning, and A is the area. Although there are no appreciable line-broadening in the trap for the blue transition and the probe has $\delta = 0$, $\eta = 1/2$ was used to be cautious, making $\eta\sigma = 3\times10^{-10}\,\mathrm{cm}^2$. To obtain the total number of atoms in the trap, Equation 8.3 is applied to each pixel. The area, A, is the area of each pixel with the magnification included ($A = (17\mu\mathrm{m})^2$ for this work). The number obtained from each pixel is summed over the entire region of interest to get the total number of atoms in the trap.

Each absorption image has two other images associated with it: background and normalization images. The background image has the dark counts of the CCD chip, and is taken with the camera shutter closed. With the chip cooled to $-5\,^\circ\mathrm{C}$, each pixel has roughly 100 counts on average. The normalization images are taken by using the same timing sequence as the absorption images and includes the probe beam, but no atoms. The background is subtracted from both the absorption and normalization images pixel by pixel, then the background-subtracted raw image is divided by the normalization image. The value for each pixel of this processed image is now I/I_0 in Equation 8.3. To determine the number of atoms detected in each pixel, the natural log is taken and divided by $\eta\sigma/A$. The total number

of atoms in the trap is found by summing the number over the entire cloud. Figures 8.11 and 8.12 outline these image processing steps.

To avoid condensation on the surface of the chip, there is a small volume of vacuum in front of the chip, with a window made of flat piece of glass with anti-reflection coating for UV. This window causes some problems for imaging. When a coherent light source such as the probe beam goes through the flat window, there is a significant amount of fringes produced by the interferences among the multiple reflections from the two surfaces. The fringes show up as stripes in the images. It is possible to purchase cameras equipped with a wedged window to avoid etalon effects, but its use with a coherent light source was not anticipated at the time of the purchase.

The fringes depend on the subtle alignment of the probe beam and are irreproducible between two shots, and difficult to reliably cancel out with normalization. The images are instead put through a two-dimensional low-pass filter by taking a convolution with a 9 pixels $\times$ 9 pixels Gaussian kernel. This is equivalent to taking a fast Fourier transform (FFT) of the images, cutting off the higher frequencies with a Gaussian falloff, and transforming back to form a filtered image. This method causes some broadening, but it was found to be negligible for the sizes of the clouds seen in this experiment.

For a sufficiently small number of trapped atoms, the number density distribution is Gaussian, as given by the solution of the Fokker-Planck equation for a damped harmonic oscillator. The rms-widths of the Gaussian shapes are σ_i and σ_f in Equation 8.1. We fit the images to the two dimensional Gaussian given by

$$\begin{aligned} G_{2D}(x,z) &= z_0 + ax + bz + \\ &\quad d\exp\left[\frac{-1}{2(1-\xi^2)}\left(\frac{(x-x_0)^2}{\sigma_x} + \frac{(z-z_0)^2}{\sigma_z} - \frac{2\xi(x-x_0)(z-z_0)}{\sigma_x\sigma_z}\right)\right] \end{aligned} \quad (8.4)$$

where z_0 is the overall count offset of the image, a and b are the slopes in the x and z directions of the image, d is the depth of the Gaussian, x_0 and z_0 are the location of the center of the cloud, ξ tips the axes, and σ_x and σ_z are the rms-height and -width of the clouds.

When the number of atoms is small, the size stays constant and the density increases

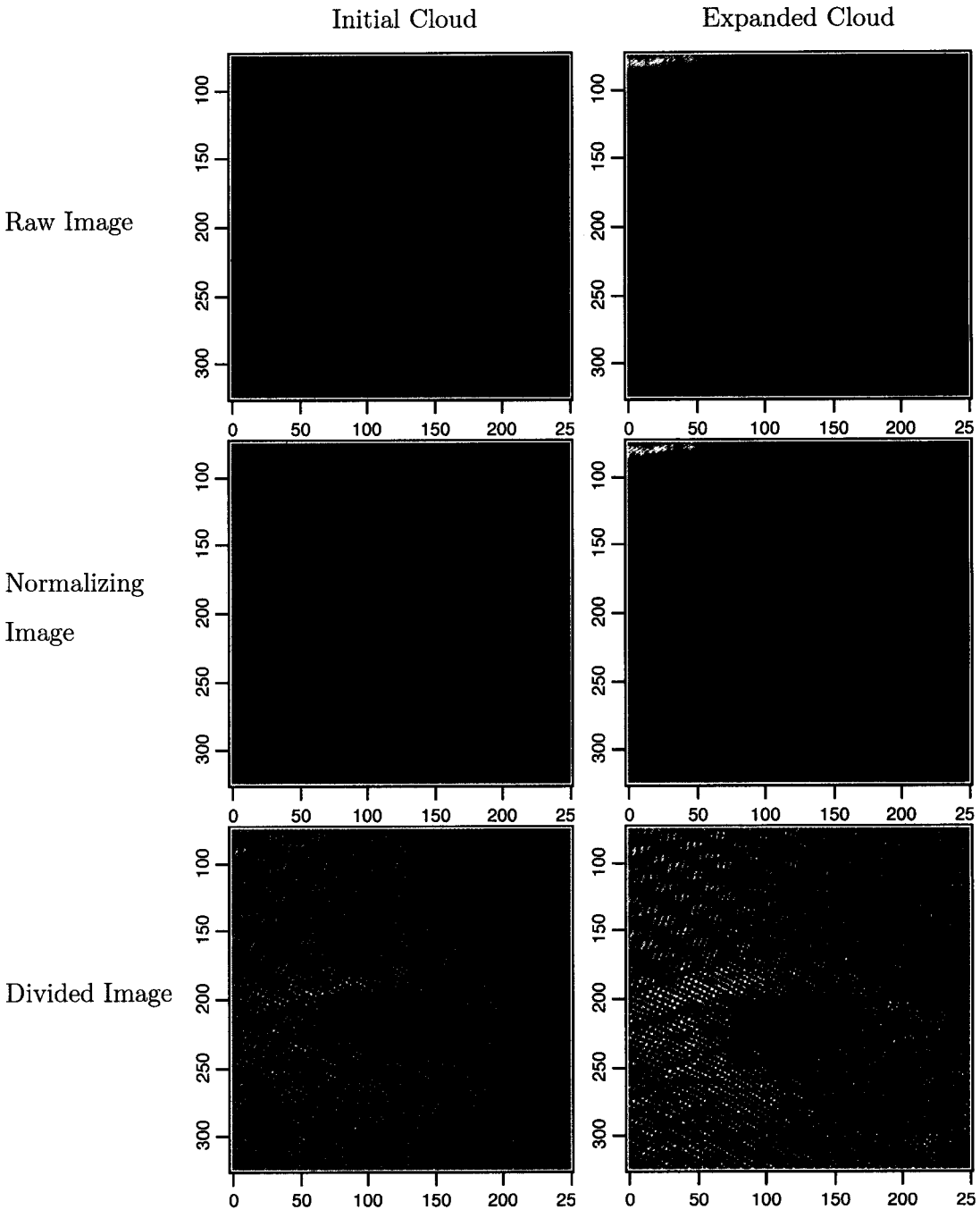

Figure 8.11: Image analysis sequence I. Image of the trapped (initial) and expanded (final) cloud of ^{174}Yb with $\tau_{TOF} = 3$ ms. The raw images are divided by normalizing images pixel by pixel, after which the natural log of the image is taken. The axes represent the number of pixels. The camera has a pixel size of 24 μm which, with the magnification of the imaging taken into account, one pixel shown here represents an object size of 17.4 μm.

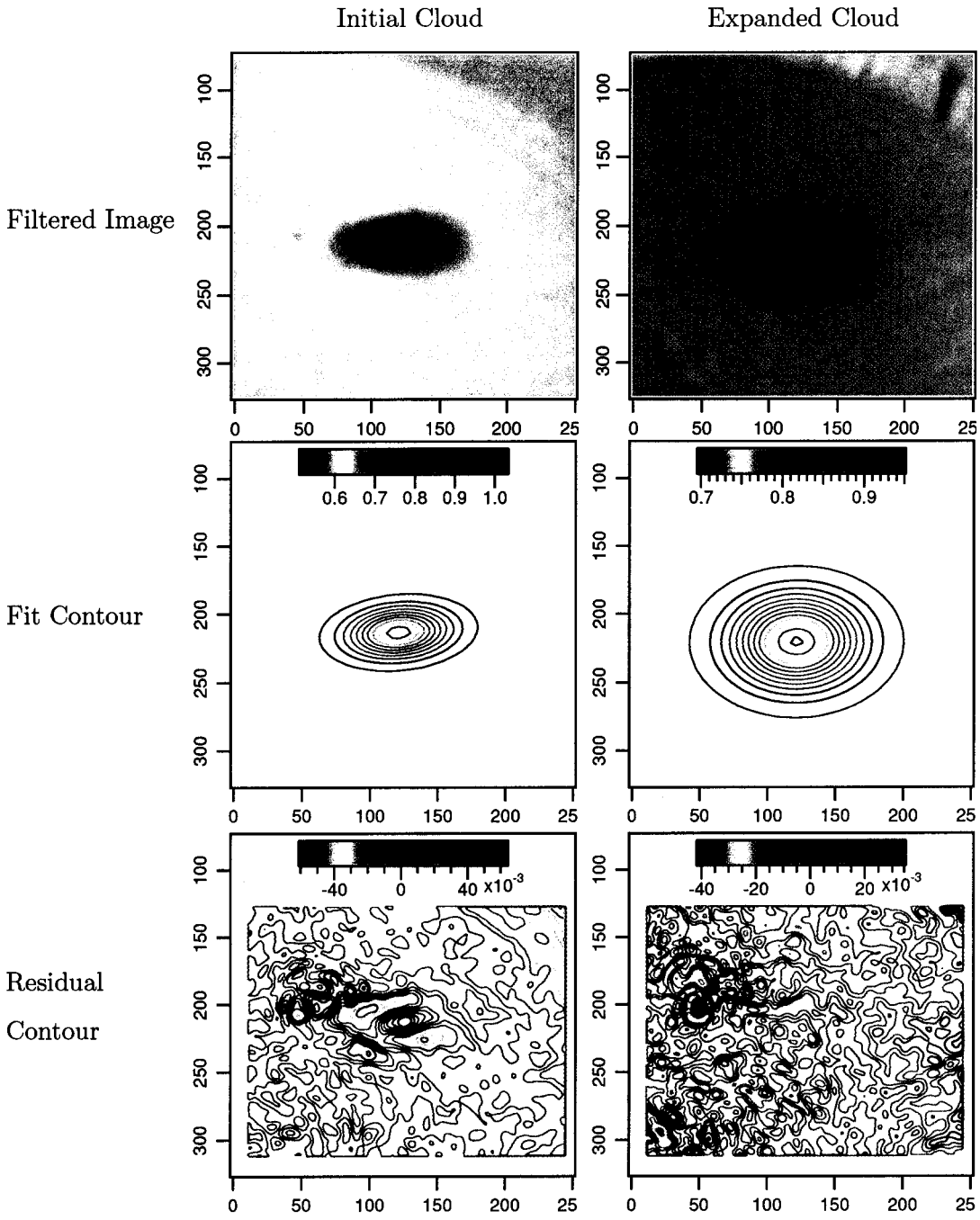

Figure 8.12: Image analysis sequence II. Image of the trapped and expanded cloud with $\tau_{TOF} = 3$ ms. The divided image seen in Figure 8.11 is filtered by taking a convolution with a 9×9 Gaussian kernel, resulting in images with better contrast. The natural log of each image is taken, and fitted to a 2-D Gaussian surface. The contour of the resulting Gaussian surface and the residual are shown. From the fit, we determine that this particular cloud has 4×10^6 atoms, with an initial width of $400\,\mu$m, with height of $200\,\mu$m. The final cloud is $530\,\mu\text{m} \times 380\,\mu\text{m}$.

as more atoms are loaded into the trap. For a larger number of atoms, radiation trapping leads to an increase in the size while the density remains constant [Wal90]. For alkali atoms which have transition lifetimes on the order of 20–30 ns, radiation trapping starts to have an effect at around $N \approx 10^5$ atoms. Our green trap typically has 10^6–10^7 atoms, but because of the long transition lifetime, radiation trapping effects are small and we found that the Gaussian fit deviates from the data by at most 10%.

8.6 Even Isotopes: Doppler Cooling

The even isotopes of Yb have no sublevels in the ground state and it is possible to explore the effects of Doppler cooling independent of the effects of sub-Doppler cooling. The temperature expected from Doppler cooling theory is quoted here from Equation 3.19:

$$T = \frac{\hbar\gamma}{8k_B}\frac{\gamma}{|\delta|}\left[1 + \frac{I_t}{I_s} + \left(\frac{2\delta}{\gamma}\right)^2\right]. \tag{8.5}$$

where $\gamma = 1/\tau$ is the natural linewidth of the transition, δ is the detuning of the laser, I_t is the total intensity of the trapping lasers, and I_s is the saturation intensity (see Table 4.4) [Let89]. From this equation, the temperature of the trap is expected to depend linearly on the trap laser intensity.

Figure 8.13 shows the temperature measured by the TOF method described in Section 8.4 for ^{174}Yb as a function of trap laser intensity. Examples of TOF images are collected in Figure 8.14. The diamonds in Figure 8.13 are the data, with the error bars corresponding to the standard deviation of the mean of 2–10 measurements at a given intensity, and the solid line is what is expected from the simple Doppler cooling theory. For this data, the expansion in both x- and z-directions in the images are used. The temperature obtained from the two directions agree to within the error given here. The spread in the temperature at each data point may be due to the day to day fluctuations in the alignment and the polarization phase difference among the MOT laser beams.

As expected, the temperature is linearly dependent on intensity for $I/I_s > 25$, but the temperature increases much more rapidly than expected from Equation 8.5. For the detuning shown here, the temperature of ^{174}Yb rises 17 times more rapidly. The data presented

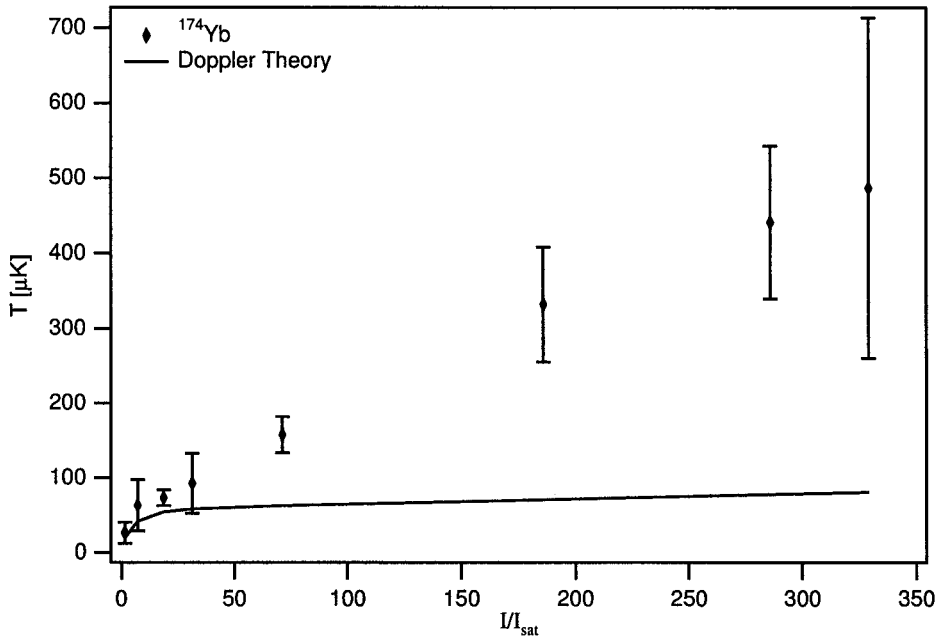

Figure 8.13: Trap temperature versus normalized trap-laser intensity, I/I_s, at $\delta = -13\gamma$ in ^{174}Yb. The solid line shows the temperature calculated from Doppler cooling theory including the displacement in position of the cloud due to gravity. The error bars represent the standard deviation of the mean of 2–10 measurements at a given intensity.

for the temperature of ^{88}Sr in Ref. [Xu02] obtained in a $\sigma^+-\sigma^-$ MOT configuration for the $^1S_0$–$^1P_1$ transition rises at a similarly rapid rate of 14 times that of Equation 8.5. Similar behavior was also seen in the other even isotopes of Yb: ^{170}Yb, ^{172}Yb, and ^{176}Yb. The number of trapped ^{168}Yb atoms was too small to make temperature measurements. At the lowest intensities gravity affects the atom equilibrium position and changes the behavior of the MOT. The effects of gravity are included in the theoretical prediction as discussed later in this section.

As mentioned in Section 3.3, the atoms in a MOT reaches a steady state temperature when the heating and cooling are balanced. The damping coefficient of the MOT was also measured for Sr by monitoring the time evolution of the cloud of atoms after displacing it from the center of the trap [Xu02]. They found that the damping coefficient is consistent with Doppler theory, thereby verifying that the higher temperature is due to excess

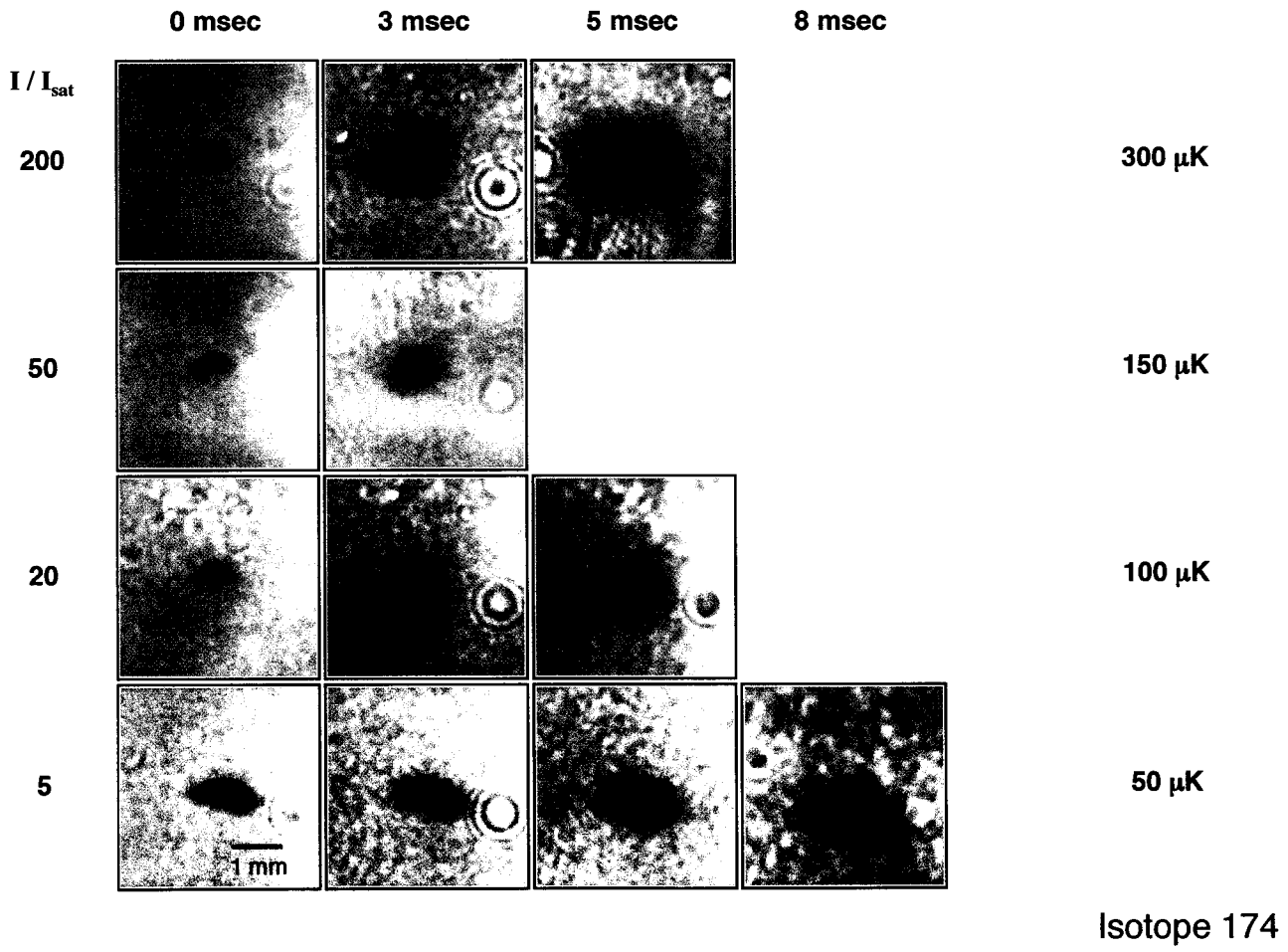

Figure 8.14: Time-of-flight images of isotope ^{174}Yb as intensity is varied.

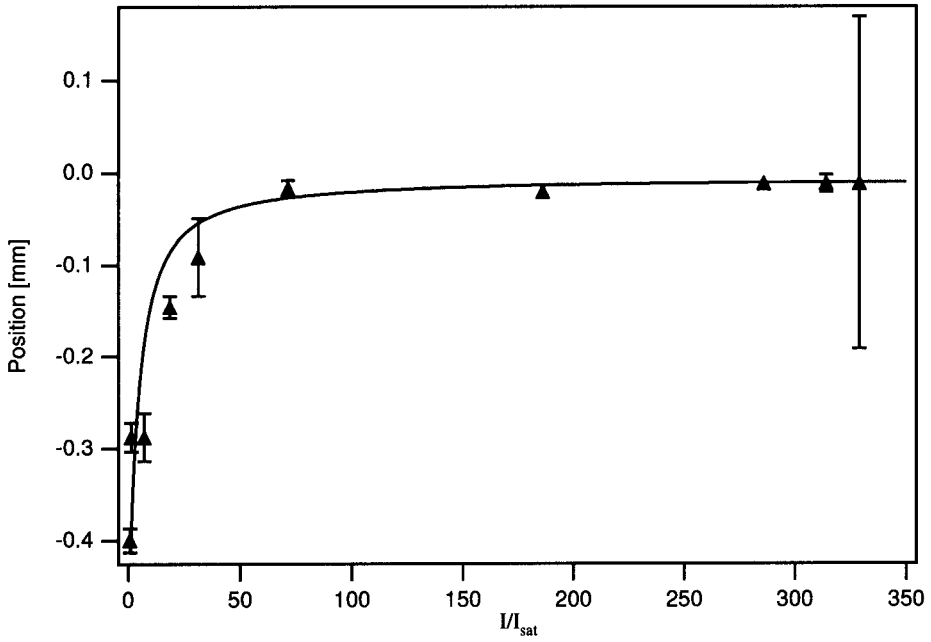

Figure 8.15: Vertical position of the ^{174}Yb cloud with respect to the center of the MOT of as a function of trap beam intensity. The solid line shows the calculated values of the location of the atoms that would balance the forces of light and gravity for the given detuning ($\delta = -13\gamma$), magnetic field gradient ($\partial B/\partial z = 16.5$ gauss) and intensity.

heating rather than insufficient cooling. A possible cause for the extra heating may be due to the localization of trapped atoms in the optical lattice set up by the 3D σ^+-σ^- laser configuration. For certain phase relations among the three orthogonal laser beams, the lattice shows intensity variations across the trap and for others, polarization gradients are present [Hop97]. It was also shown experimentally that atoms in a MOT are generally localized in light-shift potentials regardless of the relative phases among the MOT beams [Sch99]. Atoms localized in light-shift potentials experience, on average, higher laser intensities, resulting in higher temperature. In earlier experiments with the blue MOT, we found that it was crucial to carefully align the retro-reflected beams back onto themselves to achieve low temperatures. The existence of sub-Doppler cooling makes the more commonly studied alkali atom traps less sensitive to imbalances in the alignment and phase relations of the MOT beams [Wer93].

At low intensities, $I/I_s < 25$, the simple Doppler theory needs to be modified to include the effects of gravity. We found that the vertical position of the clouds drops with decreasing light intensity (see Figure 8.15) and the temperature seen in Figure 8.13 deviates from the linear dependence with intensity.

Because this line is weak, the force of gravity on the atoms is comparable to the force from the trap beams at lower intensities, especially at the large laser detuning used here ($\delta = -13\gamma$). For higher intensities, the force from the MOT beams are stronger and the effect of gravity is negligible. The force of the upward MOT beam is

$$F_{up} = \hbar k \frac{\gamma}{2} \frac{I/I_s}{1 + I_t/I_s + (2\delta_+/\gamma)^2} \tag{8.6}$$

where for atoms displaced vertically by a distance z_0 away from the center, the effective detuning is $\delta_+ = \delta + \frac{\partial B_z}{\partial z} z_0 \mu_g g_J$, and $\partial B_z/\partial z$ is the magnetic field gradient. I is the intensity of either of the vertical beams and I_t is the total intensity of all six beams that make up the trap. The downward force, F_{down}, has the same form except that δ_+ is replaced by $\delta_- = \delta - \frac{\partial B_z}{\partial z} z_0 \mu_g g_J$. Under gravity, the atoms find a new equilibrium position, z_0, which is slightly lower than the center, where forces are balanced: $F_{up} = F_{down} + mg$. The calculated vertical position of the cloud center is shown as a solid line in Figure 8.15 and is in good agreement with data.

The temperature of the trap including the vertical displacement is

$$T = \frac{\hbar\gamma}{8k_B} \left[\frac{\left(1 + \frac{I_t}{I_s} + 4\frac{\delta_-^2}{\gamma^2}\right)^{-1} + \left(1 + \frac{I_t}{I_s} + 4\frac{\delta_+^2}{\gamma^2}\right)^{-1}}{\frac{\delta_-}{\gamma}\left(1 + \frac{I_t}{I_s} + 4\frac{\delta_-^2}{\gamma^2}\right)^{-2} + \frac{\delta_+}{\gamma}\left(1 + \frac{I_t}{I_s} + 4\frac{\delta_+^2}{\gamma^2}\right)^{-2}} \right]. \tag{8.7}$$

The drop in the cloud center brings the effective detuning of the upward MOT beam closer to resonance, that is δ_+ is smaller. This results in a more efficient cooling and lower temperatures can be expected. This is included in the Doppler theory curve shown in Figure 8.13.

8.7 Odd Isotopes: Sub-Doppler Cooling

In contrast to the even isotopes, the odd isotopes have multiple sublevels in the ground state because of their nuclear spin. Having two isotopes with different spins ($I = 1/2$ and

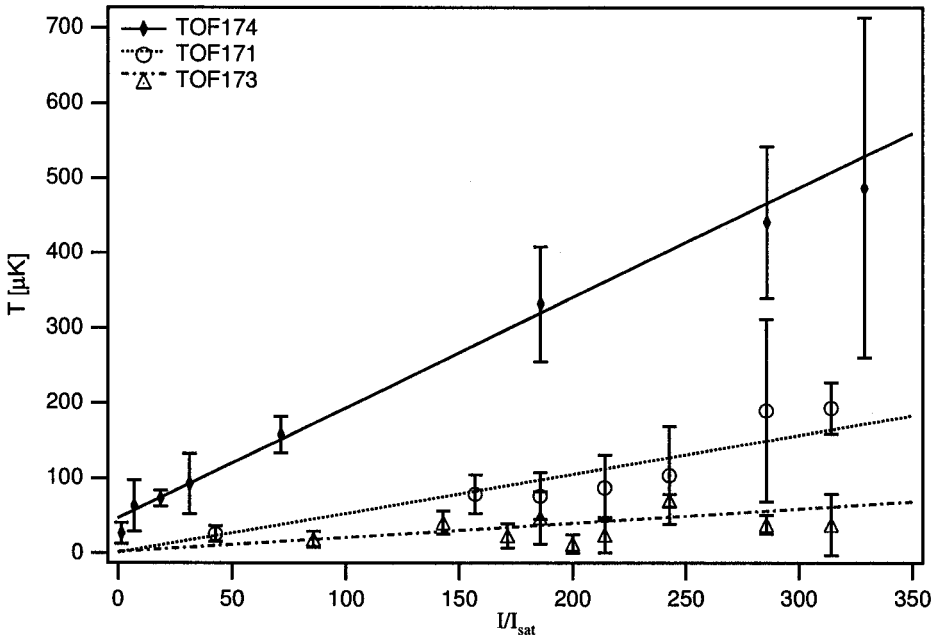

Figure 8.16: Temperature vs. I/I_s at $\delta = 13\gamma$ in ^{174}Yb, ^{171}Yb, and ^{173}Yb. The solid line shows a linear fit to the temperature of ^{174}Yb, dashed line for ^{171}Yb, and skip-dashed for ^{173}Yb.

5/2) makes it possible to isolate the dependence of cooling on the ground state angular momentum.

Figure 8.16 shows the temperature measured for isotopes ^{174}Yb, ^{171}Yb, and ^{173}Yb as a function of intensity. Figure 8.17 shows examples of time-of-flight images for two even isotopes (^{172}Yb and ^{174}Yb) and the odd isotopes (^{171}Yb and ^{173}Yb) at $I/I_s = 300$ and $\delta = -13\gamma$. These figures show that more efficient cooling is seen in isotopes with larger nuclear spin. Numerical simulations for lin $\perp$ lin configuration in 3-dimensions have shown that for $J_g \rightarrow J_e = J_g + 1$ transitions, the cooling is more efficient for isotopes with higher J_g, where temperature was calculated for systems with $J_g = 1, 2, 3, 4$ [Cas95]. For $|\delta| \gg \gamma$ and $I \gg I_s$, the temperature changes linearly with intensity, and can be expressed as

$$3k_B T/2 \simeq a(\hbar|\delta|s/2) + bE_{Rec}, \tag{8.8}$$

where $s = (1 + (2\delta/\gamma)^2)^{-1} I/I_s$ is the saturation parameter. Put in this form, the slope, a,

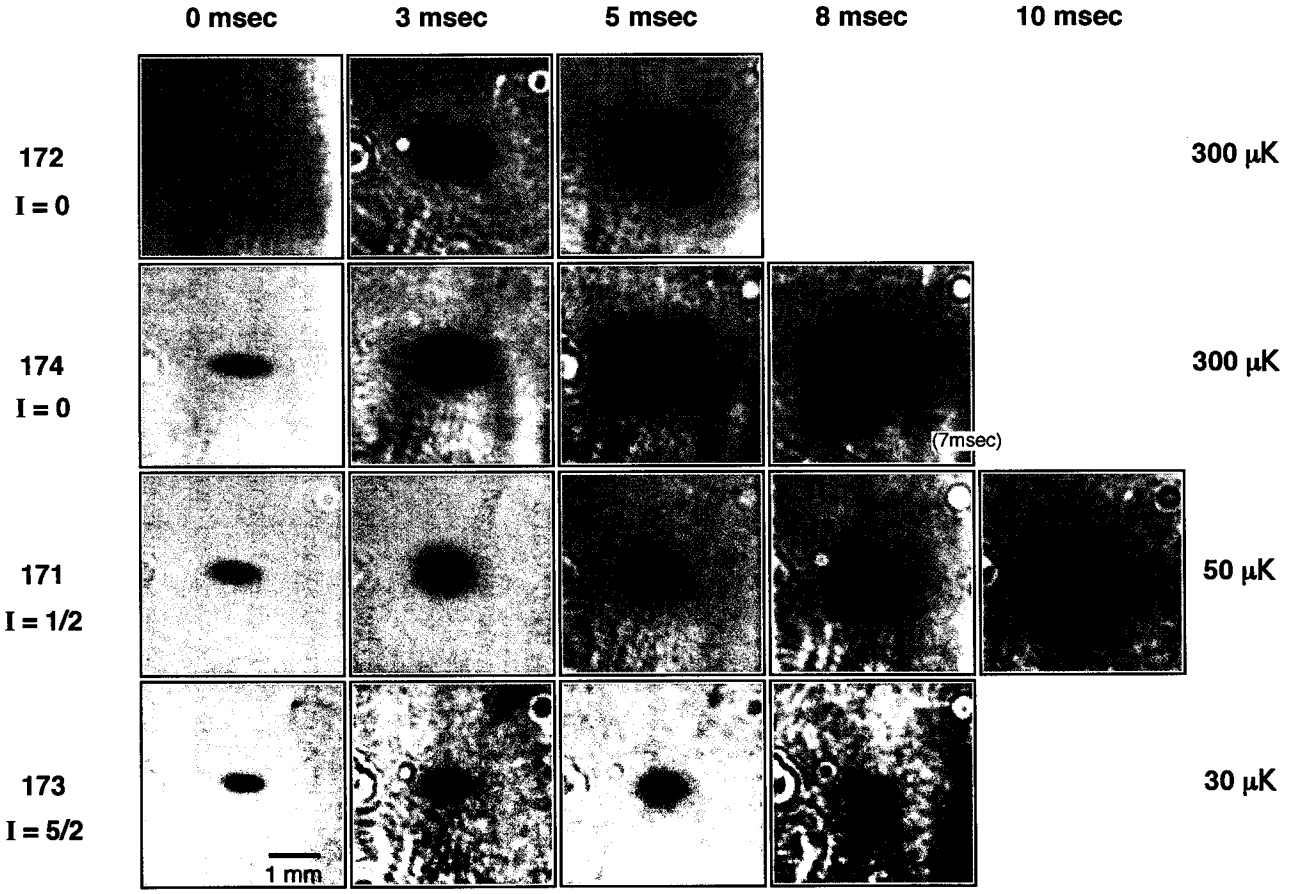

Figure 8.17: Time of Flight images of isotopes ^{172}Yb, ^{174}Yb, ^{171}Yb, and ^{173}Yb at $I/I_{sat} = 300$ and $\Delta = 13\Gamma$.

Table 8.1: Slope, a, from previous works and in the TOF measurements for the three Yb isotopes shown in Figs. 8.16 and 8.18. The errors represent the standard deviation of the mean of 2–10 measurements at a given intensity.

J_g	Calculated Slope [Cas95]	Measured Slope
0	(not available)	26 ± 4.3 (this work)
1/2	(not available)	9.0 ± 1.7 (this work)
1	3.3 ± 0.5	(not available)
2	2.6 ± 0.2	2.3 ± 0.2 [Ger93]
5/2	(not available)	3.3 ± 1.2 (this work)
3	2.5 ± 0.2	2.1 ± 0.2 [Ger93]
4	2.1 ± 0.2	2.1 ± 0.5 [Sal90]

and the offset scaling, b, depend only on the ground state angular momentum, J_g (in our case, F_g), and is independent of the mass, transition wavelength, or detuning. The values of a calculated in Ref. [Cas95] are in good agreement with experimental results from ^{87}Rb and ^{85}Rb ($J_g = 2$ and 3 respectively) [Ger93] and ^{133}Cs ($J_g = 4$) [Sal90]. In a MOT configuration with σ^+–σ^- polarization and magnetic quadrupole field gradient, the slope a was found to be 30% higher [Wal94].

It was shown in Ref. [Ger93] that the localization of atoms must be taken into account to correctly predict the temperature of atoms in a molasses in lin $\perp$ lin configuration. Although the lin $\perp$ lin and σ^+–σ^- configurations have markedly different polarization patterns in 3D, the degree of Sisyphus coupling averaged over the relative phase of the three orthogonal MOT beams has been shown to be similar to within a few percent for the two configurations [Hop97]. It has also been shown experimentally that both configurations have strong 3D localization effects for an arbitrary relative phase among the beams, and the influence of the phase variation on localization of atoms is small [Sch99].

Table 8.1 and Figure 8.18 summarize the slopes of normalized temperature versus cooling laser intensity. Figure 8.18 shows the temperature vs. I/I_s for ^{171}Yb and ^{173}Yb with

normalized axes. The colored lines show the calculated values for $J_g = 1$ through 4 [Cas95]. The grayed out regions in Figure 8.18 show the error of the linear fit to the data as denoted in Table 8.1. Although temperatures for $J_g = 5/2$ were not calculated in Ref. [Cas95], our result on ^{173}Yb isotope agrees within the error with the general trend in its dependence on angular momentum in the lin $\perp$ lin case. Our result is also consistent with the 30% higher temperature observed in a Rb MOT [Wal94]. In ^{171}Yb, we observe a slope that is nearly three times higher than in ^{173}Yb. Sisyphus cooling with $F_g < 1$ has not been measured previously. No alkali atom has $F_g < 1$, and it is an especially interesting case since the corkscrew cooling described in subsection 3.4.2 is absent. It will be interesting to investigate the cooling on this isotope with a controlled polarization of the cooling beams.

The sources that contribute to uncertainty in the slope a such as laser linewidth, optical pumping, and Zeeman shifts by the MOT fields are small compared to the quoted errors. The expansion measured in the x- and z-directions of the cloud give temperatures that are consistent to within the error. We attribute the large error to drifts in the long-term frequency lock of the green laser and variations in the phase relations among the MOT beams from day to day which depend on the alignment of the beams.

8.8 Determining the Temperature from the Cloud Size

As an independent check of the time-of-flight measurement, we use the size of the trapped clouds to measure the temperature. Equipartition theorem states that

$$k_B T = \kappa \langle \sigma_i^2 \rangle, \tag{8.9}$$

where the spring constant of the MOT in the x-direction, κ_x, for the simple Doppler-cooling theory is given by [Xu02]

$$\kappa_x = \frac{8}{\lambda} \mu_B g_J \frac{\partial B}{\partial x} \frac{\delta}{\gamma} \frac{I_x}{I_s} \left(1 + \frac{I}{I_s} + 4\frac{\delta^2}{\gamma^2} \right)^{-2}. \tag{8.10}$$

Here $\partial B/\partial x$ is the magnetic field gradient of the MOT, μ_B is the Bohr magnetron, and g_J is the gyro-magnetic ratio of the transition. For the $^1S_0$–$^3P_1$ transition, $g_J = 1.493$. In the magnetic quadrupole field, the gradient along the axis of the coils, z-direction, is

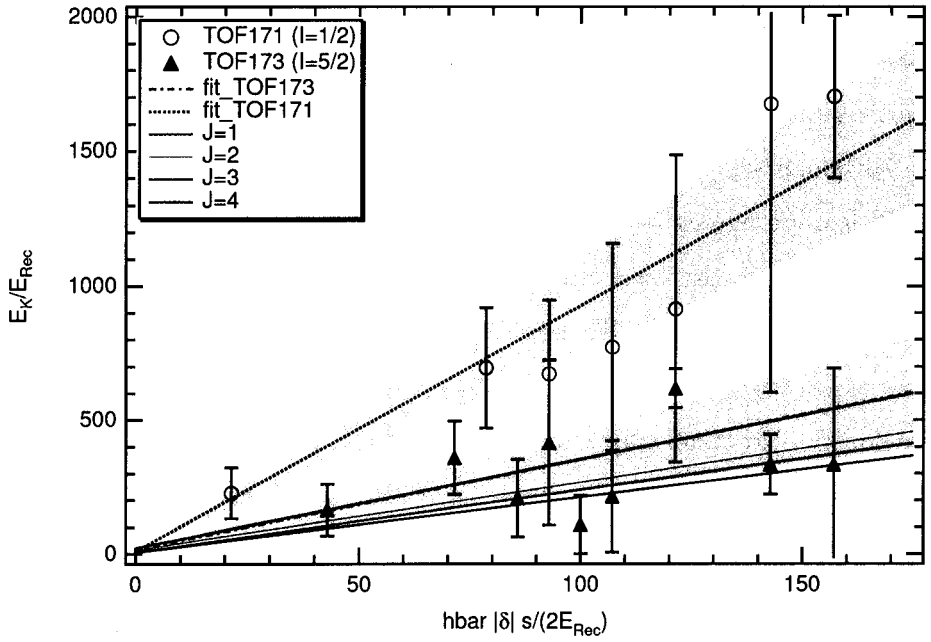

Figure 8.18: Temperature vs. I/I_s at $\delta = 13\gamma$ in ^{171}Yb and ^{173}Yb in normalized units. The dashed line shows a linear fit to the temperature of ^{171}Yb, and skip-dashed for ^{173}Yb, with the error of the fit of the slope shown in gray region. The colored lines are the predicted lines for $J_g = 1$ through 4 from Ref. [Cas95].

twice as strong as the transverse gradient in the x-direction: $\partial B/\partial z = 2\partial B/\partial x$. We also have intensity that is twice as strong along z, that is, $I_z = 2I_x$. This results in different spring constants between the vertical and horizontal directions, $\kappa_z = 4\kappa_x$, and the clouds are flattened vertically: $\sigma_x = 2\sigma_z$.

Figures 8.19, 8.20, and 8.21 show the temperature extracted from the initial size, σ_i, and the spring constant calculated from Equation 8.10 for ^{174}Yb, ^{171}Yb and ^{173}Yb. The temperatures measured from the time-of-flight method is also included for comparison.

The temperatures from the two different methods agree well in the case of ^{174}Yb, indicating that the spring constant calculated from the simple Doppler cooling theory for two-level system is accurate. The temperatures of the odd isotopes do not agree as well, and the spring constant for these isotopes need to be better understood. Optical pumping among the ground state sublevels and the smaller energy separation between the adjacent sublevels in the upper state are certainly playing a role.

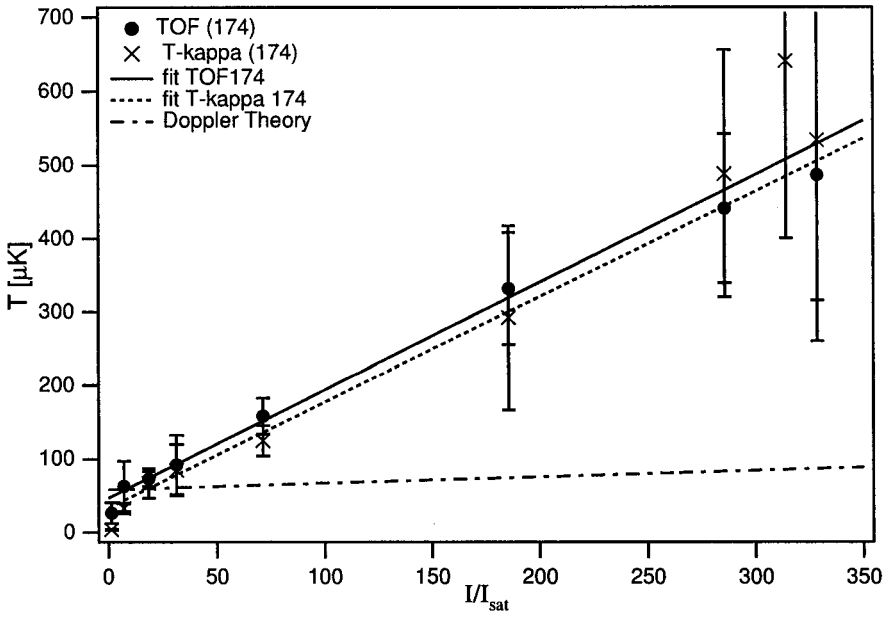

Figure 8.19: Temperature vs. intensity for ^{174}Yb measured by TOF (filled circle) and MOT spring constant ($\times$).

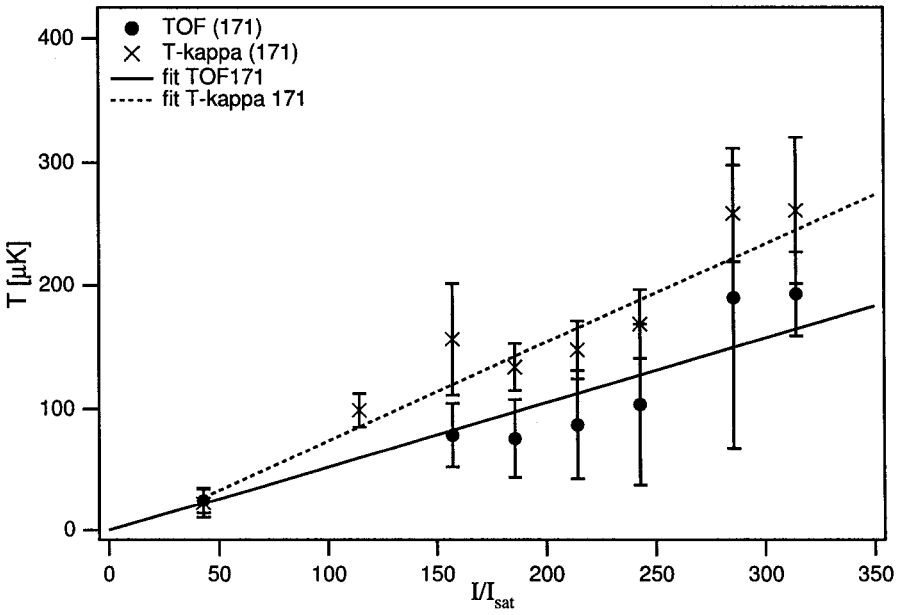

Figure 8.20: Temperature vs. intensity: ^{171}Yb measured by TOF (filled circle) and MOT spring constant ($\times$).

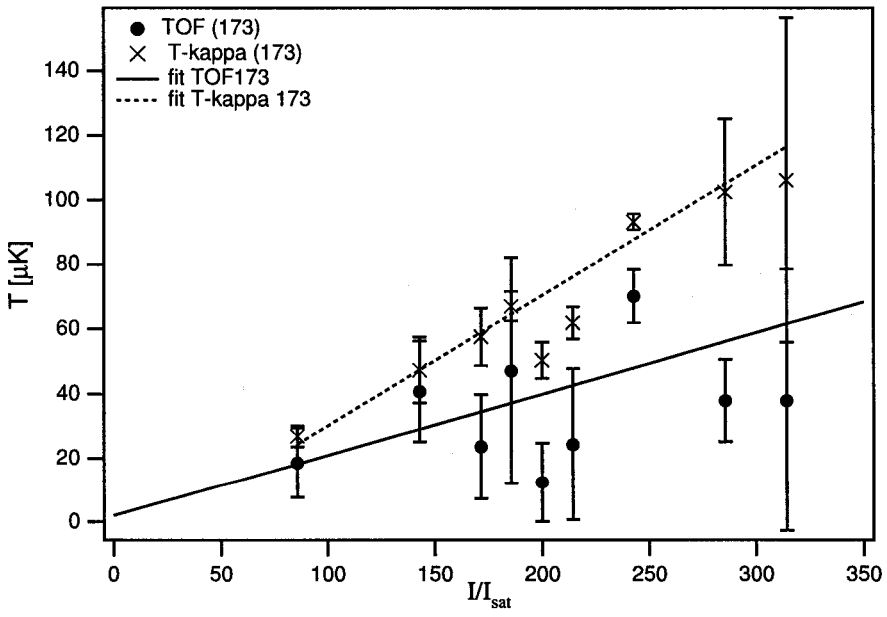

Figure 8.21: Temperature vs. intensity: ^{173}Yb measured by TOF (filled circle) and MOT spring constant ($\times$).

Chapter 9

CONCLUSIONS

In conclusion, we have cooled and trapped all seven isotopes of ytterbium using two separate transitions, $^1S_0$–$^1P_1$ and $^1S_0$–$^3P_1$. A complete experimental setup including a vacuum chamber that houses the atomic beam, Zeeman slower, and magneto-optical trap and lasers used for cooling and trapping was designed and assembled. A detection system for monitoring atom fluorescence was developed, and absorption and fluorescence imaging were used. Image analysis procedures were developed to measure the temperature, atom density distribution, and the total number of atoms.

Properties of the blue and green traps were investigated. Details of Doppler cooling have been studied for the first time in ytterbium, and Sisyphus cooling of atoms with only nuclear angular momentum but no electron angular momentum in the ground state has been observed.

This experiment has come a long way since its inception as a preliminary study on the feasibility of conducting an atomic EDM search with trapped diamagnetic atoms. In the process of immersing ourselves in the rapidly growing field of cold atoms, we have come across other possible experiments and applications for trapped ytterbium atoms. Cooling and trapping mechanisms of Yb have been studied and the apparatus is ready to be applied toward precision experiments. Some of the possible improvements to the system are described in the appendices.

BIBLIOGRAPHY

[Aba01] A. Abashian et al. "Measurement of the CP violation parameter sin2ϕ_1 in B_d^0 meson decays." Phys. Rev. Lett. **86**, 2509–2514, 2001.

[Abr95] E. R. I. Abraham, W. I. McAlexander, C. A. Sackett, and R. G. Hulet. "Spectroscopic Determination of the s-Wave Scattering Length of Lithium." Phys. Rev. Lett. **74**(8), 1315, February 1995.

[Abr96] E. R. I. Abraham, W. I. McAlexander, J. M. Gerton, R. G. Hulet, R. Côté, and A. Dalgarno. "Singlet s-wave scattering lengths of ^{6}Li and ^{7}Li." Phys. Rev. A **53**, R3713, 1996.

[And95] M. H. Anderson, J. R. Ensher, M. R. Matthews, C. E. Wieman, and E. A. Cornell. "Observation of Bose-Einstein Condensation in a Dilute Atomic Vapor Observation of Bose-Einstein Condensation in a Dilute Atomic Vapor Observation of Bose-Einstein Condensation in a Dilute Atomic Vapor." Science **269**, 198, July 1995.

[Ari92] E. Arimondo, W. Phillips, and F. Strumia, editors. *1991 International School of Physics Enrico Fermi: Laser Manipulation of Atoms and Ions: Varenna on Lake Como, Villa Monastero, 9-19 July 1991.* North-Holland, Amsterdam; New York, 1992.

[Ash78] A. Ashkin. "Trapping of Atoms by Resonance Radiation Pressure." Phys. Rev. Lett. **40**(12), 729, March 1978.

[Asp89] A. Aspect, E. Arimondo, R. Kaiser, N. Vansteenkiste, and C. Cohen-Tannoudji. "Laser cooling below the one-photon recoil energy by velocity-selective coher-

ent population trapping: theoretical analysis." J. Opt. Soc. Am. B **6**(11), 2112, November 1989.

[Aub01] B. Aubert et al. "Measurement of CP-violating asymmetries in B^0 decays to CP eigenstates." Phys. Rev. Lett. **86**(12), 2515–2522, 2001.

[Bag93] V. S. Bagnato, L. G. Marcassa, M. Oria, G. I. Surdotovich, R. Vitlina, and S. C. Zilio. "Spatial distribution of atoms in a magneto-optical trap." Phys. Rev. A **48**(5), 3771, November 1993.

[Bar93a] Roger Barlow. *Statistics: A Guide to the Use of Statistical Methods in the Physical Sciences.* Wiley, John & Sons, Incorporated, 1993.

[Bar93b] S. M. Barr. "A review of CP violation in atoms." Int. J. Mod. Phys. A **8**(2), 209–236, 1993.

[Bar01] M. D. Barrett, J. A. Sauer, and M. S. Chapman. "All-optical formation of an atomic Bose-Einstein condensate." Phys. Rev. Lett. **87**(1), 010404, July 2001.

[Beh97] J. A. Behr et al. "Magneto-optic Trapping of Beta-Decaying $^{38}K^m$, ^{37}K from an on-line Isotope Separator." Phys. Rev. Lett. **79**(3), 375, July 1997.

[Ber91] Werner Bernreuther and Makiko Suzuki. "The electric dipole moment of the electron." Rev. Mod. Phys **63**(2), 313, April 1991.

[Bev92] Philip R. Bevington and D. Keith Robinson. *Data Reduction and Error Analysis for the Physical Sciences.* WCB/McGraw-Hill, 2nd edition, 1992.

[Bij94] M. Bijlsma and B. J. Verhaar. "Role of collisions in the search for an electron electric-dipole moment." Phys. Rev. A **49**(6), R4285, June 1994.

[Bla78] K. B. Blagoev, V. A. Komarovskii, and N. P. Penkin. "Radiative lifetimes of Yb_I Yb_{II} excited states." Opt. Spectrosc. (USSR) **45**(5), 832, 1978.

[Bla94] K. B. Blagoev and V. A. Komarovskii. "Lifetimes of Levels of Neutral and Singly Ionized Lanthanide Atoms." Atomic Data and Nuclear Data Tables **56**(1), 1–40, 1994.

[Bow96] C. J. Bowers, D. Budker, E. D. Commins, D. DeMille, S. J. Freedman, A.-T. Nguyen, and S.-Q. Shang. "Experimental investigation of excited-state lifetimes in atomic ytterbium." Phys. Rev. A **53**(5), 3103, May 1996.

[Bow98] Christopher Jonathan Bowers. *Experimental Investigation of the* $6s^{2/1}S_0 \rightarrow 5d6s^3D_1$ *Forbidden Transition in Atomic Ytterbium.* PhD thesis, University of California at Berkeley, 1998.

[Bow99] C. J. Bowers, D. Budker, S. J. Freedman, G. Gwinner, and J. E. Stalnaker. "Experimental investigation of the $6s^2\ ^1S_0 \rightarrow 6s5d^3D_{1,2}$ forbidden transitions in atomic ytterbium." Phys. Rev. A **59**(5), 3513, May 1999.

[Boy68] G. D. Boyd and D. A. Kleinman. "Parametric Interaction of Focused Gaussian Light Beams." Journal of Applied Physics **39**(8), 3597– 3639, July 1968.

[Boy96] R. A. Boyd, J. L. Bliss, and K. G. Libbrecht. "Teaching physics with 670-nm diode lasers – experiments with Fabry-Perot cavities." American Journal of Physics **64**(9), 1109, September 1996.

[Bra95] C. C. Bradley, C. A. Sackett, J. J. Tollett, and R. G. Hulet. "Evidence of Bose-Einstein Condensation in an Atomic Gas with Attractive Interactions." Phys. Rev. Lett. **75**(9), 1687, August 1995.

[Bur95] Eric A. Burt. *Demonstration of Trapped Single Laser Cooled Indium Ions.* PhD thesis, University of Washington, 1995.

[Cas] Castech. "http://www.castech.com/".

[Cas89] Y. Castin, H. Wallis, and J. Dalibard. "Limit of Doppler cooling." J. Opt. Soc. Am. B **6**(11), 2046, November 1989.

[Cas90] Yvan Castin and Klaus Mølmer. "Atomic momentum diffusion in a σ_+-σ_- laser configuration: influence of an internal sublevel structure." J. Phys. B **23**, 4101, 1990.

[Cas95] Yvan Castin and Klaus Mølmer. "Monte Carlo Wave-Function Analysis of 3D Optical Molasses." Phys. Rev. Lett. **74**(19), 3772, May 1995.

[Cha99] A. Chambers, R. K. Fitch, and B. S. Halliday. *Basic vacuum technology.* Institute of Physics Pub., Bristol; Philadelphia, 1999.

[Chr01] J. H. Christenson, J. W. Cronin, V. L. Fitch, and R. Turlay. "Evidence for the 2π decay of the K_2^0 meson." Phys. Rev. Lett. **13**(4), 138–140, 2001.

[Chu85] S. Chu, L. Hollberg, J. E. Bjorkholm, A. Cable, and A. Ashkin. "Three-Dimensional Viscous Confinement and Cooling of Atoms by Resonance Radiation Pressure." Phys. Rev. Lett. **55**(1), 48, July 1985.

[Chu86] Steven Chu, J. E. Bjorkholm, A. Ashkin, and A. Cable. "Experimental Observation of Optically Trapped Atoms." Phys. Rev. Lett. **57**(3), 314, July 1986.

[Cor77] Alan Corney. *Laser cooling and trapping.* Clarendon Press, Oxford; New York, 1977.

[Cor99] K. L. Corwin, S. J. M. Kuppens, D. Cho, and C. E. Wieman. "Spin-Polarized Atom in a Circularly Polarized Optical Dipole trap." Phys. Rev. Lett. **83**(7), 1311, August 1999.

[Cra00] S. G. Crane, X. Zhao, W. Taylor, and D. J. Vieira. "Trapping an isotopic mixture of fermionic ^{84}Rb and bosonic ^{87}Rb atoms." Phys. Rev. A **62**, 011402, July 2000.

[Cur01] E. A. Curtis, C. W. Oates, and L. Hollberg. "Quenched narrow-line laser cooling of ^{40}Ca to near the photon recoil limit." Phys. Rev. A **64**, 031403(R), 2001.

[Dal89] J. Dalibard and C. Cohen-Tannoudji. "Laser cooling below the Doppler limit by polarization gradients: simple theoretical models." J. Opt. Soc. Am. B **6**(11), 2023–2045, 1989.

[Das96] B. P. Das. "Computation of correlation effects on the parity-nonconserving electric-dipole transition in atomic ytterbium." Phys. Rev. A **56**(2), 1635, August 1996.

[Das02] B. P. Das. *private communication*, 2002.

[Dav95a] N. Davidson, H. J. Lee, C. S. Adams, M. Kasevich, and S. Chu. "Long Atomic Coherence Times in an Optical Dipole Trap." Phys. Rev. Lett. **74**(8), 1311, February 1995.

[Dav95b] K. B. Davis, M. O. Mewes, M. R. Andrews, N. J. van Druten, D. S. Durfee, D. M. Kurn, and W. Ketterle. "Bose-Einstein Condensation in a Gas of Sodium Atoms." Phys. Rev. Lett. **75**, 3969, November 1995.

[Dei93] K. Deilamian, J. D. Gialspy, and D. E. Kelleher. "Isotope shifts and hyperfine splittings of the 398.8-nm Yb I line." J. Opt. Soc. Am. B **10**(5), 789, May 1993.

[DeM95] David DeMille. "Parity Nonconservation in the $6s^2\ ^1S_0 \rightarrow 6s5d^3D_1$ Transition in Atomic Ytterbium." Phys. Rev. Lett. **74**(21), 4165, May 1995.

[DeM99] B. DeMarco and D. S. Jin. "Onset of Fermi Degeneracy in a Trapped Atomic Gas." Science **285**, 1703, September 1999.

[DeM00] D. DeMille, F. Bay, S. Bickman, D. Kawall, Jr. D. Krause, S. E. Maxell, and L. R. Hunter. "Investigation of PbO as a system for measuring the electric dipole moment of the electron." Phys. Rev. A **61**, 052507, 2000.

[Der01] Andrei Derevianko. "Feasibility of Cooling and Trapping Metastable Alkaline-Earth Atoms." Phys. Rev. Lett. **87**(2), 023002, July 2001.

[Din99] Timothy P. Dinneen, Kurt R. Vogel, Ennio Arimondo, John L. Hall, and Alan Gallagher. "Cold collisions of Sr*-Sr in a magneto-optical trap." Phys. Rev. A **59**(2), 1216, February 1999.

[Dre83] R. W. P. Drever, J. L. Hall, F. V. Kowalski, J. Hough, G. M. Ford, A. J. Munley, and H. Ward. "Laser phase and frequency stabilization using an optical resonator." Appl. Phys. B **31**(2), 97–105, June 1983.

[Gar95] J. R. Gardner, R. A. Cline, J. D. Miller, D. J. Heinzen, H. M. J. M. Boesten, and B. J. Verhaar. "Collisions of Doubly Spin-Polarized, Ultracold ^{85}Rb Atoms." Phys. Rev. Lett. **74**, 3764, 1995.

[Gen98] S. D. Gensemer and P. L. Gould. "Ultracold Collisions Observed in Real Time." Phys. Rev. Lett. **80**, 936939, 1998.

[Ger93] C. Gerz, T. W. Hodapp, P. Jessen, K. M. Jones, W. D. Phillips, C. I. Westbrook, and K. Mølmer. "The Temperature of Optical Molasses for Two Different Atomic Angular Momenta." Europhys. Lett. **21**(6), 661, February 1993.

[Gor00] A. Gorelov et al. "Beta-neutrino correlation experiments on laser trapped ^{38}K^{m}, ^{37}K." Hyperfine Interactions **127**, 373, August 2000.

[Gra02] S. R. Granade, M. E. Gehm, K. M. O'Hara, and J. E. Thomas. "All-optical production of a degenerate Fermi gas." Phys. Rev. Lett. **88**(12), 120405, March 2002.

[Grü02] Jan Grünert and Andreas Hemmerich. "Sub-Doppler magneto-optical trap for calcium." Phys. Rev. A **65**, 041401(R), 2002.

[Gue94] I. Guedes, M. T. de Araujo, D. M. B. Milori, G. I. Surdotovich, V. S. Bagnato, and S. C. Zilio. "Forces acting on magneto-optically trapped atoms." J. Opt. Soc. Am. B **11**(10), 1935–1940, October 1994.

[Hä75] T. W. Hänsch and A. L. Shawlow. "Cooling of Gases by Laser Radiation." Opt. Commun. **13**(1), 68, January 1975.

[Han80] T. W. Hansch and B. Couillaud. "Laser frequency stabilization by polarization spectroscopy of a reflecting reference cavity." Opt. Commun. **35**(3), 441–4, December 1980.

[Han03] Dirk P. Hansen, Janis R. Mohr, and Andreas Hemmerich. "Magnetic trapping of metastable calcium atoms." Phys. Rev. A **67**, 021401(R), February 2003.

[Hin97] E. A. Hinds. "Testing Time Reversal Symmetry Using Molecules." Physica Scripta **T70**, 34, 1997.

[Hol01] L. Hollberg, C. W. Oates, E. A. Curtis, E. N. Ivanov, S. A. Diddams, T. Udem, H. G. Robinson, J. C. Bergquist, R. J. Rafac, W. M. Itano, R. E. Drullinger, and D. J. Wineland. "Optical Frequency Standards and Measurements." IEEE J. Quantum Electron. **37**(12), 1502, December 2001.

[Hon99] K. Honda, Y. Takahashi, T. Kuwamoto, M. Fujimoto, and K. Toyoda. "Magneto-optical trapping of Yb atoms and a limit on the branching ratio of the $^1P_1$ state." Phys. Rev. A **59**(2), R934, February 1999.

[Hon02] K. Honda, Y. Takasu, T. Kuwamoto, M. Kumakura, Y. Takahashi, and T. Yabuzaki. "Optical dipole force trapping of a fermion-boson mixture of ytterbium isotopes." Phys. Rev. A **66**, 021401(R), 2002.

[Hop97] S. A. Hopkins and A. V. Durrant. "Parameters for polarization gradients in three-dimensional electromagnetic standing waves." Phys. Rev. A **56**(5), 4012, November 1997.

[Hud02] J. J. Hudson, B. E. Sauer, M. R. Tarbutt, and E. A. Hinds. "Measurement of the electron electric dipole moment using YbF molecules." Phys. Rev. Lett. **89**(2), 023003, July 2002.

[Ido00] Tetsuya Ido, Yoshitomo Isoya, and Hidetoshi Katori. "Optical-dipole trapping of Sr atoms at a high phase-space density." Phys. Rev. A **61**, 061403(R), 2000.

[Jac93] J. P. Jacobs, W. M. Klipstein, S. K. Lamoreaux, B. R. Heckel, and E. N. Fortson. "Testing time-reversal symmetry using ^{199}Hg." Phys. Rev. Lett. **71**(23), 3782, December 1993.

[Jac95] J. P. Jacobs, W. M. Klipstein, S. K. Lamoreaux, B. R. Heckel, and E. N. Fortson. "Limit on the electric-dipole moment of ^{199}Hg using synchronous optical pumping." Phys. Rev. A **52**(5), 3521, November 1995.

[Jon96] K. M. Jones, P. S. Julienne, P. D. Lett, W. D. Phillips, E. Tiesinga, and C. J. Williams. "Measurement of the atomic lifetime and of retardation in the interaction between two atoms bound in a molecule." Europhys. Lett. **35**, 85, 1996.

[Jul93] P. S. Julienne, A. M. Smith, and K. Burnett. Adv. At., Mol., Opt. Phys. **30**, 141, 1993.

[Jur02] E. Jurdik, J. Hohlfeld, A. F. van Etteger, A. J. Toonen, W. L. Meerts, H. van Kempen, and Th. Rasing. "Performance optimization of an external enhancement resonator for optical second-harmonic generation." J. Opt. Soc. Am. B **19**(7), 1660, July 2002.

[Kat99a] H. Katori, T. Ido, and M. Kuwata-Gonokami. "Optimal Design of Dipole Potentials for Efficient Loading of Sr Atoms." J. Phys. Soc. Japan **68**(8), 2479, August 1999.

[Kat99b] Hidetoshi Katori, Tetsuya Ido, Yoshitomo Isoya, and Makoto Kuwata-Gonokami. "Magneto-Optical Trapping and Cooling of Strontium Atoms down to the Photon Recoil Temperature." Phys. Rev. Lett. **82**(6), 1116, February 1999.

[Khr97] Iosif B. Khriplovich and Steve K. Lamoreaux. *CP violation without strangeness: electric dipole moments of particles, atoms, and molecules.* Springer-Verlag, Berlin; New York, 1997.

[Kis94] Th. Kisters, K. Zeiske, F. Riehle, and J. Helmcke. "High-resolution spectroscopy with laser-cooled and trapped calcium atoms." Applied Physics B **59**, 89–98, 1994.

[Kli96a] W. M. Klipstein, S. K. Lamoreaux, and E. N. Fortson. "Observation of spontaneous spin polarization in an optically pumped cesium vapor." Phys. Rev. Lett. **76**, 2266, 1996.

[Kli96b] William M. Klipstein. *Constraints on Time Reversal Symmetry Violation from a New Limit on the Permanent Electric Dipole Moment of Mercury 199, and Observation of Spontaneous Atomic Spin Polarization in Cesium.* PhD thesis, University of Washington, 1996.

[Kum01] Hiroshi Kumagai, Yuichi Asakawa, Takeshi Fujii, Katsumi Midorikawa, and Minoru Obara. "High-power deep-UV cw coherent light source for laser cooling of silicon atoms." RIKEN Review **33**, 3, March 2001.

[Kup00] S. J. M. Kuppens, K. L. Corwin, K. W. Miller, T. E. Chupp, and C. E. Wieman. "Loading an optical dipole trap." Phys. Rev. A **62**, 013406, 2000.

[Kur98] T. Kurosu, G. Zinner, T. Trebst, and F. Riehle. "Method for quantum-limited detection of narrow-linewidth transitions in cold atomic ensembles." Phys. Rev. A **58**(6), R4275, December 1998.

[Kuw99] T. Kuwamoto, K. Honda, Y. Takahashi, and T. Yabuzaki. "Magneto-optical trapping of Yb atoms using an intercombination transition." Phys. Rev. A **60**(2), R745, August 1999.

[Lam02] S. K. Lamoreaux. "Solid-state systems for the electron electric dipole moment and other fundamental measurements." Phys. Rev. A **66**, 022109, 2002.

[Let88] P. D. Lett, R. N. Watts, C. I. Westbrook, and W. D. Phillips. "Observation of Atoms Laser Cooled below the Doppler Limit." Phys. Rev. Lett. **61**, 169, July 1988.

[Let89] P. D. Lett, W. D. Phillips, S. L. Rolston, E. C. Tanner, R. N. Watts, and C. I. Westbrook. "Optical molasses." J. Opt. Soc. Am. B **6**(11), 2084, November 1989.

[Let95] P. D. Lett, K. Molmer, S. D. Gensemer, K. Y. N. Tan, A. Kumarakrishnan, C. D. Wallace, and P. L. Gould. "Hyperfine structure modifications of collisional losses from light-force atom traps." J. Phys. B **28**, 65–81, 1995.

[Lid02] David R. Lide, editor. *CRC Handbook of Chemistry and Physics.* CRC Press, Boca Raton, FL, 83rd edition, 2002.

[Lof00a] T. Loftus, J. R. Bochinski, and T. W. Mossberg. "Probing magneto-optic trap dynamics through weak excitation of a coupled narrow-linewidth transition." Phys. Rev. A **61**, 061401(R), 2000.

[Lof00b] T. Loftus, J. R. Bochinski, R. Shivitz, and T. W. Mossberg. "Power-dependent loss from an ytterbium magneto-optic trap." Phys. Rev. A **61**, 051401(R), 2000.

[Lof01a] T. Loftus, J. R. Bochinski, and T. W. Mossberg. "Optical double-resonance cooled-atom spectroscopy." Phys. Rev. A **63**, 023402, 2001.

[Lof01b] T. Loftus, J. R. Bochinski, and T. W. Mossberg. "Simultaneous multi-isotope trapping of ytterbium." Phys. Rev. A **63**, 053401, 2001.

[Lof01c] Thomas Howard Loftus. *Laser Cooling and Trapping of Atomic Ytterbium.* PhD thesis, University of Oregon, 2001.

[Lof02a] T. Loftus, J. R. Bochinski, and T. W. Mossberg. "Magnetic trapping of ytterbium and the alkaline-earth metals." Phys. Rev. A **66**, 013411, 2002.

[Lof02b] Thomas H. Loftus. *private communication*, 2002.

[Mac99] M. Machholm, P. S. Julienne, and K. A. Suominen. "Collisions of cold magnesium atoms in a weak laser field." Phys. Rev. A **59**(6), R4113, June 1999.

[Mac01] Mette Machholm, Paul S. Julienne, and Kalle-Antti Suominen. "Calculations of collisions betwen cold alkaline-earth-metal atoms in a weak laser field." Phys. Rev. A **64**, 033425, 2001.

[Mac02] M. Machholm, P. S. Julienne, and K. A. Suominen. "Subthermal linewidths in photoassociation spectra of cold alkaline-earth-metal atoms." Phys. Rev. A **65**, 023401, 2002.

[Mad02] D. N. Madsen and J. W. Thomsen. "Measurement of absolute photo-ionization cross sections using magnesium magneto-optical traps." J. Phys. B **35**, 2173, 2002.

[Mar78] W. C. Martin, Romuald Zalubas, and Lucy Hagan. *Atomic Energy Levels : the Rare-Earth Elements.* National Bureau of Standards, 1978.

[Mar93] L. Marcassa, V. Bagnato, Y. Wang, C. Tsao, J. Weiner, O. Dulieu, Y. B. Band, and P. S. Julienne. "Collisional loss rate in a magneto-optical trap for sodium atoms: Light-intensity dependence." Phys. Rev. A **47**, R4563, 1993.

[McA95] W. I. McAlexander, E. R. I. Abraham, N. W. M. Ritchie, C. J. Williams, H. T. C. Stoof, and R. G. Hulet. "Precise atomic radiative lifetime via photoassociative spectroscopy of ultracold lithium." Phys. Rev. A **51**, R871, 1995.

[Met99] Harold J. Metcalf and Peter van der Straten. *Laser cooling and trapping.* Springer, New York, 1999.

[Mig91] J. Migdalek and W. E. Baylis. "Relative transition probabilities and lifetimes of low-lying levels in ytterbium." Journal of Physics B **24**, L99–L102, 1991.

[Mil93] J. D. Miller, R. A. Cline, and D. J. Heinzen. "Far-off-resonance optical trapping of atoms." Phys. Rev. A **47**(6), R4567, June 1993.

[Møl91] Klaus Mølmer. "Friction and diffusion coefficients for cooling of atoms in laser fields with multidimensional periodicity." Phys. Rev. A **44**(9), 5820, November 1991.

[Møl02] Klaus Mølmer, 2002. *private communication.*

[Mur89] S. A. Murthy, D. Krause Jr., Z. L. Li, and L. R. Hunter. "New limits on the electron electric dipole moment from cesium." Phys. Rev. Lett. **63**, 965, 1989.

[Nag03] S. B. Nagel, C. E. Simien, S. Laha, P. Gupta, V. S. Ashoka, and T. C. Killian. "Magnetic trapping of metastable $^3P_2$ atomic strontium." Phys. Rev. A **67**, 011401(R), 2003.

[New96] N. R. Newbury and C. Wieman. "Resource Letter TNA-1: Trapping of neutral atoms." Am. J. Phys. **64**(1), 18–20, January 1996.

[Oat99] C. W. Oates, F. Bondu, R. W. Fox, and L. Hollberg. "A diode-laser optical frequency standard based on laser-cooled Ca atoms: Sub-kilohertz spectroscopy by optical shelving detection." Eur. Phys. J. D **7**, 449, 1999.

[O'H99] K. M. O'Hara, S. R. Granade, M. E. Gehm, T. A. Savard, S. Bali, C. Freed, and J. E. Thomas. "Ultrastable CO_2 laser trapping of lithium fermions." Phys. Rev. Lett. **82**(21), 4204, May 1999.

[Pet94] M. G. Peters, D. Hoffmann, J. D. Tobiason, and T. Walker. "Laser-induced ultracold $Rb(5S_{1/2})$+$Rb(5P_{1/2})$ collisions." Phys. Rev. A **50**, R906, 1994.

[Raa87] E. L. Raab, M. Prentiss, Alex Cable, Steven Chu, and D. E. Pritchard. "Trapping of Neutral Sodium Atoms with Radiation Pressure." Phys. Rev. Lett. **59**(23), 2631, December 1987.

[Ram56] Norman F. Ramsey. *Molecular Beams.* Oxford University Press, 1956.

[Reg02] B. C. Regan, E. D. Commins, C. J. Schmidt, and D. Demille. "New limit on the electron electric dipole moment." Phys. Rev. Lett. **88**(7), 071805, February 2002.

[Rob99] M. Roberts, P. Taylor, S. V. Gateva-Kostova, R. B. M. Clarke, W. R. C. Rowley, and P. Gill. "Measurement of the $^2S_{1/2}$-$^2D_{5/2}$ clock transition in a single $^{171}Yb^+$ ion." Phys. Rev. A **60**(4), 2867, Oct 1999.

[Rom99] M. V. Romalis and E. N. Fortson. "Zeeman frequency shifts in an optical dipole trap used to search for an electric-dipole moment." Phys. Rev. A **59**(6), 4547, June 1999.

[Rom01a] M. V. Romalis, W. C. Griffith, J. P. Jacobs, and E. N. Fortson. "New limits on the permanent electric dipole moment of ^{199}Hg." Phys. Rev. Lett. **86**(12), 2505, March 2001.

[Rom01b] M. V. Romalis and M. P. Letdbetter. "Transverse spin relaxation in liquid ^{129}Xe in the presence of large dipolar fields." Phys. Rev. Lett. **87**(6), 067601, 2001.

[Ros01] M. A. Rosenberry and T. E. Chupp. "Atomic electric dipole moment measurement using spin exchange pumped masers of ^{129}Xe and ^3He." Phys. Rev. Lett. **86**(1), 22, January 2001.

[Rus98] F. Ruschewitz, J. L. Peng, H. Hinderthür, N. Schaffrath, K. Sengstock, and W. Ertmer. "Sub-Kilohertz Optical Spectroscopy with a Time Domain Atom Interferometer." Phys. Rev. Lett. **80**(15), 3173, April 1998.

[Sal88] Ch. Salomon, D. Hils, and J. L. Hall. "Laser stabilization at the millihertz level." J. Opt. Soc. Am. B **5**(8), 1576 – 1587, August 1988.

[Sal90] C. Salomon, J. Dalibard, W. D. Phillips, A. Clairon, and S. Guellati. "Laser Cooling of Cesium Atoms below 3 μK." Europhys. Lett. **12**(8), 683, August 1990.

[San93] J. Sandberg. *Research Toward Laser Spectroscopy of Trapped Atomic Hydrogen.* PhD thesis, Massachusetts Institue of Technology, May 1993.

[Sau95] B. E. Sauer, Jun Wang, and E. A. Hinds. "Anomalous spin-rotation coupling in the $X^2\Sigma^+$ state of YbF." Phys. Rev. Lett. **74**(9), 1554, February 1995.

[Sau96] B. E. Sauer, Jun Wang, and E. A. Hinds. "Laser-rf double resonance spectroscopy of ^{174}YbF in the $X^2\Sigma^+$ state: Spin-rotation, hyperfine interactions, and the electric dipole moment." J. Chem. Phys. **105**(17), 7412, November 1996.

[Sav97] T. A. Savard, K. M. O'Hara, and J. E. Thomas. "Laser-noise-induced heating in far-off resonance optical traps." Phys. Rev. A **56**(2), 1095(R), August 1997.

[Sch96] H. Schnatz, B. Lipphardt, J. Helmcke, F. Riehle, and G. Zinner. "First Phase-Coherent Frequency Measurement of Visible Radiation." Phys. Rev. Lett. **76**(1), 18, January 1996.

[Sch99] H. Schadwinkel, U. Reiter, V. Gomer, and D. Meschede. "Magneto-optical trap as an optical lattice." Phys. Rev. A **61**, 013409, 1999.

[Sen94] K. Sengstock, U. Sterr, J. H. Müller, V. Rieger, D. Bettermann, and W. Ertmer. "Optical Ramsey spectroscopy on laser-trapped and thermal Mg atoms." Appl. Phys. B **59**, 99–115, 1994.

[Ses91] D. W. Sesko, T. G. Walker, and C. E. Wieman. "Behavior of neutral atoms in a spontaneous force trap." J. Opt. Soc. Am. B **8**(5), 946–958, May 1991.

[Sim96] J. E. Simsarian, A. Ghosh, G. Gwinner, L. A. Orozco, G. D. Sprouse, and P. A. Voytas. "Magneto-optic trapping of ^{210}Fr." Phys. Rev. Lett. **76**(19), 3522, 1996.

[Sob92] Igor I. Sobelman. *Atomic Spectra and Radiative Transitions.* Springer, 2nd edition, 1992.

[Spr02] G .D. Sprouse, S. Aubin, E. Gomez, J. S. Grossman, L. A. Orozco, M. R. Pearson, and M. True. "Atomic probes of electromagnetic and weak interactions with trapped radioactive atoms." Eur. Phys. J. A **13**, 239, 2002.

[Tak03] Y. Takasu, K. Honda, K. Komori, T. Kuwamoto, M. Kumamura, Y. Takahashi, and T. Yabuzaki. "High-Density Trapping of Cold Ytterbium Atoms by an Optical Dipole Force." Phys. Rev. Lett. **90**(2), 023003, January 2003.

[Tam00] C. Tamm, D. Engelke, and V. Buhner. "Spectroscopy of the electric-quadrupole transition $^2S_{1/2}$(F=0)-$^2D_{3/2}$(F=2) in trapped $^{171}Yb^+$." Phys Rev. A **61**(5), 053405, May 2000.

[Tie02] E. Tiesinga, S. Kotochigova, and P. S. Julienne. "Scattering length of the ground-state Mg+Mg collision." Phys. Rev. A **65**, 042722, 2002.

[Ude01a] Th. Udem, S. A. Diddams, K. R. Vogel, C. W. Oates, E. A. Curtis, W. D. Lee, W. M. Itano, R. E. Drullinger, J. C. Bergquist, and L. Hollberg. "Absolute Frequency Measurements of the Hg^+ and Ca Optical Clock Transitions with a Femtosecond Laser." Phys. Rev. Lett. **86**(22), 4996–9, May 2001.

[Ude01b] Th. Udem, S. A. Diddams, K. R. Vogel, C. W. Oates, E. A. Curtis, W. D. Lee, W. M. Itano, R. E. Drullinger, J. C. Bergquist, and L. Hollberg. "Absolute Frequency Measurements of the Hg^+ and Ca Optical Clock Transitions with a Femtosecond Laser." Phys. Rev. Lett. **86**, 4996, 2001.

[Ung89] P. J. Ungar, D. S. Weiss, E. Riis, and Steven Chu. "Optical molasses and multilevel atoms: theory." J. Opt. Soc. Am. B **6**(11), 2058, November 1989.

[Vas78] B. V. Vasilev and E. V. Kolycheva. Sov. Phys. JETP, 1978.

[Vet01] P. A. Vetter, S. J. Freedman, B. K. Fujikawa, and N. D. Scielzo. "The beta - nu correlation using a neutral atom trap." AIP Conference Proceedings **570**, 89, 2001.

[Vog99] Kurt Richard Vogel. *Laser Cooling on a Narrow Atomic Transition and Measurement of the Two-Body Cold Collision Loss Rate in a Strontium Magneto-Optical Trap.* PhD thesis, University of Colorado, 1999.

[vW94] W. A. van Wijngaarden and J. Li. "Measurement of isotope shifts and hyperfine splittings of ytterbium by means of acousto-optic modulation." J. Opt. Soc. Am. B **11**(11), 2163, November 1994.

[Wal90] T. G. Walker, D. W. Sesko, and C. E. Wieman. "Collective behavior of optically trapped neutral atoms." Phys. Rev. Lett. **64**(4), 408, January 1990.

[Wal92] C. D. Wallace, T. P. Dinneen, K. Y. N. Tan, T. T. Grove, and P. L. Gould. "Isotopic difference in trap loss collisions of laser cooled rubidium atoms." Phys. Rev. Lett. **69**, 897900, 1992.

[Wal94] C. D. Wallace, T. P. Dinneen, K. Y. N. Tan, A. Kumarakrishnan, P. L. Gould, and J. Javanainen. "Measurements of temperature and spring constant in a magneto-optical trap." J. Opt. Soc. Am. B **11**(5), 703, May 1994.

[Wan97] H. Wang, J. Li, X. T. Wang, C. J. Williams, P. L. Gould, and W. C. Stwalley. "Precise determination of the dipole matrix element and radiative lifetime of the ^{39}K 4p state by photoassociative spectroscopy." Phys. Rev. A **55**(3), R1569, March 1997.

[Wei89] David S. Weiss, Erling Riis, Yaakov Shevy, P. Jeffrey Ungar, and Steven Chu. "Optical molasses and multilevel atoms: experiment." J. Opt. Soc Am. B **6**(11), 2072, November 1989.

[Wei99] John Weiner, Vanderlei S. Bagnato, Sergio Zilio, and Paul. S. Julienne. "Experiments and theory in cold and ultracold collisions." Rev. Mod. Phys. **71**(1), 1–85, January 1999.

[Wer93] J. Werner, H. Wallis, G. Hillenbrand, and A. Steane. "Laser cooling by σ^+-σ^- circularly polarized beams of unequal intensities." Journal of Physics B **26**, 3063, 1993.

[Win75] D. Wineland and H. Dehmelt. "Proposed 10^{14} $\delta\nu/\nu$ Laser Fluorescence Spectroscopy on Tl^+ Mono-Ion Oscillator." Bull. Am. Phys. Soc. **20**, 637, 1975.

[Win79] D. J. Wineland and W. M. Itano. "Laser cooling of atoms." Phys. Rev. A **20**(4), 1521, October 1979.

[Xu02] Xinye Xu, Thomas H. Loftus, Matthew J. Smith, John L. Hall, Alan Gallagher, and Jun Ye. "Dynamics in a two-level atom magneto-optical trap." Phys. Rev. A **66**, 011401(R), 2002.

[Xued] Xinye Xu, Thomas H. Loftus, Josh W. Dunn, Chris H. Greene, John L. Hall, Allan Gallagher, and Jun Ye. "Single-stage sub-Doppler cooling of alkaline earth atoms." Phys. Rev. Lett., *to be published.*

[Yar75] Amnon Yariv. *Quantum electronics.* Wiley, New York, 1975.

[Zho95] W. L. Zhou, Y. Mori, T. Sasaki, S. Nakai, K. Nakano, S. Niikura, and B. Craig. "Intracavity frequency doubling of a continuous wave Ti:sapphire laser with over 70% conversion efficiency." Appl. Phys. Lett. **66**(19), 2463, May 1995.

[Zin00] G. Zinner, T. Binnewies, and F. Riehle. "Photoassociation of Cold Ca Atoms." Phys. Rev. Lett. **85**, 2292, 2000.

Appendix A

ELECTRONICS SCHEMATICS

This appendix contains the electronics schematic and layout of the current drivers for the Zeeman slower, the bias, and MOT coils, and the slow-lock for the green laser. The electronics for the fast-lock for the green laser using the Pound-Drever scheme and for the laser doubling cavity lock are shown and explained in theses by Burt [Bur95] and Sandberg [San93].

A.1 Driver for Zeeman Slower, Bias Coils, and MOT Coils

The Zeeman slower, bias coils, and MOT coils were driven by separate current supplies controlled by electronics as shown in Figure A.1. The current in each coil are controlled by either a stable voltage reference from an LM399 or an external voltage source. The current in each coil is monitored by a $0.1\,\Omega$ sense resistor, which provides a $100\,\mathrm{mV}/1\,\mathrm{Amp}$ current monitor signal. The current monitor signal is fed back with an op-amp (LF411) and the current is controlled by a power MOSFET (IRF150). The current in each coil can also be monitored by an LCD panel meter mounted on the box. The direction of the current in each coil can be reversed with a switch located on the front face of the box. The MOT coils can also be made to run in a Helmholtz configuration by running the current in the same direction in the two coils.

The MOT coils can run either independently or in series. In the independent mode, the center of the magnetic field gradient can be moved vertically, and series mode ensures that the same current is running in both coils. Series mode was used in most of the work done for this dissertation.

The inductance and resistance of the Zeeman slower, bias, and MOT coils measured at room temperature are listed in Table A.1. The knowledge of the inductance of MOT coils is important when the magnetic field gradient needs to be changed quickly. The MOT field

used in this experiment can be turned off in less than 400 μs.

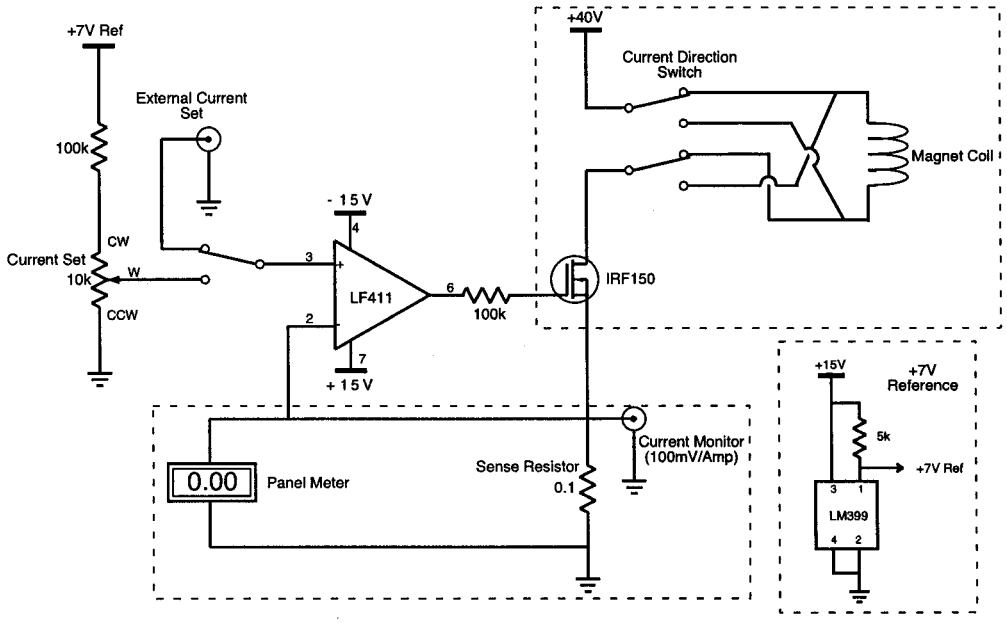

Figure A.1: Schematic of a coil driver electronics used for the Zeeman slower, Zeeman bias, and MOT coils. Each coil has a separate control as shown in this figure.

Table A.1: The measured inductance and resistance of the Zeeman slower, bias, and MOT coils.

	Resistance (R)	R at 1 kHz	Inductance (L)	L/R
Zeeman	7.4 Ω	130 Ω	35 mH	4.6 ms
Bias	2.8	18	4.4	1.6
MOT (top)	0.5	5.0	1.3	2.6
MOT (bottom)	0.5	4.9	1.3	2.5

A.2 Slow Lock for the Green Laser

The long-term lock is established by locking the narrowed laser to the $^1S_0$–$^3P_1$ Yb transition. The error signal is produced by modulating the magnetic sublevels of the $^3P_1$ state. The Zeeman shift to the ground state is negligible since there is no electronic spin. Helmholtz coils apply a Zeeman-shift to the atomic beam resonance and small modulation is applied to the current. The fluorescence signal is collected by a lens onto a PMT, and the signal is demodulated with a lock-in amplifier. The output of the lock-in amplifier is the error signal, and is fed into the external piezo-voltage control of the driver of the Fabry-Perot cavity used for the short-term lock.

Figure A.2 and A.3 shows the layout of the electronics board that includes a PMT pre-amp and gain control, and current driver for the Helmholtz coils used to modulate the atomic resonance. The board is laid out as follows. From the left: LM399 (U1) produces a stable +7 V voltage reference, with (U2) as a follower. XR8038 (U3) is a function generator which puts out sine and TTL square waves in the range of 0.001 Hz to 200 kHz. The operating frequency is 1 kHz. The square-wave is fed into the frequency reference of the lock-in amplifier, and the sine-wave drives the modulation of the magnet coils. The amplitude of the modulation is controlled with an op-amp (U4). It can also be turned off with a switch located on the front of the driver box. The modulation is AC-coupled and summed with an offset with an op-amp (U6). The offset can be set either by a POT on the box or an external voltage source, and has a follower (U5) to make sure that the voltage does not get drawn down. An offset can be added to the current in one of the coils at this point (U9). The modulated signal goes into the feedback op-amps (U7) and (U10) that control the current of the magnet coils.

The PMT pre-amp gain is controlled by (U11) and (P3), and the signal is fed into a lock-in amplifier by EG&G. The output of the lock-in amplifier can be amplified and integrated with (U12) and (U13) if necessary. A lock-in amplifier has its own integration stage on the output, and the 100 ms filter was used for much of the work here. The output of the lock-in is fed back into the Fabry-Perot cavity controller to keep the laser frequency locked to the atomic transition.

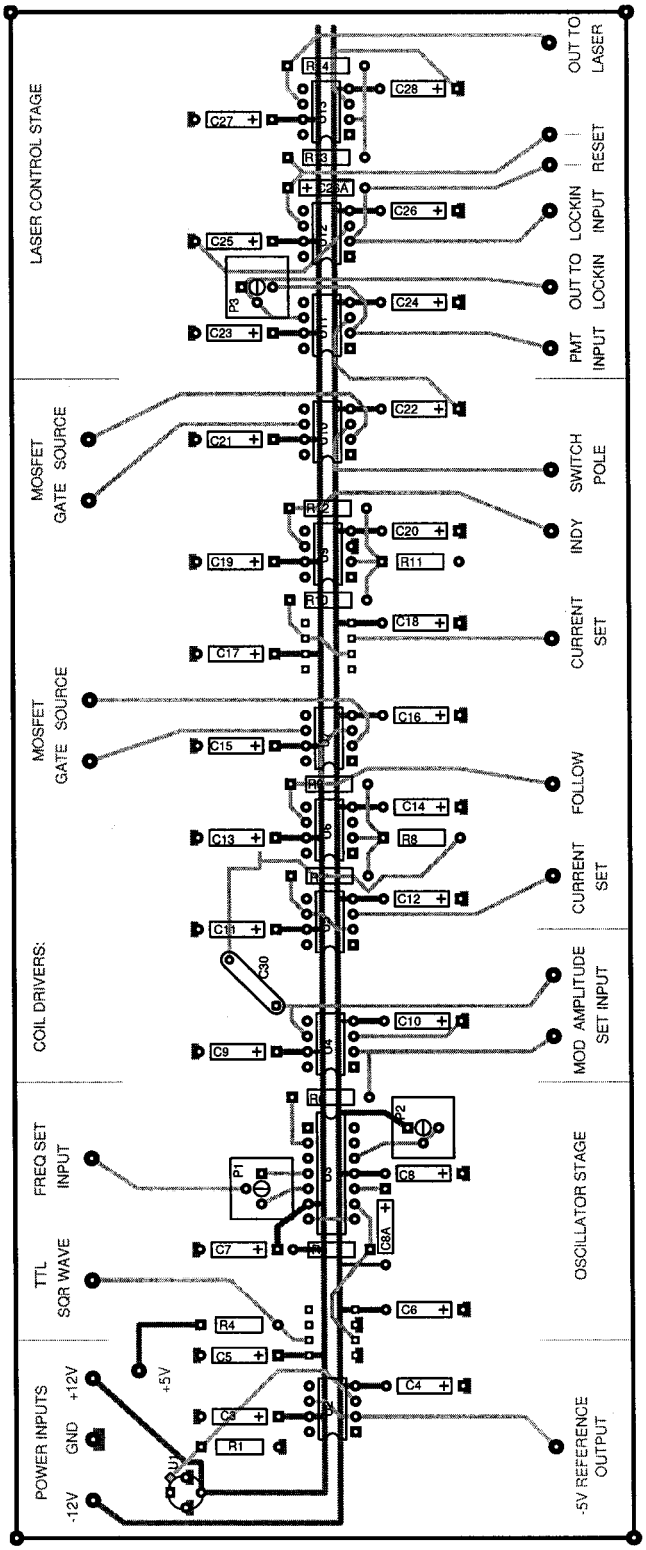

Figure A.2: The board layout for the current drivers to produce magnetic field for the green laser long-term stability lock.

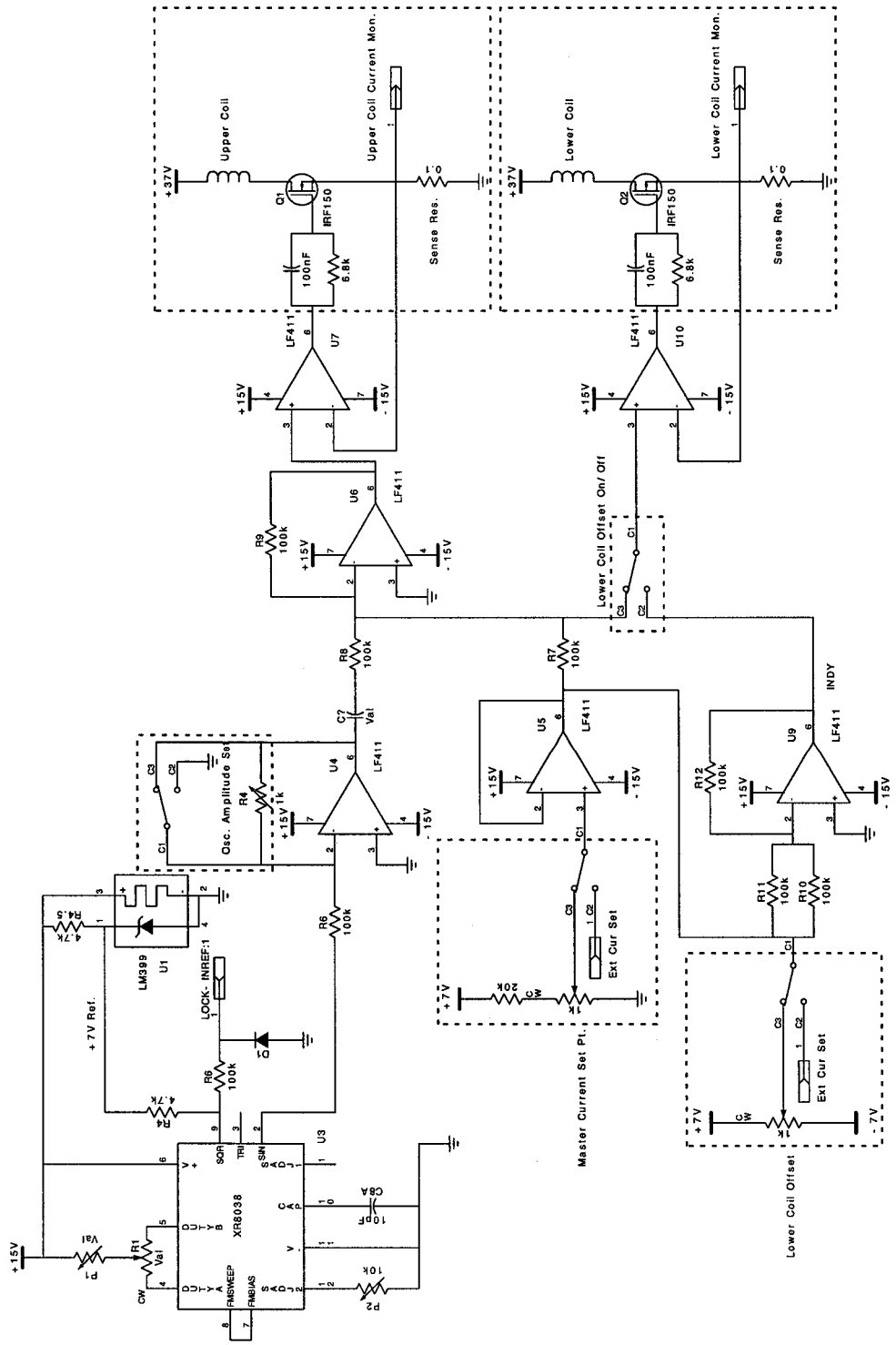

Figure A.3: The schematic of the green lock magnetic field driver. Dashed boxes indicate components that are off the board.

Appendix B

DIRECT LOADING OF THE GREEN MOT

Currently, the number of atoms in the traps are limited by the lifetime of the $^1S_0$–$^1P_1$ transition. To achieve a higher number of atoms and density, we need to implement direct loading of the green MOT. In this scheme, we would use the $^1S_0$–$^1P_1$ transition for the Zeeman slower, and trap the atoms with the $^1S_0$–$^3P_1$ transition. A Zeeman slower using the $^1S_0$–$^3P_1$ transition would be impractical because the transition is so weak and the slower would have to be extremely long. There are several advantages to direct loading: since the green MOT lifetime is so much longer we will be able to collect more atoms. We can also replace the Ar^+, Ti:sapphire, and doubling cavity combination with a simple diode laser because the laser power required to form an efficient blue MOT is no longer necessary. This will make the green MOT loading procedure simpler and hopefully more reliable.

The trap depth and capture range of a green MOT is extremely narrow due to the narrow linewidth of the transition. To improve the loading efficiency, the laser needs to be broadened in a controlled manner. This is accomplished by putting sidebands on the primary carrier frequency in the green MOT AOM driver. Figure B.1 is a schematic of the electronics used. The rf output of the VCO (voltage-controlled oscillator) at 80 MHz is split in two by a power splitter from MiniCircuits, and each half is mixed with a 300 kHz and 900 kHz by a double-balanced mixer. The two halves are combined again, and fed through an amplifier, and into the AOM. The amplitude of the 300 kHz and 900 kHz oscillations are adjusted so that the four sidebands are of equal magnitude. As a result, we obtain four frequencies separated by 600 kHz centered around 80 MHz ($\pm$300 kHz and $\pm$900 kHz), and the effective width of the laser after it goes through the AOM is 2.4 MHz.

We have implemented laser broadening for the green MOT loading. Although it was necessary to have a larger laser detuning so that the highest sideband frequency is still to the red of the resonance, we found the MOT to be more robust. The transfer efficiency from

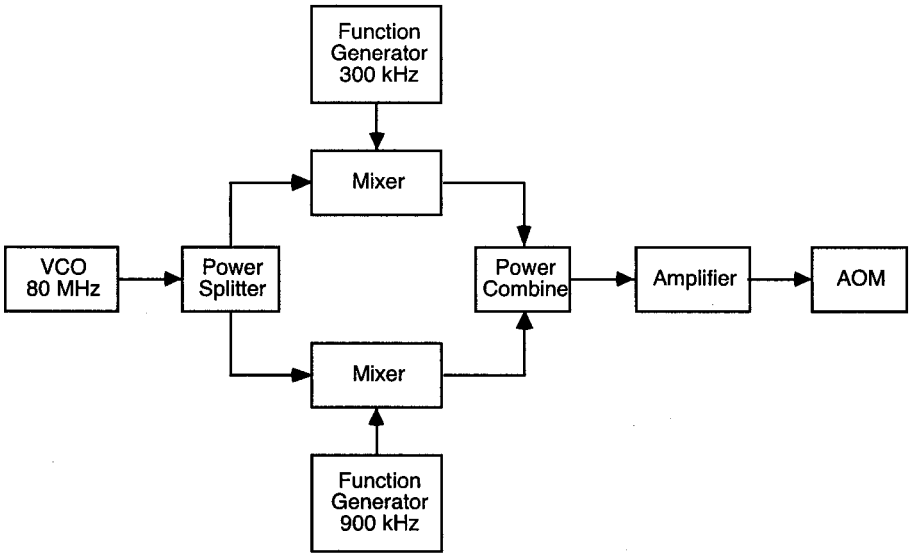

Figure B.1: Electronics for adding sidebands to the green laser.

the blue MOT into the green MOT is higher, and the green MOT is less susceptible to laser dropouts and instabilities. The temperature of the MOT is higher in this configuration due to the broad laser width, and the ability to turn off the sidebands after the MOT has been loaded is being added.

To achieve reliable trap loading, it is necessary to lock the blue laser and carefully tune the frequency for the Zeeman slower. The capture range of the green trap is narrower than that of the blue trap even with the laser broadened, and the velocity of the atoms coming out of the Zeeman slower will have to be monitored carefully. We have constructed a second atomic beam dedicated for locking the blue laser with electronics similar to the one used in the slow lock of the green laser.

Appendix C

SIMULTANEOUS DIPOLE TRAPPING WITH A MOT

To proceed with precision measurements using trapped atoms, it may be necessary to load the Yb atoms into an optical dipole trap, also called FORT (far-off-resonance trap). Because these traps are conservative and do not dissipate energy, it is necessary to first cool the atoms in a MOT. Efficient transfer of atoms from a MOT to a FORT is desirable for achieving high number densities in the FORT. The light shift caused by the presence of the FORT laser can alter the performance of the cooling in a MOT. In a normal dipole-allowed transition, the ground state and the upper state are shifted in the opposite direction, making simultaneous dipole trapping and Doppler cooling incompatible. Optimization of FORT loading has been the subject of study for many groups (see Ref. [Kup00] for example), and Doppler cooling for dipole traps have been implemented by alternating between the cooling and dipole trap phases [Mil93].

Ytterbium and alkaline-earth atoms have the advantage that they can be cooled on the $^1S_0$–$^3P_1$ intercombination line. The $^1S_0$ and $^3P_1$ states are more strongly coupled to other states which have the same S-number than to each other, therefore it is possible to produce the same amount of light shift in the two states by choosing the right wavelength for the dipole trap laser. High phase-space density exceeding 0.1 and a hight transfer efficiency of 80% have been achieved in Sr using this technique [Ido00, Kat99a]. The intercombination line of Sr is weaker than in Yb. By combining the continuous loading of the green MOT and a simultaneous dipole trap, it may be possible to have a very efficient Yb dipole trap with a very large phase-space density.

A rough estimate of the wavelength necessary to achieve simultaneous dipole trapping and Doppler cooling has been made. Ytterbium has the complication of having many states associated with the excited f-electrons, and the calculation shown here will have to be tested experimentally. The transition wavelengths are listed in Ref. [Mar78] and their lifetimes are

Table C.1: The wavelengths and lifetimes of the dipole-allowed transitions to the $6s6p^3P_1$ state of Yb.

	$6s5d^3D_1$	$6s5d^3D_2$	$6s7s^3S_1$	$6s6d^3D_1$	$6s6d^3D_2$	$6p6p^3P_0$	$6p6p^3P_1$	$6p6p^3P_2$
λ (nm)	1540	1480	680	458	458	409	387	374
τ (ns)	1086	613	39	50	29	—	15	—

listed in Refs. [Bla94, Bow96, Bla78].

The static polarizability of ytterbium in the ground state is $\alpha_s = 21.0 \times 10^{-24}\,\mathrm{cm}^3$. The states that are dipole-coupled to the ground state are the upper state of the blue and green transitions: $6s6p^1P_1$ and $6s6p^3P_1$. Their wavelengths are 399 nm and 556 nm, and lifetimes are 5.5 ns and 850 ns respectively. The states that couple to the $6s6p\ ^3P_1$ via electric dipole transition and their wavelengths and lifetimes are listed in Table C.1. The lifetimes of the $6p6p^3P_0$ and $6p6p^3P_2$ states could not be found in the literature, and were omitted in the calculation. The contributions to the light shift of the $6s6p^3P_1$ state from these states are expected to be small, especially if the laser is tuned far from resonance.

Figure C.1 shows the light-shift induced by a dipole trap laser of 100 mW focused to a 15 μm waist as a function of its wavelength. The red line shows the shift induced in the ground state, $6s^2\ ^1S_0$. The short dashed line is the light-shift induced on the $M = 0$ magnetic sub-level of the $6s6p^3P_1$ state by a π-polarized light ($\Delta M = 0$), the skip-dashed line is the shift on the $M = \pm 1$ sub-levels by a $\sigma^{\pm}$ light ($\Delta M = \pm 1$), and the long-dashed line is for the $M = \pm 1$ sub-levels shifted by a π-polarized light, or $M = 0$ shifted by a $\sigma^{\pm}$ light. The shifts in the ground and $6s6p^3P_1$ states cross at 819.65 nm for the skip-dashed line, and at 847.53 nm for the long-dashed line. The short-dashed line has no solution. Simultaneous dipole trap and MOT may be accomplished by choosing either of these wavelengths with the appropriate polarization for the FORT trap beam.

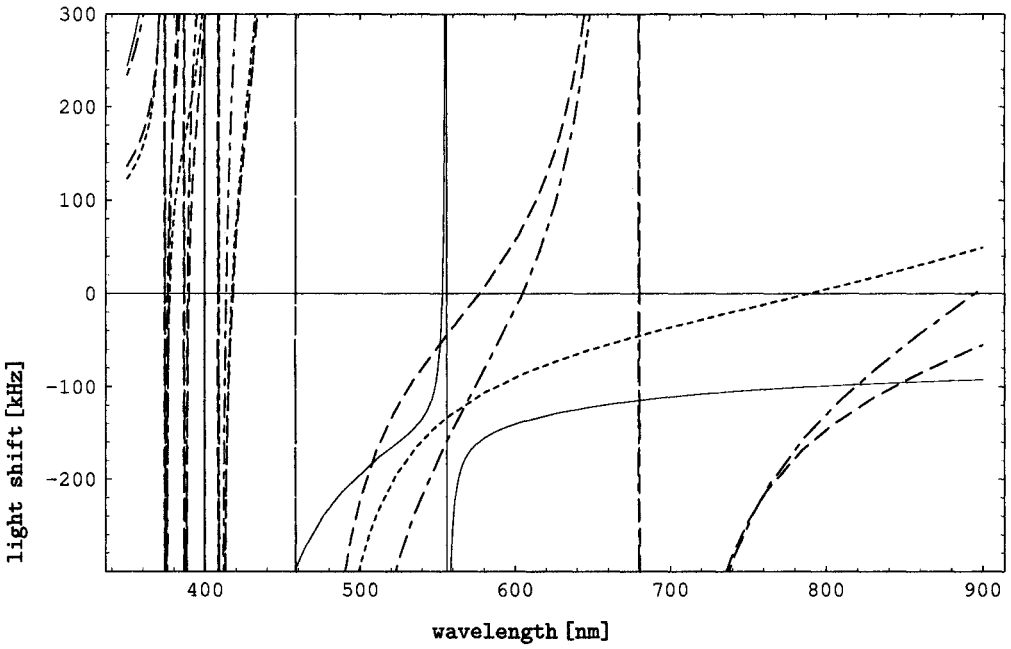

Figure C.1: Light shift induced in the $6s6s\,^1S_0$ (red) and $6s6p\,^3P_1$ states (dashed lines) by a single 100 mW FORT beam focused to a 15 μm spot size. The short dashed line is the light-shift induced on the $M = 0$ magnetic sub-level of the $6s6p\,^3P_1$ state by a π-polarized light ($\Delta M = 0$), the skip-dashed line is the shift on the $M = \pm 1$ sub-levels by a $\sigma^{\pm}$ light ($\Delta M = \pm 1$), and the long-dashed line is for the $M = \pm 1$ sub-levels shifted by a π-polarized light, or $M = 0$ shifted by a $\sigma^{\pm}$ light.

VITA

Reina Maruyama was born in Japan in August, 1973. Her family moved to New Canaan, CT in 1985, where she later attended high school. She received a B.S. from the Department of Applied Physics at the School of Engineering and Applied Sciences, Columbia University in May of 1995. She began her graduate work at the University of Washington in 1995, subsequently receiving a M.S. in 1996, and receiving a Ph.D. in 2003 with Prof. Norval Fortson as her advisor. She will begin her postdoctoral research at the University of California at Berkeley, where she is the recipient of the 2003 Chancellor's Postdoctoral Fellowship.